VIBRATION SUPPRESSION THROUGH STIFFNESS VARIATION AND MODAL DISPARITY

By

Jimmy Issa

A DISSERTATION

Submitted to
Michigan State University
in partial fulfillment of the requirements
for the degree of

DOCTOR OF PHILOSOPHY

Department of Mechanical Engineering

2008

INFORMATION TO USERS

The quality of this reproduction is dependent upon the quality of the copy submitted. Broken or indistinct print, colored or poor quality illustrations and photographs, print bleed-through, substandard margins, and improper alignment can adversely affect reproduction.

In the unlikely event that the author did not send a complete manuscript and there are missing pages, these will be noted. Also, if unauthorized copyright material had to be removed, a note will indicate the deletion.

ProQuest LLC
789 E. Eisenhower Parkway
PO Box 1346
Ann Arbor, MI 48106-1346

ABSTRACT

VIBRATION SUPPRESSION THROUGH STIFFNESS VARIATION AND MODAL DISPARITY

By

Jimmy Issa

Vibration suppression is the main objective of this study. A semi-active and an active vibration control strategy based on stiffness variation are proposed for removing energy from vibrating structures. For the semi-active vibration control strategy, the notion of modal disparity is introduced and exploited as a new method of vibration suppression. For a given structure, modal disparity is a measure of the difference in the mode shapes of the structure in two stiffness states. Modal disparity is validated experimentally in a beam where stiffness variation is induced by application and removal of constraints. In dynamical systems modeled with finite degrees-of-freedom, the application of constraints transfers energy to the unmodeled high-frequency modes, where it is dissipated naturally and quickly. The removal of constraints does not dissipate energy but resets the system for the constraints to be applied again for further reduction of energy. Thus sequential application and removal of constraints eventually dissipates the energy of the system completely. It is shown that energy removal is always possible, even with a random switching schedule, except in one case where the energy is trapped in modes that span invariant subspaces with certain orthogonality properties. The optimal locations and timing of constraint application is investigated with the goal of maximizing energy dissipation through maximal energy transfer to the unmodeled high-frequency modes. For the active control strategy, cable actuators are proposed for removing energy from three-dimensional framed structures. The tension in the cables has two effects on the structure; it increases the stiffness of the structure and applies an external load on the structure. Both effects are used in the

design of the active control strategy in which the cable tension is essentially switched between different levels to do negative work. Experimental results are presented to validate the efficacy of the control strategy.

To my dear parents Samir and Josephine.

ACKNOWLEDGMENTS

My utmost gratitude goes to my thesis advisor Dr. Ranjan Mukherjee for his continuous guidance and endless support during my years at Michigan State University.

A special thanks goes to Dr. Steven W. Shaw for providing valuable instructions and suggestions and for his continuous help throughout my years of graduate studies.

I would like to express my deep and sincere gratitude to Dr. Alejandro R. Diaz for his help and support.

My thanks to Dr. Alan Haddow and Dr. Hassan Khalil for serving as members of my Ph.D committee. They provided useful suggestions to improve this work.

My thanks to Umar Farooq, Elliot Motato, Jeffrey Rhoads, Nicholas Miller and Nandagopal Methil-Sudhakaran for providing me valuable help and for their friendship.

Finally, I would like to thank the graduate secretary Aida Montalvo for her help.

TABLE OF CONTENTS

CHAPTER 1

Introduction

1.1 Background and Objectives

Vibration control is a subject of significant importance with applications ranging from small scale structures like micro beam resonators to large scale structures such as large space structures, buildings and bridges. All of these structures are prone to disturbances and excitations, for example, thermal gradients on space structures and wind excitation on bridges. To overcome the problem that arise due to disturbances and excitations and provide stability, control schemes are designed for energy removal. Typically, the control schemes fall into two categories; the first is active control in which the control action is based on realtime sensing of states of the structure. The second category, passive control, is implemented by embedding passive elements in the structure with the goal of increasing its energy dissipation properties. Some control schemes are based on a combination of the two strategies and can be described as semi-active control.

The goal of this study has been the exploration of new methods of vibration suppression. Our main target has been the stiffness of the structure and we have developed energy dissipation schemes based on stiffness variation. Two methods have been proposed. In one method, actuators are employed to locally enforce constraints

at predefined locations on a structure. This leads to a change in stiffness of the structure and transfer of energy from low-frequency to high-frequency modes. In the high-frequency modes, energy is dissipated quickly by conversion to heat without the need for active control. Since we actively transfer energy to the high-frequency modes where they are passively dissipated due to high levels of damping, we refer to this method as semi-active control. In the second method, an active control scheme is investigated where a cable actuator is used to transmit control forces to the structure. This results in a change in stiffness of the structure and simultaneous application of external forces. The tension is actively controlled and applied only when it removes energy from the structure.

1.2 A Semi-Active Vibration Control Strategy

The controlled redistribution of energy in vibrating structures is at the heart of many engineering problems with important practical applications. Modal control strategies, vibration absorbers, and some forms of energy harvesting, all rely in one form or another on the redistribution of energy in vibrating structures from mode to mode and, in space, from one region of the structure to another. Recently, a new methodology for design of structures was proposed to achieve a targeted and purposeful redistribution of vibration energy [1], [2]. This methodology relies on *modal disparity*, a quantifiable property of the structure being designed, and relies on a carefully crafted variation in the stiffness of the structure.

Stiffness variation, by itself, is not a new concept. For example, Clark [3] and Corr and Clark [4] proposed stiffness variation of piezoelectric actuators to accomplish energy dissipation in vibration control. Kurdila, et. al [5] proved that this state-switching strategy reduces the energy of the system and is stable, and Ramaratnam and Jalili [6] implemented this idea of "switched stiffness" in vibration control

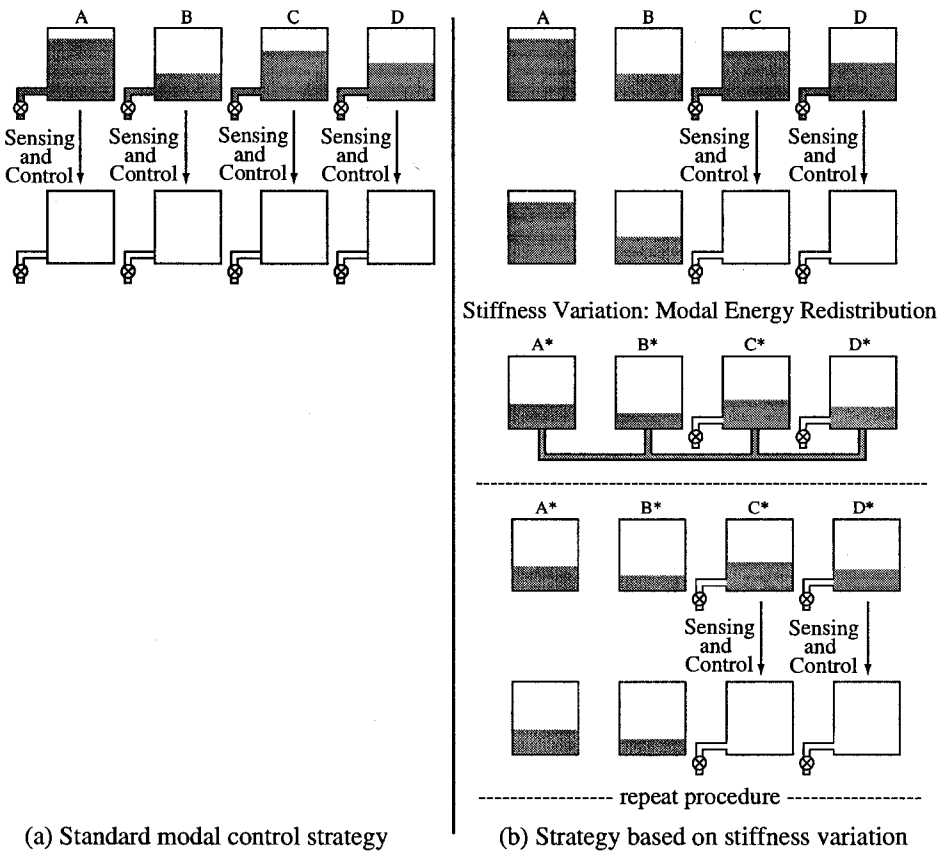

Figure 1.1. A simple analogy to illustrate a control methodology based on the concept of modal disparity.

experiments. In contrast to these results, where the purpose of stiffness variation is to dissipate energy, Diaz and Mukherjee [1], [2] proposed stiffness variation for modal energy redistribution which then can be used for energy absorption, harvesting, or dissipation. Modal energy redistribution should also be differentiated from earlier work on localization [7], [8], [9], and energy pumping [10], [11], where energy redistribution occurs spatially.

Stiffness variation and its effect on modal energy redistribution can be explained by means of a simple analogy where the amount of vibration energy present in a flexible structure is represented by a certain volume of fluid that needs to be drained away. A modal view corresponds to fluid (energy) that is distributed among a set of

discrete containers, one for each mode. Figure 1.1 depicts this situation using four modes, labeled A, B, C and D. In traditional modal control, the amount of fluid in each container has to be sensed separately and a controller that is capable of draining fluid from *all* the containers is used (Fig.1.1a). Now consider a situation where the fluid in only two containers, say containers C and D (Fig.1.1b), are sensed and then drained by a simple controller. Once all the fluid is removed from these containers, the overall fluid volume decreases, but fluid remains trapped in the other containers, A and B. Energy redistribution of the remaining fluid among all the containers, including moving some fluid into containers C and D, can be achieved by stiffness variation. One step of stiffness variation, followed by draining of the fluid from containers C and D, would leave fluid in the other containers, but repeating this process back and forth between two stiffness states will drain the fluid from all the containers.

The success of a stiffness variation approach to energy redistribution is measured by the total amount of energy that is transferred *into* target modes (container C and D) at each step, and the details of how much energy is transferred *out* of the other modes, the source modes (containers A and B), at each step. The rate at which energy is redistributed depends on the source modes. For instance, if a source mode in one stiffness state is nearly identical to a source mode in the other stiffness state (e.g., B and B* in Fig.1.1b), then modal energy will drain very slowly from these modes, i.e., fluid will be essentially trapped in the corresponding containers. To quantify the amenability of a structure to energy redistribution strategies, a measure of energy redistribution is needed. *Modal disparity* is such measure. It is a property of the structure, as well as of the device introduced to effect the change in stiffness. In this work, we generate modal disparity in structures with the objective of transferring energy from the low-frequency modes to the high-frequency modes, where it can be dissipated naturally and quickly.

As part of our semi-active control strategy, we consider stiffness variation in structures through the application and removal of constraints. The effect of application and removal of constraints on the system dynamics is studied and modal disparity between the resulting stiffness states is quantified in chapter 2. In chapter 3 modal disparity is experimentally verified through redistribution of modal energy between the modes of a clamped-clamped beam in its two stiffness states. In particular, the beam has a pin joint at mid-span that can be locked using an electromagnetic brake or allowed to rotate freely by releasing the brake; the two stiffness states of the beam result from locking and releasing the pin joint. In chapter 4 we propose a control strategy based on the scheme in Fig.1.1. The only difference is that the energy in containers C^* and D^* are not drained by active control. Instead, these containers are chosen to correspond to the high-frequency modes of the system such that the energy is drained due to internal damping. In chapter 4, we model the system with finite dof[1] and treat the high-frequency modes as unmodeled dynamics of the system. The control strategy developed relies on application and release of constraints that effectively transfer energy to the high-frequency unmodeled modes, where they are dissipated by conversion to heat. The constraints are applied at predefined locations on the structure and it is shown that energy reduction is always possible except in some special cases. With the view to obtain faster rates of energy dissipation, the location and timing of the constraints are optimized in chapter 5. Two example problems are considered with different optimization criteria.

1.3 Active Vibration Suppression Strategy

Active vibration suppression has a long history of research. A variety of actuators have been employed in active control and these include, piezoelectric materials,

[1]degrees-of-freedom

thrusters, momentum wheels, and cables, and their performance depends on the type of structure (beam, truss, frame) and their placement on the structure. The idea of active tendon control began as a way to reduce damage in cable stayed-bridges and buildings caused by earthquakes and wind. It has been primarily developed by civil engineers, as described, for example, in Yang et al. [12, 13]. Cables are attractive as actuators for large-scale structures since their effects can be transmitted far from the energy source of the actuator and, in addition, their effects can be non-local, for example, by changing the overall stiffness of a structure. Many approaches to the control system design for cable actuators in large-scale structures have been proposed due to the variety of structures considered, in both civil and aerospace applications.

Among the work on cable control for civil structures, Chung et al. [14] carried out an experiment and used an optimal control scheme to reduce the response of a single dof building type structure under base motion. Other authors [15] used active tendon actuators to reduce the horizontal vibration of building structures subjected to seismic and wind excitation. Warnitchai et al. [16] carried out an experiment to study the feasibility of active tendon control on cable-stayed bridges using velocity feedback control. Other authors used active tendon actuator to reduce vibration in cable stayed beams and cable stayed bridges, for example, Magana et al. [17, 18] and Fujino et al. [19]. Achkire and Preumont [20] and Bossens and Preumont [21] used positive integral force feedback, an energy absorbing control strategy, to suppress the vibration of large cable-stayed bridges; the cable forces were supplied by a specially-built large scale hydraulic actuator.

Cable structures are very attractive for aerospace applications, where weight is an important issue. In these applications the cables not only offer lightweight structural support, they are also used as active tendons to provide stability. In recent years

the idea of active tendon control in aerospace applications was explored and many approaches have been proposed. Murotsu et al. [22] used a newly conceived torque actuation devise for controlling the vibrations of a beam-like space structure using position and velocity feedback. Okubo et al. [23] proposed a tendon control system for the shape control of flexible space structures. Preumont et al. [24, 25] used cable tension to stiffen and control trusses by inducing active damping. Nudehi et al. [26] used a cable-supplied end force to suppress the transverse vibrations of a cantilever beam. The control is based on active stiffness variation in which Lyapunov stability theory and passivity analysis were used to determine when to apply and release tension in the cable in order to pump energy out of the system.

In chapter 6 we extend the approach of Nudehi et al. [26] to three dimensional frame structures. Unlike the beam problem where cable tension resulted in stiffness variation of the beam only, cable tension in structures typically result in simultaneous stiffness variation and application of external forces. Both of these effects are used in the design of an active control scheme to remove energy and suppress vibration of the structure. For the development of the control scheme, a finite element model of cable-framed structures is proposed and the effect of the cable placement on the structure is investigated. Both numerical simulations and experimental results are presented.

CHAPTER 2

Modal Disparity

2.1 Stiffness Variation And Modal Disparity

The main objective of this chapter is to formally introduce the notion of modal disparity and to propose a measure to quantify it. Modal disparity arise in structures capable of having multiple stiffness states. Typically, some mechanism is required to switch stiffness states and hence modal disparity is a property of the structure as well as the mechanism used to change the stiffness.

To define modal disparity, we consider a linear system vibrating freely about its equilibrium position. The potential energy of the system is assumed to be zero in this equilibrium configuration, which will be referred to as the zero equilibrium henceforth. The free vibration of the system about the zero equilibrium is described by a set of natural frequencies and mode shapes, and an energy distribution among the modes. When the stiffness of the system is changed (by a suitable mechanism) the equilibrium configuration changes and the system is described by a new set of natural frequencies and mode shapes. In the general case, the new equilibrium configuration of the system will have some stored potential energy and therefore will not be a zero equilibrium. Due to the change of stiffness, the total energy of the system will be redistributed. Assuming that no energy is lost due to change of stiffness, a part of

the energy will be stored as potential energy in the new equilibrium configuration; the rest will be distributed among the new modes of the system. When the stiffness of the system reverts back to its original value, the system recovers its original shape and vibrates about the zero equilibrium position. All the energy of the system is transferred back to the modes of its original configuration. If damping is ignored and if no loss of energy occurs due to modal truncation, the total energy of the system is conserved but the energy distribution among the modes is different from that at the initial time. The activation and deactivation of the stiffness variation mechanism thus allows redistribution of modal energy. The amount of energy pumped into or out of a specific mode is dependent on the timing of the transition between stiffness states and difference in mode shapes of the structure in the two stiffness states.

A water-bucket analogy of modal energy redistribution due to change in stiffness, as discussed in the paragraph above, is depicted in Fig.2.1. The level of energy in the modes is represented by the volume of water in the buckets. When the mechanism is activated, the equilibrium configuration changes and some volume of water is stored as potential energy in the new equilibrium configuration. The remaining volume is distributed between the buckets that represent the modes of the system in its new stiffness state. When the stiffness of the system reverts back to its original value, the total amount of water remains conserved but its distribution between the buckets changes.

The efficacy of energy redistribution can be quantified by the difference in the volume of water in each bucket at the initial time and after one cycle of stiffness variation. While this will depend on the time when the stiffness is changed and reverted back to its original value, it will also depend on the difference between the mode shapes of the structure in the two stiffness states. A measure of the change in

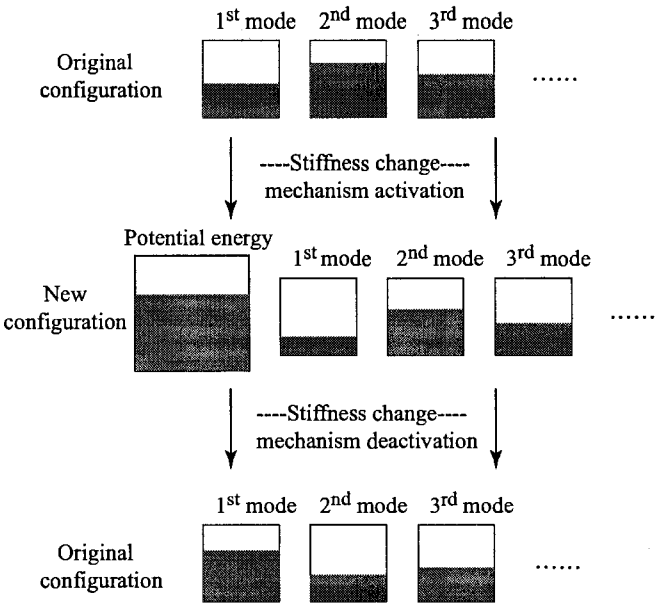

Figure 2.1. Modal energy redistribution after one cycle of constraint application and removal

the mode shapes of the system due to change in stiffness is modal disparity. Modal disparity, defined next, contributes to modal energy redistribution.

Modal disparity *is the degree to which the mode shapes of the system in its original stiffness state are different from those in its new stiffness state. The projection of one set of mode shapes onto the other through the mass of the system is a good way to quantify this difference. Typically, if there is no change in the stiffness, there will be no change in the modes and if the modes are normalized with respect to the mass matrix, this projection will lead to the identity matrix. In the case of stiffness variation, this projection will lead to a matrix called the modal disparity matrix. The norm of the* (i, j) *element of this matrix is a measure of how close the* i^{th} *mode of system in one stiffness state is to the* j^{th} *mode in the other stiffness state. This matrix is essential for understanding the mechanics of transition between different stiffness states of a given system.*

The stiffness of a system can be changed in a variety of ways. Diaz and Mukherjee, for example proposed the use of cables [2], and active joints [27] for varying the stiffness of three dimensional structures. In this present study we consider enforcing constraints on the system as a way of changing its stiffness. In the next section we derive expressions to relate the system displacements and velocities before and after the change of stiffness. In section 2.3 a modal coordinate description of the transitions is presented and modal disparity is quantified. A numerical example is presented in section 2.4 to illustrate energy redistribution due to modal disparity. In this example, the axial vibration of a rod is considered. The rod is fixed at one end and free at the other and a magnetic brake is used to restrain the motion of the free end at any desired time.

2.2 Spatial Coordinate Description

We consider the general case of continuous systems. An N dof[1] reduced order model of such systems can be derived using finite element methods. Ignoring damping, the equation of motion describing the behavior of the system about its zero equilibrium position can be written as follows:

$$M\ddot{X} + KX = 0 \tag{2.1}$$

where M and K are the $N \times N$ mass and stiffness matrices of the reduced order system and X is the N dimensional vector of generalized displacements corresponding to the dof. This unconstrained state of the system is referred to as state α. Upon application of a constraint, the configuration of the system changes. Using the same finite element mesh, a reduced order model with N dof is again considered to facilitate mathematical operations. In this state the system vibrates about its new equilibrium position. Ignoring damping and using the new equilibrium as a reference, the equation

[1]degree-of-freedom

of motion of the system can be written as

$$M\ddot{Y} + \widetilde{K}Y = 0 \tag{2.2}$$

where $\widetilde{K}$ is the new $N \times N$ stiffness matrix and Y is the N dimensional vector of displacements corresponding to the new dof. Physically, X and Y are the displacements of the same nodes of the finite element model but have different origins because of the system vibrating about different equilibrium configurations. The constrained state of the system is referred to as state β.

After describing the behavior of the system in each state, we derive expressions to relate the system displacements and velocities during its transition from one state to another. We first assume that the system is vibrating in state α, and at some time $t_{\alpha\beta}$, the constraint is enforced to transfer the system to state β. This transition actually occurs over a brief interval of time $t \in [t_{\alpha\beta}^-, t_{\alpha\beta}^+]$ and results in the application of impulsive forces. The system displacements and velocities after the application of the constraint, $X(t_{\alpha\beta}^+)$ and $\dot{X}(t_{\alpha\beta}^+)$, can be related to the system displacements and velocities before the application of the constraint, $X(t_{\alpha\beta}^-)$ and $\dot{X}(t_{\alpha\beta}^-)$ as follows:

$$\begin{aligned} X(t_{\alpha\beta}^+) &= X(t_{\alpha\beta}^-) \\ M\dot{X}(t_{\alpha\beta}^+) &= M\dot{X}(t_{\alpha\beta}^-) + I_{\alpha\to\beta} \end{aligned} \tag{2.3}$$

where $I_{\alpha\to\beta}$ is the impulse vector. The equation above can be solved without a problem since the number of unknowns in $I_{\alpha\to\beta}$ is equal to the number of dependent variables in $\dot{X}(t_{\alpha\beta}^+)$. The initial conditions $Y(t_{\alpha\beta}^+)$ and $\dot{Y}(t_{\alpha\beta}^+)$ of state β are expressed in terms of the final conditions in state α as

$$\begin{aligned} Y(t_{\alpha\beta}^+) &= X(t_{\alpha\beta}^+) - X_0(t_{\alpha\beta}^+) \\ \dot{Y}(t_{\alpha\beta}^+) &= \dot{X}(t_{\alpha\beta}^+) \end{aligned} \tag{2.4}$$

where $X_0(t^+_{\alpha\beta})$ is the new equilibrium position. The equilibrium position $X_0(t^+_{\alpha\beta})$ is determined from static analysis of the structure, as will be illustrated with the help of an example later in section 2.4. It is important to note that $X_0(t^+_{\alpha\beta})$ is a function of the switching time $t_{\alpha\beta}$. Thus, the amount of potential energy stored in the system, $E_0 = \frac{1}{2}X_0^T(t^+_{\alpha\beta})KX_0(t^+_{\alpha\beta})$, is time dependent. When the constraint is removed, the system reverts back to state α. This transition occurs over a brief interval of time $t \in [t^-_{\beta\alpha}, t^+_{\beta\alpha}]$, during which there will be no change in the system displacements or momentum, *i.e.*

$$\begin{aligned} Y(t^+_{\beta\alpha}) &= Y(t^-_{\beta\alpha}) \\ \dot{Y}(t^+_{\beta\alpha}) &= \dot{Y}(t^-_{\beta\alpha}) \end{aligned} \tag{2.5}$$

The initial conditions of the system in state α are calculated from the displacements and velocities in state β using the relations

$$\begin{aligned} X(t^+_{\beta\alpha}) &= Y(t^+_{\beta\alpha}) + X_0(t^+_{\alpha\beta}) \\ \dot{X}(t^+_{\beta\alpha}) &= \dot{Y}(t^+_{\beta\alpha}) \end{aligned} \tag{2.6}$$

In the next section we investigate the transition between states in modal coordinates.

2.3 Modal Coordinates Description

In order to describe the system in modal space, we define ϕ_i and $\eta_i(t)$, $i = 1, 2, \ldots, N$, to be the normalized mode shapes and modal amplitudes of the unconstrained system. Similarly, we assume ψ_i and $\nu_i(t)$, $i = 1, 2, \ldots, N$, to be the normalized mode shapes and modal amplitudes of the constrained system. The system displacements $X(t)$ in state α and $Y(t)$ in state β can now be written as follows

$$\begin{aligned} X(t) &= \textstyle\sum_{i=1}^{N} \phi_i \eta_i(t) \qquad \text{in state } \alpha \\ Y(t) &= \textstyle\sum_{i=1}^{N} \psi_i \nu_i(t) \qquad \text{in state } \beta \end{aligned} \tag{2.7}$$

The change in the system displacements and velocities due to the application of a constraint, described by Eqs.(2.3) and (2.4), can be written as

$$\begin{aligned} Y(t^+_{\alpha\beta}) &= X(t^-_{\alpha\beta}) - X_0(t^+_{\alpha\beta}) \\ M\dot{Y}(t^+_{\alpha\beta}) &= M\dot{X}(t^-_{\alpha\beta}) + I_{\alpha\to\beta} \end{aligned} \tag{2.8}$$

Substitution of Eq.(2.7) into Eq.(2.8) yields

$$\begin{aligned} \textstyle\sum_{i=1}^{N} \psi_i \nu_i(t^+_{\alpha\beta}) &= \textstyle\sum_{i=1}^{N} \phi_i \eta_i(t^-_{\alpha\beta}) - X_0(t^+_{\alpha\beta}) \\ M \textstyle\sum_{i=1}^{N} \psi_i \dot{\nu}_i(t^+_{\alpha\beta}) &= M \textstyle\sum_{i=1}^{N} \phi_i \dot{\eta}_i(t^-_{\alpha\beta}) + I_{\alpha\to\beta} \end{aligned} \tag{2.9}$$

The modal displacements and velocities after application of the constraint can be computed from Eq.(2.9) as follows

$$\begin{aligned} \nu_j(t^+_{\alpha\beta}) &= \textstyle\sum_{i=1}^{N} \psi_j^T M \phi_i \; \eta_i(t^-_{\alpha\beta}) - \psi_j^T M X_0(t^+_{\alpha\beta}) \\ \dot{\nu}_j(t^+_{\alpha\beta}) &= \textstyle\sum_{i=1}^{N} \psi_j^T M \phi_i \; \dot{\eta}_i(t^-_{\alpha\beta}) \end{aligned} \tag{2.10}$$

In the derivation of Eq.(2.10) the identity $\psi_j^T I_{\alpha\to\beta} = 0$ was used. This follows from the fact that constraint forces do zero work, *i.e* $\dot{Y}(t^+_{\alpha\beta})^T I_{\alpha\to\beta} = 0$.

The modal displacements and velocities after the constraint has been removed are calculated using Eqs.(2.5), (2.6) and (2.7), as shown below

$$\begin{aligned} \eta_j(t^+_{\beta\alpha}) &= \textstyle\sum_{i=1}^{N} \phi_j^T M \psi_i \; \nu_i(t^-_{\beta\alpha}) + \phi_j^T M X_0(t^+_{\alpha\beta}) \\ \dot{\eta}_i(t^+_{\beta\alpha}) &= \textstyle\sum_{i=1}^{N} \phi_j^T M \psi_i \; \dot{\nu}_i(t^-_{\beta\alpha}) \end{aligned} \tag{2.11}$$

If we define

$$\eta(t) = \begin{bmatrix} \eta_1(t) \\ \eta_2(t) \\ \vdots \\ \eta_N(t) \end{bmatrix}, \qquad \nu(t) = \begin{bmatrix} \nu_1(t) \\ \nu_2(t) \\ \vdots \\ \nu_N(t) \end{bmatrix}, \qquad \begin{aligned} \Phi &= \begin{bmatrix} \phi_1 & \phi_2 & \dots & \phi_N \end{bmatrix} \\ \Psi &= \begin{bmatrix} \psi_1 & \psi_2 & \dots & \psi_N \end{bmatrix} \end{aligned}$$

the transition between states α and β described in Eqs.(2.10) and (2.11) can be rewritten in vector form as follows

$$\begin{aligned} \alpha \longrightarrow \beta \qquad & \begin{cases} \nu(t^+_{\alpha\beta}) &= \Psi^T M \Phi \, \eta(t^-_{\alpha\beta}) - \Psi^T M X_0(t^+_{\alpha\beta}) \\ \dot{\nu}(t^+_{\alpha\beta}) &= \Psi^T M \Phi \, \dot{\eta}(t^-_{\alpha\beta}) \end{cases} \\ \beta \longrightarrow \alpha \qquad & \begin{cases} \eta(t^+_{\beta\alpha}) &= \Phi^T M \Psi \, \nu(t^-_{\beta\alpha}) + \Phi^T M X_0(t^+_{\alpha\beta}) \\ \dot{\eta}(t^+_{\beta\alpha}) &= \Phi^T M \Psi \, \dot{\nu}(t^-_{\beta\alpha}) \end{cases} \end{aligned} \tag{2.12}$$

It is clear that the matrix $\Psi^T M \Phi$ and its transpose $\Phi^T M \Psi$ are central to the transformation between states α and β. For this reason these matrices are chosen as measures of modal disparity.

2.4 Numerical Example

2.4.1 Modeling

We consider the axial vibration of a linear rod with a constant circular cross-section, as shown in Fig.2.1. The rod is fixed at one end and free at the other end. An electromagnetic brake attached to the free end of the rod enables it to be fixed at any desired time. In stiffness state α the brake is free whereas in state β the brake is locked. The differential equation describing the motion of the system is

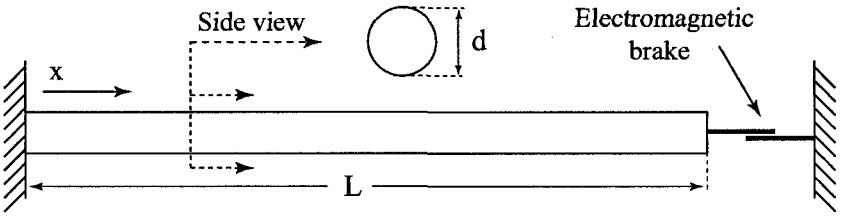

Figure 2.2. A flexible rod

$$\rho A\ddot{u} - EAu'' = 0 \tag{2.13}$$

for all $x \in (0, L)$. The boundary conditions are

$$u(0,t) = 0$$

$$\text{State } \alpha \quad u'(L,t) = 0$$

$$\text{State } \beta \quad u(L,t) = \delta$$

In Eq.(2.13), E is the Young's modulus of elasticity, ρ is the material density and A is the cross-section area of the rod. In the boundary conditions, δ is the extension of the locked end of the bar in state β. The bar is modeled with N linear standard finite elements, see [28] for example. Each node has one displacement dof denoted by $u(x,t)$. If L_e denotes the length of an element, the elementary mass and stiffness matrices take the form

$$M_e = \frac{\rho A L_e}{6}\begin{bmatrix} 2 & 1 \\ 1 & 2 \end{bmatrix}, \qquad K_e = \frac{EA}{L_e}\begin{bmatrix} 1 & -1 \\ -1 & 1 \end{bmatrix}$$

The modeling of both states is facilitated by the use of a linear spring as shown in

Fig.2.3. It is attached between the free end of the bar and the wall. In state α the end is free, *i.e.* $k_s = 0$. In state β, it is fixed and this is modeled by setting $k_s = \infty$, *i.e.*, setting k_s to some large number. The equations of motion of the system in both states will take the form as in Eqs.(2.1) and (2.2).

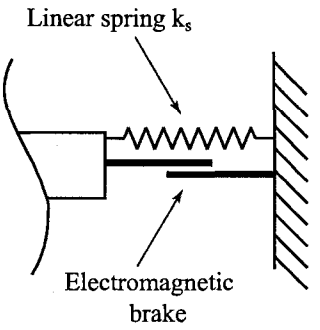

Figure 2.3. The electromagnetic brake model

2.4.2 Simulations

The material and geometric properties of the rod are assumed to be those given in Tab.2.1. The rod was modeled by 300 finite elements, *i.e.*, $N = 300$. The natural

Table 2.1. Material and geometric properties of the beam in Fig.2.2

Material	Rubber
Young's Modulus	10 MPa
Density	600 Kg/m^3
Cross section Area	π 0.05^2 m^2
Length	4.0 m

frequencies of the first 6 modes of the rod in each state are tabulated in Tab.2.2. The normalized mode shapes of the rod in the two stiffness states are shown in Fig.2.4. It is important to note that the mode shapes in state β do not depend on the deflection

of the end of the rod (δ) in the brake locked configuration. This fact is justified as follows. The extension of the end of the rod will move the equilibrium of the system to a new position X_0, $X_0 \neq 0$. If the change of variable $Y = (X - X_0)$ is used, the new system will have the same mass and stiffness matrices as given by Eq(2.2) for all values of δ. The only change will be the level of potential energy $\frac{1}{2}X_0^T(t_{\alpha\beta}^+)KX_0(t_{\alpha\beta}^+)$ that will be stored in the system.

Table 2.2. Natural frequencies of the beam in the two stiffness states

$\omega_{\alpha i}$, $\omega_{\beta i}$ (Hz)		mode number, i					
		$i=1$	$i=2$	$i=3$	$i=4$	$i=5$	$i=6$
stiffness state	α	8.07	24.21	40.34	56.48	72.62	88.76
	β	16.14	32.27	48.41	64.55	80.69	96.83

$$\Psi^T M \Phi = \begin{pmatrix} -0.849 & 0.509 & 0.121 & 0.057 & -0.033 & 0.022 \\ 0.340 & 0.728 & -0.566 & -0.154 & 0.078 & -0.048 \\ -0.218 & -0.283 & -0.694 & 0.588 & -0.170 & 0.090 \\ 0.162 & 0.185 & 0.261 & 0.679 & 0.600 & -0.179 \\ 0.129 & 0.140 & 0.170 & 0.250 & -0.670 & -0.606 \\ -0.107 & -0.113 & -0.128 & -0.161 & 0.242 & -0.664 \end{pmatrix} \tag{2.14}$$

Using a 6-mode model of the system in each state, we consider the scenario where the system is vibrating in state α starting from the following initial conditions:

$$\eta(0) = \begin{bmatrix} 0.00 & 0.00 & 0.00 & 0.00 & 0.00 & 0.00 \end{bmatrix}^T$$
$$\dot{\eta}(0) = \begin{bmatrix} 0.01 & 0.01 & 0.01 & 0.01 & 0.01 & 0.01 \end{bmatrix}^T.$$

After 3 seconds in state α, the brake is locked and as a result the system is transferred to state β. Using Eq.(2.10), the initial conditions in state β are calculated as follows:

$$\nu(3^+) = 1e^{-5} \begin{bmatrix} -5.67 & -3.85 & 1.68 & -1.34 & -0.28 & -1.24 \end{bmatrix}^T$$
$$\dot{\nu}(3^+) = 1e^{-2} \begin{bmatrix} -0.56 & -0.78 & -1.22 & -0.04 & -0.44 & 0.40 \end{bmatrix}^T.$$

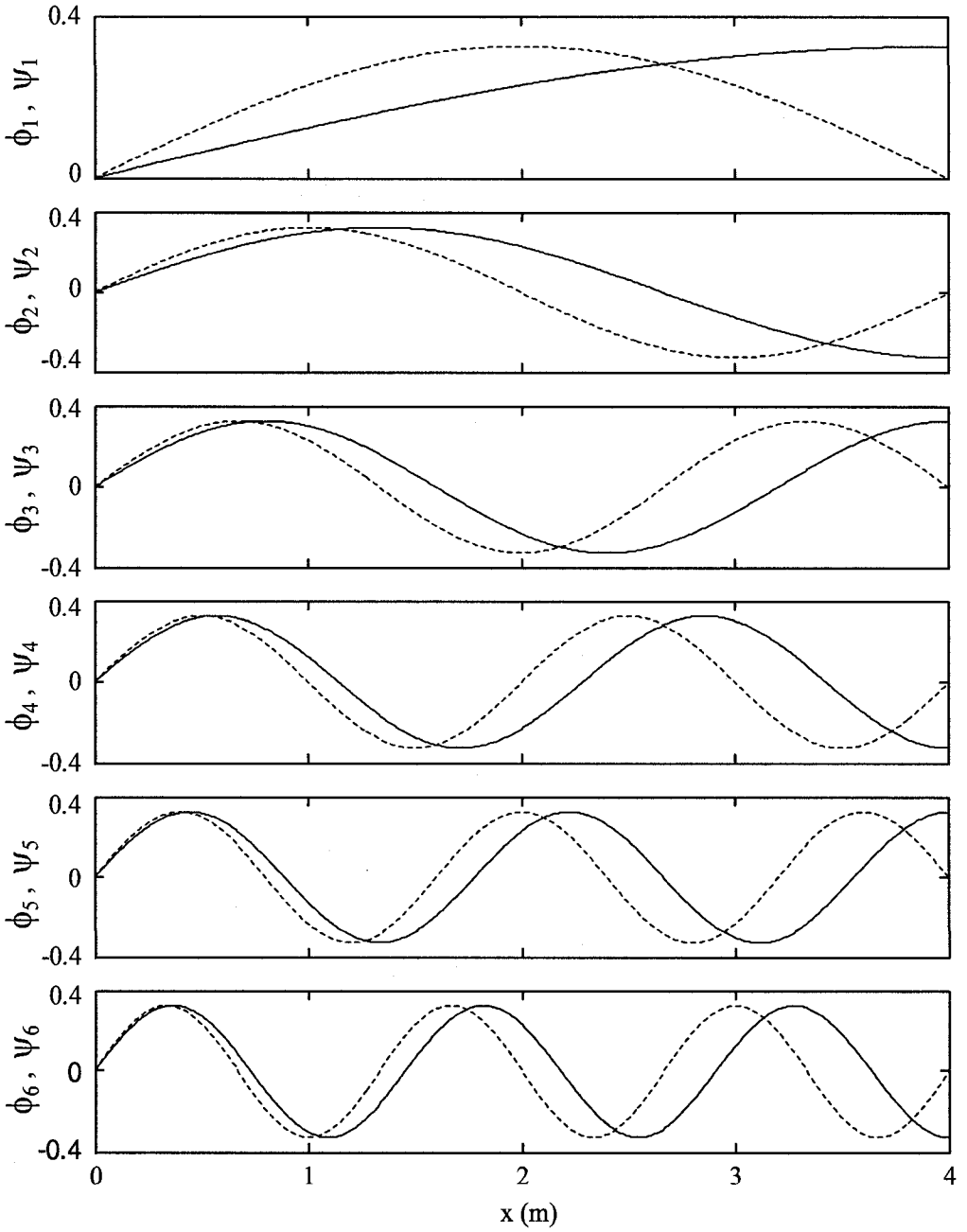

Figure 2.4. Mode shapes of the rod in the two stiffness states: the solid lines represent the ϕ_i's and the dashed lines represent the ψ_i's.

Here $\delta = 6.38e^{-5}\ m$ and if E_T is the total energy in the system, the energy stored in the system after application of the constraint is 0.133 E_T. After 3 seconds in state β the system is switched back to state α, the modal displacements and velocities are calculated using Eq.(2.11) as

$$\eta(6^+) = 1e^{-5}\left[\begin{array}{cccccc} 18.90 & -4.55 & 0.72 & 0.80 & -1.51 & 1.58 \end{array}\right]^T$$
$$\dot{\eta}(6^+) = 1e^{-2}\left[\begin{array}{cccccc} 0.38 & -0.63 & 1.09 & -0.83 & 0.54 & -0.08 \end{array}\right]^T.$$

A scheme illustrating modal energy redistribution during one cycle of constraint application and removal is shown in Fig.2.5. At the first transition 13.3% of the energy is stored as potential, 81.4% is redistributed between the first 6 modes of the system in state β and the remaining 5.3%, not shown here, is transferred to the higher modes. After removing the constraint, 91.2% of the total energy E_T is rearranged in the modes of the system in state α and 3.45% is transferred to the higher modes.

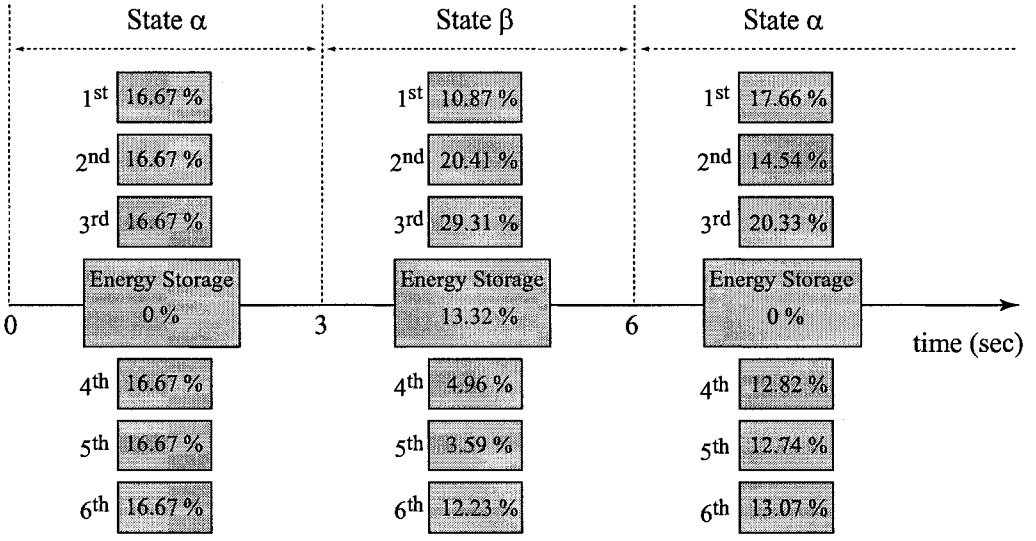

Figure 2.5. Modal energy redistribution in the bar after one cycle of constraint application and removal

2.5 Remarks

A method for modal energy redistribution was presented in this chapter. It was shown that modal energy of a vibrating system can be redistributed by stiffness variation, and specifically through cyclic application and removal of constraints. The amount of energy redistributed depends on the difference in the mode shapes of the structure in the two stiffness states. A measure of this difference in the mode shapes of the structure is defined as modal disparity and is quantified. In the next chapter we provide an experimental verification of modal disparity and demonstrate the potential for energy dissipation through modal energy redistribution.

CHAPTER 3

Experimental Verification Of Modal Disparity

3.1 Introduction

In this chapter we present experimental results to illustrate modal disparity in a structure due to change in stiffness. In an earlier work [1], [2], modal disparity of structures with variable stiffness was computed and simulation results of modal energy redistribution were provided. The objective of this chapter is to experimentally demonstrate modal energy redistribution in a clamped-clamped beam with a variable stiffness joint. A mathematical model of the beam using finite elements is presented in Section 3.2. The mechanics of stiffness variation is discussed in Section 3.3. Simulation results are presented in Section 3.4; they provide a benchmark for the experimental results presented in Section 3.5. Concluding remarks are provided in Section 3.6.

3.2 Modeling

In this section we review the finite element procedure to model the free vibration of a beam with a mid-span hinge, as shown in Fig.3.1. We assume that the hinge has a built in actuator enabling it to be locked or released at any desired time. Clamped at both ends, the beam is switched from one stiffness state to another by locking or

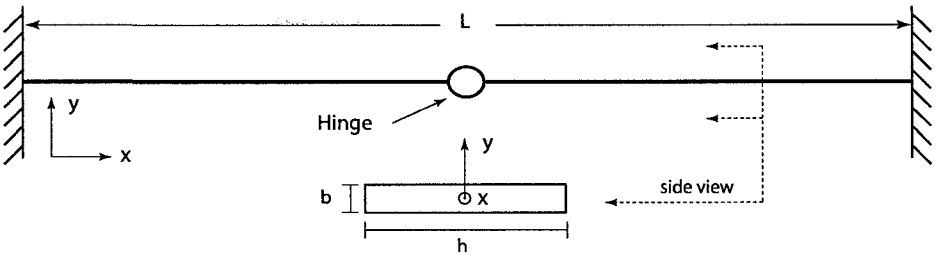

Figure 3.1. A clamped-clamped beam with a mid span hinge

releasing the hinge. Let A be the cross-sectional area and I be the area moment of inertia of the beam. Let ρ and E be the material density and modulus of elasticity of the beam, respectively. Assuming Euler-Bernoulli theory, the equation of motion of the beam in the x-y plane can be written as follows:

$$EI\,y''''(x,t) + \rho A\,\ddot{y}(x,t) = 0 \qquad \text{if } x \in (0, L/2) \text{ or } x \in (L/2, L) \tag{3.1}$$

The boundary conditions are

$$\begin{aligned} y(0,t) &= y(L,t) = 0 \\ y'(0,t) &= y'(L,t) = 0 \\ y((L/2)^-,t) &= y((L/2)^+,t) \\ y'''((L/2)^-,t) &= y'''((L/2)^+,t) \end{aligned}$$

The beam is in stiffness state α when the hinge is free and in stiffness state β when it is locked. The remaining boundary conditions needed to completely describe the behavior of the system in the two stiffness states are as follows:

$$\text{stiffness state } \alpha \qquad \begin{aligned} y''((L/2)^-,t) &= 0 \\ y''((L/2)^+,t) &= 0 \end{aligned}$$

$$\text{stiffness state } \beta \qquad \begin{aligned} y'((L/2)^-,t) &= y'((L/2)^+,t) \\ y''((L/2)^-,t) &= y''((L/2)^+,t) \end{aligned}$$

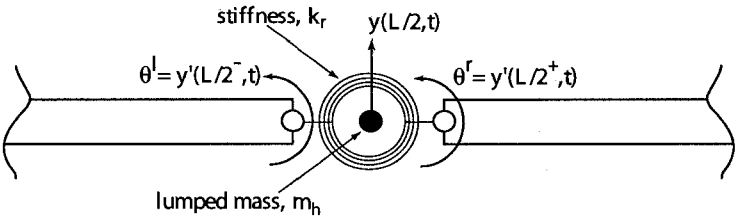

Figure 3.2. The hinge model

We model the beam by N standard (cubic) finite elements. Each element has two nodes with two dof[1] per node (translation in the y axis and rotation about the z axis). The modeling of the hinge in both states is facilitated by assuming that the node at $x = L/2$ has two rotational dof, θ^l and θ^r, corresponding to $y'(L/2^-,t)$ and $y'(L/2^+,t)$, respectively. When the hinge is free (stiffness state α), θ^l and θ^r are independent. However, when it is locked (stiffness state β) the constraint $\theta^l = \theta^r$ has to be enforced. This is achieved by adding a penalty of magnitude $\frac{1}{2}k_r\left(\theta^l - \theta^r\right)^2$ to the strain energy, that is, by adding a rotational stiffness between θ^l and θ^r as shown in Fig.3.2.

$$K_r = k_r \begin{bmatrix} 1 & -1 \\ -1 & 1 \end{bmatrix} \tag{3.2}$$

To account for the hinge model, the stiffness matrix in Eq.(3.2) is added to the global stiffness matrix. In the stiffness state α, the parameter k_r is set to zero and in stiffness state β, it is set to a large positive value. The finite element model has $(2N-1)$ dof. The hinge model is shown schematically in Fig.3.2, where the hinge mass is accounted for by the addition of a lumped mass m_h at the central node.

[1]degrees-of-freedom

3.3 Stiffness Change Mechanism

As mentioned in the previous section, the transition from stiffness state α to stiffness state β is accomplished by an actuator, having the capability to lock the hinge. This transition is assumed to occur over a brief interval of time and results in the application of an action-reaction pair of impulsive moments to the middle node, as shown in Fig.3.3. Furthermore, by sensing the state of the beam, the hinge is locked only when the beam is passing through its equilibrium configuration. Let $t^-_{\alpha\beta}$ and $t^+_{\alpha\beta}$ denote the beginning and the end of this brief transition period. The effect of the impulsive moments can be mathematically described by the relations

$$\begin{aligned} Y(t^-_{\alpha\beta}) &= Y(t^+_{\alpha\beta}) \\ M\dot{Y}(t^-_{\alpha\beta}) + I_{\alpha\to\beta} &= M\dot{Y}(t^+_{\alpha\beta}) \end{aligned} \tag{3.3}$$

where M is the mass matrix and Y is the vector of nodal dof. $I_{\alpha\to\beta}$, the impulse vector, takes the form shown below:

$$I_{\alpha\to\beta} = [0, \cdots, C, -C, \cdots, 0]^T, \qquad C = \int_{t^-_{\alpha\beta}}^{t^+_{\alpha\beta}} \tau(t)\, dt \tag{3.4}$$

The nonzero entries of $I_{\alpha\to\beta}$ correspond to the coordinates θ^l and θ^r, where C is the impulse and τ is the impulsive moment. $Y(t^+_{\alpha\beta})$ and $\dot{Y}(t^+_{\alpha\beta})$ are the displacements and velocities in stiffness state β at the end of the transition period. They are calculated from the values of $Y(t^-_{\alpha\beta})$ and $\dot{Y}(t^-_{\alpha\beta})$ using Eq.(3.3). Although C is an unknown, Eq.(3.3) can be solved since two elements of $\dot{Y}(t^+_{\alpha\beta})$, namely $\dot{\theta}^l$ and $\dot{\theta}^r$, are equal. The transition from stiffness state β to stiffness state α is accomplished by releasing the hinge. If $t^-_{\beta\alpha}$ and $t^+_{\beta\alpha}$ denote the beginning and the end of this brief transition period, the beam displacements and velocities vectors just prior to and right after the release of the hinge are the same, *i.e.*

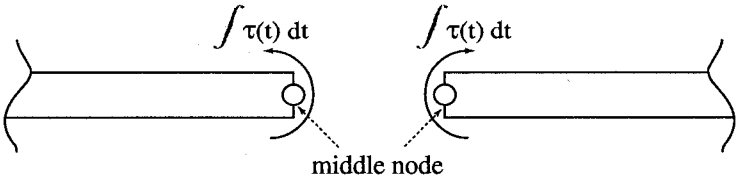

Figure 3.3. Action-reaction pair of impulsive moments

$$\begin{aligned} Y(t_{\beta\alpha}^{-}) &= Y(t_{\beta\alpha}^{+}) \\ \dot{Y}(t_{\beta\alpha}^{-}) &= \dot{Y}(t_{\beta\alpha}^{+}) \end{aligned} \tag{3.5}$$

The beam behavior at the transition from one state to another is described by equations (3.3) and (3.5). Eq.(3.1) describe the beam behavior at all other times as a clamped-clamped beam with a frictionless hinge at mid span (in stiffness state α) or a clamped-clamped beam (in stiffness state β). With this notation, the stiffness parameter k_r (introduced in section 3.2) can be defined as follows

$$k_r = \begin{cases} 0 & \text{stiffness state } \alpha \\ k_\infty & \text{stiffness state } \beta \end{cases}$$

where k_∞ is some large positive number chosen to enforce the constraint $\theta^l = \theta^r$.

3.4 Modal Space

Let ϕ_i and ψ_i denote the i-th normalized mode shapes of the beam in stiffness state α and stiffness state β, respectively, and let $\mu_i(t)$ and $\nu_i(t)$ denote the corresponding modal displacements. In the two stiffness states, the vector of nodal dof can be expressed as

$$Y(t) = \begin{cases} \sum_{i=1}^{2N-1} \mu_i(t)\,\phi_i & \text{stiffness state } \alpha \\ \\ \sum_{i=1}^{2N-1} \nu_i(t)\,\psi_i & \text{stiffness state } \beta \end{cases} \tag{3.6}$$

The transition from stiffness state α to stiffness state β, mathematically described by Eq.(3.3), can now be rewritten as

$$\begin{aligned} \sum_{i=1}^{2N-1} \mu_i(t_{\alpha\beta}^-)\,\phi_i &= \sum_{i=1}^{2N-1} \nu_i(t_{\alpha\beta}^+)\,\psi_i \\ M \sum_{i=1}^{2N-1} \dot{\mu}_i(t_{\alpha\beta}^-)\,\phi_i + I_{\alpha\to\beta} &= M \sum_{i=1}^{2N-1} \dot{\nu}_i(t_{\alpha\beta}^+)\,\psi_i \end{aligned} \tag{3.7}$$

Using Eq.(3.7), the modal displacements and velocities, $\nu_j(t_{\alpha\beta}^+)$ and $\dot{\nu}_j(t_{\alpha\beta}^+)$, can be expressed in terms of $\mu_j(t_{\alpha\beta}^-)$ and $\dot{\mu}_j(t_{\alpha\beta}^-)$ as follows

$$\begin{aligned} \nu_j(t_{\alpha\beta}^+) &= \sum_{i=1}^{2N-1} \psi_j^T M \phi_i\,\mu_i(t_{\alpha\beta}^-) \\ \dot{\nu}_j(t_{\alpha\beta}^+) &= \sum_{i=1}^{2N-1} \psi_j^T M \phi_i\,\dot{\mu}_i(t_{\alpha\beta}^-) \end{aligned} \tag{3.8}$$

In the derivation of Eq.(3.8) from Eq.(3.7), we used the identity $\psi_j^T\, I_{\alpha\to\beta} = 0$. This is true since the entries of ψ_j, $j = 1, 2, \cdots (2N-1)$, corresponding to the nonzero entries of $I_{\alpha\to\beta}$, namely, θ^l and θ^r are equal.

Using the same procedure as above, the transition from stiffness state β to stiffness state α can be obtained from Eq.(3.5) as follows

$$\begin{aligned} \mu_j(t_{\beta\alpha}^+) &= \sum_{i=1}^{2N-1} \phi_j^T M \psi_i\,\nu_i(t_{\beta\alpha}^-) \\ \dot{\mu}_j(t_{\beta\alpha}^+) &= \sum_{i=1}^{2N-1} \phi_j^T M \psi_i\,\dot{\nu}_i(t_{\beta\alpha}^-) \end{aligned} \tag{3.9}$$

If we define $\Phi = \left[\phi_1, \phi_2, \cdots, \phi_{(2N-1)}\right]$ and $\Psi = \left[\psi_1, \psi_2, \cdots, \psi_{(2N-1)}\right]$, it is clear from Eqs.(3.8) and (3.9) that elements of the matrix $\Psi^T M \Phi$ define the mapping between modal coordinates during the transition from stiffness state α to stiffness state β. The transposed matrix, $\Phi^T M \Psi$, defines the mapping between modal coordinates during

the transition from stiffness state β to stiffness state α. These matrices will be identity matrices if the two stiffness states are the same and any deviation from the identity structure is a measure of modal disparity between the two stiffness states [1].

3.5 Numerical Example

Consider the beam in Fig.3.1 with the material and geometric properties in Table 3.1. The mode shapes of the first four modes of the beam in the two stiffness states are

Table 3.1. Material and geometric properties of the beam in Fig.3.1

Material	Aluminum
Young's Modulus	71 GPa
Density	2710 Kg/m^3
Cross section Area	$0.05 \times 0.0023 m^2$
Length	2.0 m
Hinge mass	0.182 Kg

shown in Fig.3.3, and their corresponding natural frequencies in Table 3.2. The even numbered modes in the two stiffness states are identical. This is true since the hinge is located at mid-span where the even numbered modes have zero curvature therefore they will not be affected by the state of the hinge, *i.e.* locked or released.

Table 3.2. Natural frequencies of the beam in the two stiffness states

$\omega_{\alpha i}$, $\omega_{\beta i}$ (Hz)		mode number, i			
		$i=1$	$i=2$	$i=3$	$i=4$
stiffness state	α	1.29	8.34	9.52	27.0
	β	2.30	8.34	14.68	27.0

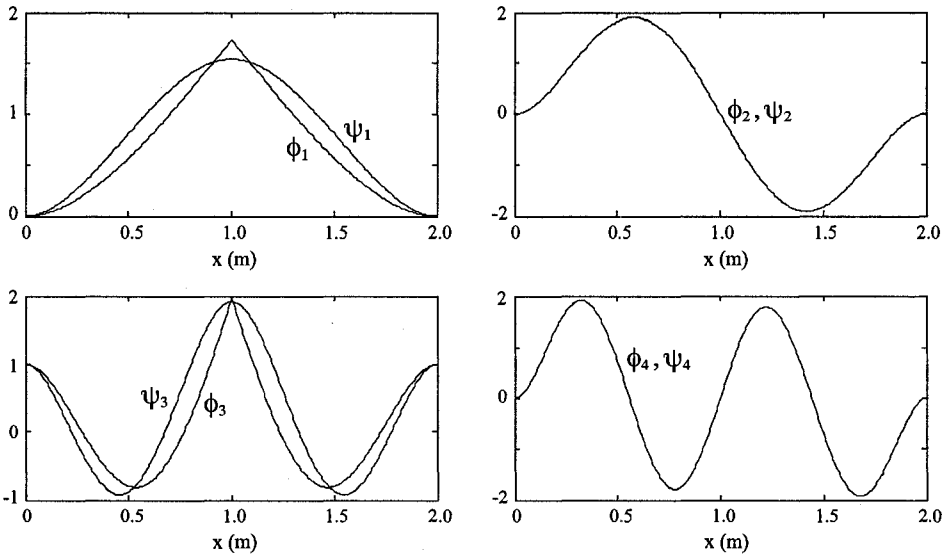

Figure 3.4. Mode shapes of the beam in the two stiffness states

Using modal truncation, the matrix measure of modal disparity, $\Psi^T M\Phi$, is computed using the first four modes as follows

$$\Psi^T M\Phi = \begin{pmatrix} 0.980 & 0.000 & 0.153 & 0.000 \\ 0.000 & 1.000 & 0.000 & 0.000 \\ 0.139 & 0.000 & 0.949 & 0.000 \\ 0.000 & 0.000 & 0.000 & 1.000 \end{pmatrix} \tag{3.10}$$

In the matrix $\Psi^T M\Phi$, the fact that second and fourth rows and columns maintain the identity structure, is an indication that the even-numbered modes in the two stiffness states are identical. However, the non-unity value of the diagonal elements and nonzero elements in the off-diagonal entries of odd-numbered rows and columns indicate the presence of modal disparity between the odd-numbered modes of the two stiffness states.

To illustrate modal energy redistribution between odd-numbered modes in the two stiffness states, we consider the scenario where the beam is initially in stiffness state α and vibrating purely in the third mode with a maximum amplitude $\mathcal{X}_\alpha$. Ignoring

damping, the total energy in the system is equal to $E_\alpha = 0.5\,\mathcal{X}_\alpha^2\,\omega_{\alpha 3}^2$. It is assumed that the beam is switched to state β when it passes through its neutral position. The modal displacements right after locking the hinge are zeros $\nu_i(t_{\alpha\beta}^+) = 0$, since $\mu_i(t_{\alpha\beta}^-) = 0$. The modal velocities right after switching to stiffness states β can be computed from Eq.(3.8) as follows

$$\begin{bmatrix} \dot{\nu}_1(t_{\alpha\beta}^+) \\ \dot{\nu}_2(t_{\alpha\beta}^+) \\ \dot{\nu}_3(t_{\alpha\beta}^+) \\ \dot{\nu}_4(t_{\alpha\beta}^+) \end{bmatrix} = \begin{pmatrix} 0.980 & 0.000 & 0.153 & 0.000 \\ 0.000 & 1.000 & 0.000 & 0.000 \\ 0.139 & 0.000 & 0.949 & 0.000 \\ 0.000 & 0.000 & 0.000 & 1.000 \end{pmatrix} \begin{bmatrix} 0 \\ 0 \\ \mathcal{X}_\alpha\,\omega_{\alpha 3} \\ 0 \end{bmatrix} \tag{3.11}$$

Clearly, the energy of the beam is redistributed in modes 1 and 3 in stiffness state β. The maximum amplitudes of these modes are

$$\begin{aligned} \mathcal{X}_{\beta 1} &= 0.153\mathcal{X}_\alpha(\omega_{\alpha 3}/\omega_{\beta 1}) = 0.633\mathcal{X}_\alpha \\ \mathcal{X}_{\beta 3} &= 0.949\mathcal{X}_\alpha(\omega_{\alpha 3}/\omega_{\beta 3}) = 0.615\mathcal{X}_\alpha \end{aligned} \tag{3.12}$$

The modal energy in modes 1 and 3 are easily calculated as follows.

$$\begin{aligned} E_{\beta 1} &= \tfrac{1}{2}\mathcal{X}_{\beta 1}^2\omega_{\beta 1}^2 = \tfrac{1}{2}\,0.153^2\mathcal{X}_\alpha^2\,\omega_{\alpha 3}^2 = 0.153^2\,E_\alpha \\ E_{\beta 3} &= \tfrac{1}{2}\mathcal{X}_{\beta 3}^2\omega_{\beta 3}^2 = \tfrac{1}{2}\,0.949^2\mathcal{X}_\alpha^2\,\omega_{\alpha 3}^2 = 0.949^2\,E_\alpha \end{aligned} \tag{3.13}$$

These results will be validated through experiments in the next section.

3.6 Experimental Verification

The experimental hardware is shown in Fig.3.5. The beam has a pair of piezoelectric transducers[2] mounted on each side at a distance of 5.0 cm from one of the clamped ends. These transducers are used for excitation. A single piezoelectric strain sensor[3] is mounted on the beam at a distance of 5.0 cm from the other clamped end. The

[2]product of Mide Technology Corporation
[3]product of PCB Piezotronics

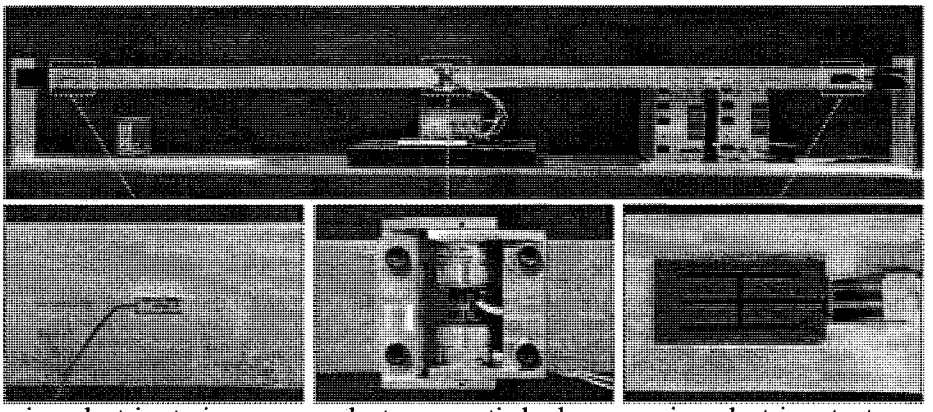

Figure 3.5. Experimental hardware

position of the sensor and actuators are chosen to ensure high degree of controllability and observability of the first three modes of the system. The material and geometric properties of the beam in the experimental setup are the same as those used in simulations and provided in Table 3.1. In this table, the hinge mass includes the mass of the electromagnetic brakes[4], shown in Fig.3.5, used for locking and releasing the hinge. In our experiments, we chose to investigate energy redistribution between the

Table 3.3. Natural frequencies of the beam in the two stiffness states, determined experimentally

$\omega_{\alpha i}$, $\omega_{\beta i}$ (Hz)		mode number, i		
		$i=1$	$i=2$	$i=3$
stiffness state	α	1.40	8.24	9.70
	β	2.37	8.20	13.90

first three modes of the beam. This was motivated by the fact that modal disparity can be adequately demonstrated by the first three modes and estimation of the higher modes are more prone to inaccuracies. The first three natural frequencies were ex-

[4]product of Inertia Dynamics

perimentally determined for both stiffness states and are provided in Table 3.3. The piezoelectric transducers were used to excite the beam and the strain sensor was used to measure beam vibration. The natural frequencies were identified as the frequencies of excitation that resulted in maximal amplitude of vibration. The experimentally determined values show good agreement with the numerically computed values in Table 3.2. We first present experimental results for two cases where the beam was initially in stiffness state α (hinge released) and switched to stiffness state β (hinge locked). For the first case, Case A, the beam was excited at its second natural frequency in stiffness state α. The stiffness of the beam was switched after termination of excitation and the results, shown in Fig.3.6, indicate that the beam vibrates primarily in its second mode in stiffness state β. This is expected since the second mode of the two stiffness states are identical. This can be verified from the elements of the second column vector of the modal disparity matrix $\Psi^T M \Phi$ in Eq.(3.10). All entries of this vector are zero except for the second entry, which is unity. For the second case, Case B, the beam was excited at its third natural frequency in stiffness state α. Its stiffness was switched after termination of excitation and the results are shown in Fig.3.7. Since the first and third elements of the third column vector of $\Psi^T M \Phi$ are nonzero, the beam vibrates in its first and third natural frequencies in stiffness state β. The amplitude of these modes, immediately after the switch, can be computed based on our analysis in the last section. These values and the values obtained from experiments are both presented in Table 3.4 and they show good conformity. The plots in Fig.3.7 indicate a small presence of the second mode in both stiffness states. It is logical to infer that excitation of the beam introduced the second mode in stiffness state α and energy associated with this mode transferred directly to the second mode in stiffness state β. For the sake of completeness, we present experimental results for one case where the beam was initially in stiffness state β (hinge locked) and switched to stiffness state α (hinge released). The results for this case, which we denote as

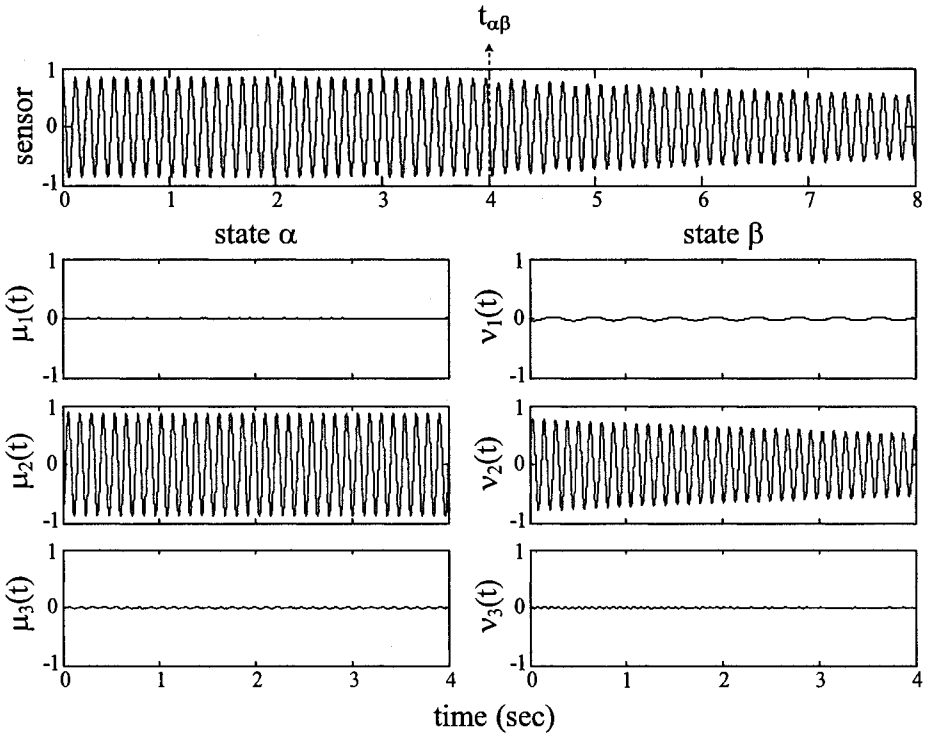

Figure 3.6. Energy redistribution between modes for Case A

Case C, are shown in Fig.3.8 and summarized in Table 3.4. For this case, the beam vibrates in its second mode in stiffness state β and energy associated with this mode is entirely transferred to the second mode in stiffness state α, upon switching. The results for this case are therefore quite similar to that of Case A. The amplitude of the third mode in stiffness state α could not be measured accurately and is marked "xxx" in Table 3.4. The difficulty of the measurement was due to its small magnitude coupled with waxing and waning due to beating. The beating phenomenon can be attributed to the close proximity of the second and third natural frequencies of the beam in stiffness state α.

3.7 Remarks

The investigation in this chapter has confirmed that changes in structural stiffness result in modal disparity, and that this disparity permits energy to be transferred

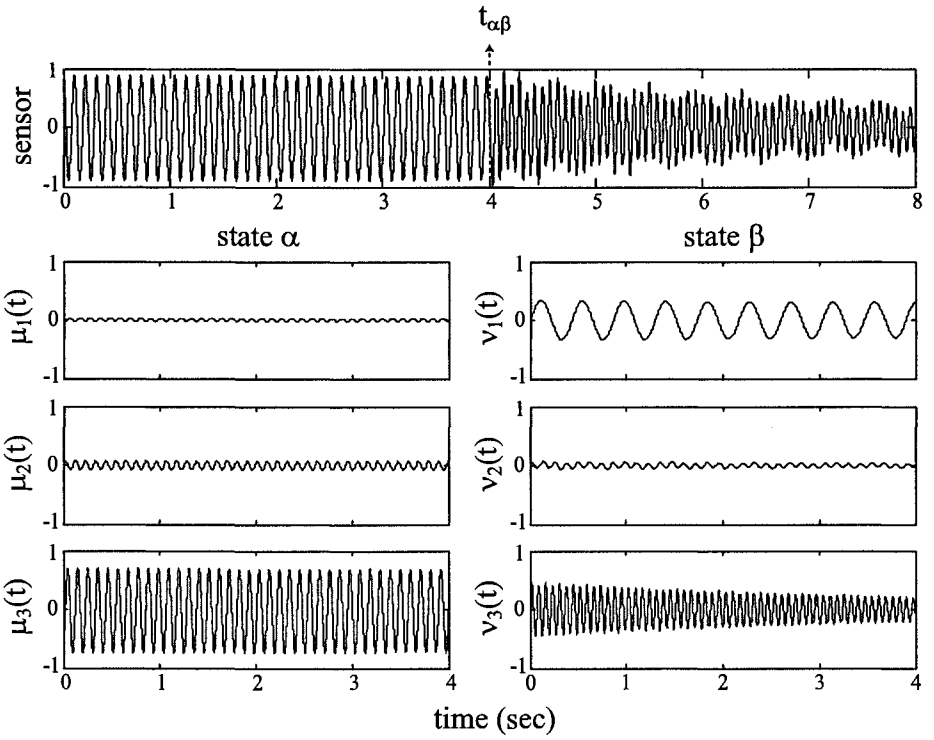

Figure 3.7. Energy redistribution between modes for Case B

between different sets of spatial modes in a given structure. Finite element based analysis and systematic experiments have demonstrated that the phenomena can be modeled and quantitatively predicted. One of the keys in the modeling is to properly account for the physics of the transition between the different stiffness states, which results in the correct mapping of the modal energies from one set of modes to another. With these tools in hand, it should be possible to design structural systems with built-in mechanisms for stiffness variation for favorable modal disparity, and to predict the efficacy of various proposed switching schemes. In the next chapter we present a semi-active control strategy where the stiffness of the structure is actively varied to transfer energy from the low-frequency modes to the high-frequency modes where it can be dissipated naturally and quickly.

Table 3.4. Modal amplitudes immediately before and after switchings

	Stiffness switch	amplitudes before switch mode number i			amplitudes after switch actual/expected values		
		$i=1$	$i=2$	$i=3$	$i=1$	$i=2$	$i=3$
Case A	$\alpha \rightarrow \beta$	0.01	0.88	0.01	0.02/0.01	0.80/0.88	0.01/0.01
Case B	$\alpha \rightarrow \beta$	0.02	0.07	0.68	0.36/0.42	0.05/0.07	0.44/0.45
Case C	$\beta \rightarrow \alpha$	0.00	0.84	0.01	0.01/0.00	0.79/0.84	xxx/0.00

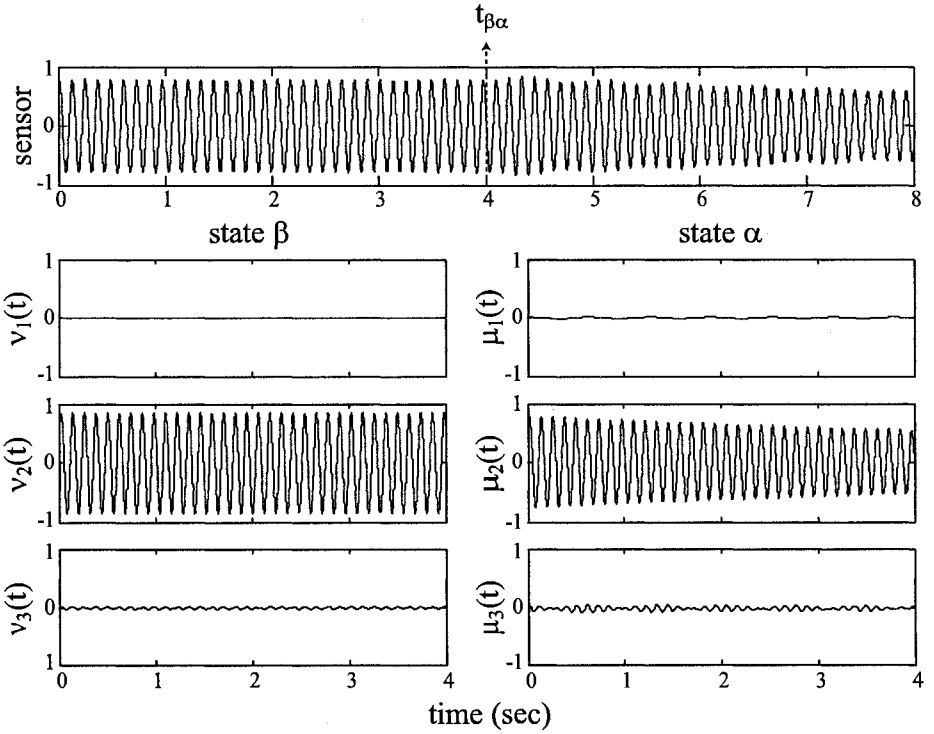

Figure 3.8. Energy redistribution between modes for Case C

CHAPTER 4

Energy Dissipation In Dynamical Systems Through Sequential Application And Removal Of Constraints

4.1 Introduction

Energy dissipation is the primary objective of many control problems in dynamical systems. For such problems, we explore the feasibility of energy dissipation through sequential application and removal of constraints. We illustrate our basic idea with the example of the three dof[1] mass-spring system, shown in Fig.4.1. In Fig.1, the

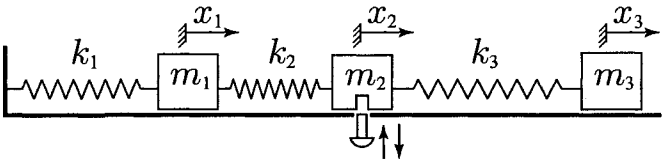

Figure 4.1. A three dof mass-spring system

displacements of the three masses are denoted by x_1, x_2, and x_3. A constraint $x_2 = 0$ is applied by instantaneously pushing the pin into the slot in mass m_2 and removed by pulling the pin out of the slot. The application of the constraint requires the instantaneous position of mass m_2 to satisfy $x_2 = 0$ but removal of the constraint

[1]degrees-of-freedom

can occur at any time. The application of the constraint results in an instantaneous reduction in energy of the overall system by an amount equal to the kinetic energy of mass m_2. The removal of the constraint does not alter the energy of the system but enables the constraint to be applied again for further reduction of energy. Except in special situations[2], sequential application and removal of the constraint will ultimately reduce the energy of the system to zero. On reading this example, two questions arise:

1. What happens to the kinetic energy of m_2 when the constraint is applied ?
2. Can one generalize this idea to remove energy from dynamical systems through sequential application and removal of constraints ?

The answer to the first question is provided in Section 4.2 but it requires that we model the pin and/or mass as deformable bodies. This is further explained with the help of the next example of direct central impact, which can be found in almost any textbook in dynamics. The answer to the second question is the subject of this chapter and is discussed in the remaining sections.

Consider the two *particles* A and B, of mass m_A and m_B, moving to the right along the same straight line with velocities v_A and v_B, as shown in Fig.4.1. If we assume that $v_A > v_B$, particle A will eventually strike particle B. Upon impact, the two particles will *deform* and at the end of the period of deformation they will have the same velocity u. A period of restitution will then take place and at the end of this period, the two particles will have velocities v'_A and v'_B. The velocities v'_A and v'_B can be obtained by solving the two equations

[2]An example of a special situation is where the system of masses move in a manner that maintains $x_2(t) \equiv 0$; this will occur if one of the modes have a zero displacement for mass m_2 and the system vibrates in that mode.

$$\begin{aligned} m_A v_A + m_B v_B &= m_A v'_A + m_B v'_B \\ (v'_B - v'_A) &= e\,(v_A - v_B) \end{aligned}$$

The first equation corresponds to conservation of linear momentum. The second equation relates the relative velocities of the particles, before and after impact, via the coefficient of restitution, $e \in [0, 1]$. In regards to this standard textbook

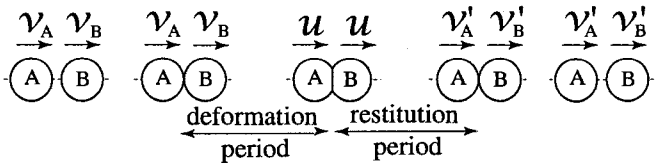

Figure 4.2. Direct central impact between two masses

explanation of the impact phenomenon, we wish to make the observation that initially the two masses are assumed to be rigid bodies, and hence they are referred to as particles, but later they are assumed to undergo deformation, in contradiction with the initial assumption of rigidity. In reality, the masses are deformable bodies and their deformation excites their flexible body modes if the material is elastic. The rigid body assumption, routinely made, simply implies that the flexible body modes correspond to high frequencies and are not relevant to the problem involving the rigid body motion of the masses after the restitution period.

Under the implicit assumption that the masses are deformable bodies, it is useful to discuss the two special cases corresponding to $e = 0$ and $e = 1$. When $e = 0$, the two masses have zero relative velocity after impact and this is referred to as "perfectly plastic impact". In the absence of restitution, the masses undergo plastic deformation. Work is done during plastic deformation and hence the kinetic energy of the masses after impact is less than that before impact. For $e = 1$, the masses have the maximal relative velocity after impact, equal to that

before impact. In this case of "perfectly elastic impact", some of the kinetic energy is stored as potential energy during deformation of the masses. The stored potential energy is completely converted back to kinetic energy during restitution and consequently the kinetic energy of the masses is the same before and after impact.

In this chapter we are interested in the removal of energy in "perfectly elastic" systems and thus we eliminate the possibility of permanent or plastic deformation. For the two-mass example, this implies no loss in kinetic energy and this can be simply attributed to the fact that the motion of the masses A and B are unconstrained after impact. To understand the loss of kinetic energy due to application of a constraint, as in the case of our 3-dof mass spring system, we consider a variation of the two-mass problem next.

4.2 Energy Loss due to Application of a Constraint

Consider the problem of direct central impact where the two masses are perfectly elastic, but, by virtue of some mechanism, the masses remain coalesced after they make contact. This scenario, depicted in Fig.4.3, will result from application of the constraint $(x_A - x_B) = 0$, where x_A and x_B are the position coordinates of the masses. In this scenario, conservation of momentum dictates that the velocity of the two masses after contact will be

$$\begin{aligned} v'_A &= u - \delta \frac{m_B}{(m_A + m_B)} \\ v'_B &= u + \delta \frac{m_A}{(m_A + m_B)} \end{aligned} \tag{4.1}$$

where u is the velocity of the center of mass, an invariant of the motion, has the expression

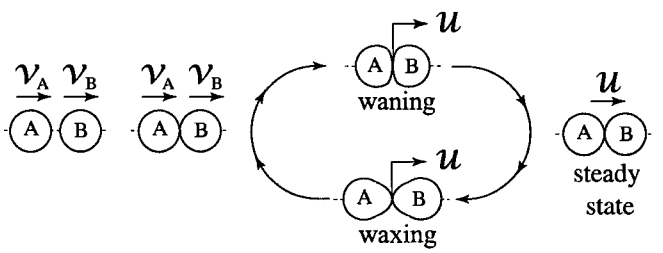

Figure 4.3. Scenario depicting two masses that stay connected after impact

$$u = \frac{m_A v_A + m_B v_B}{m_A + m_B} \tag{4.2}$$

and δ has the dimension of m/sec, and assumes a positive value during waxing, a negative value during waning, and a zero value at points of maximum deformation.

From Eqs.(4.1) and (4.2), the kinetic energy of the masses after contact can be computed to be

$$\frac{1}{2}m_A {v'_A}^2 + \frac{1}{2}m_B {v'_B}^2 = \frac{1}{2}(m_A + m_B)u^2 + \frac{1}{2}\frac{m_A m_B}{(m_A + m_B)}\delta^2 \tag{4.3}$$

The second term on the right hand side of Eq.(4.3) denotes the kinetic energy that is converted into potential energy during deformation, and converted back into kinetic energy when the masses regain their original shape. This cyclic conversion between kinetic and potential energy is possible due to excitation of the flexible modes of the masses, and this process would continue perpetually if there were no modal damping. In reality, the high-frequency flexible modes have high modal damping, and as a result the energy is gradually dissipated through conversion into heat. From the maximum absolute value of δ, which corresponds to $e = 1$, the total amount of energy dissipated can be shown to be

$$\frac{1}{2}\frac{m_A m_B}{(m_A + m_B)} |\delta|^2_{max} = \frac{1}{2}\frac{m_A m_B}{(m_A + m_B)}(v_A - v_B)^2$$

When all of this energy is dissipated at steady state, the two masses move together with the common velocity u, as shown in Fig.4.3. In contrast with the scenario depicted in Fig.4.2, where zero relative velocity of the masses after impact implies plastic deformation, the two masses here retain their original shape. Clearly, the application of a constraint for a finite duration of time results in a "perfectly plastic impact" behavior for "perfectly elastic" material property.

4.3 Relation to Prior Work

It is clear from our discussion in Section 4.2 that application of a constraint in a perfectly elastic finite dof system results in motion identical to a perfectly plastic impact. This dissipates mechanical energy and provides the opportunity for energy removal through sequential application and removal of constraints. Although such a method of energy dissipation has not been explored in the literature, there are many papers on energy dissipation using impact dampers. The pioneering work was done by Paget [29] for vibration reduction in turbine blades. This motivated the analytical studies by Lieber and Jensen [30], Grubin [31], and Warburton [32] on impact damping in single dof systems. The extension of this work includes analytical and experimental investigations of multi-unit impact dampers [33], and the effect of impact dampers on multi-dof systems [34], [35], [36], and continuous systems [37], [38]. There is a large volume of literature on impact dampers, and in that work, impact is a result of a physical collision. The approach presented in this chapter is fundamentally different in that the physical collision is followed by coalescence, as opposed to separation. The coalescence causes changes in natural frequencies and mode shapes of the system and results in energy transfer from one set of modes to another. For finite-dof systems,

the coalesced state also has fewer modes due to fewer dof and this "modal truncation" results in loss of kinetic energy. The modal description of impact and redistribution of energy due to application of a constraint has been verified experimentally for a clamped-clamped beam in chapter 3, and in this chapter we generalize the idea for finite-dof systems.

4.4 Finite DOF Linear Systems

In this section we investigate energy dissipation in linear systems with finite dof through sequential application and removal of constraints. From our earlier discussion we know that application of a constraint will result in an impact and transfer of energy into flexible body modes of the system, where it will be dissipated. Our finite-dof assumption simply implies that the flexible modes are unmodeled; this is justified by the fact that the energy transferred to these modes decay rapidly and their high-frequency dynamics have negligible effect on the dynamics of the the rigid body dof.

4.4.1 Spatial coordinate description

Consider the N-dof linear system

$$M\ddot{X} + KX = 0 \tag{4.4}$$

where M and K are the N-dimensional mass and stiffness matrices and $X = [x_1, x_2, \cdots, x_N]^T$ is the vector of independent generalized coordinates. Upon application of a holonomic constraint, the dynamics of the system takes the form

$$\tilde{M}\ddot{Y} + \tilde{K}Y = 0 \tag{4.5}$$

where $\tilde{M}$ and $\tilde{K}$ are the $(N-1)$-dimensional mass and stiffness matrices and $Y = \left[y_1, y_2, \cdots, y_{(N-1)}\right]^T$ is the vector of independent generalized coordinates of the

constrained system. Both the unconstrained and constrained systems are assumed to be undamped since our objective is to investigate energy dissipation solely due to application of the constraint.

We denote the unconstrained system as state α and the constrained system as state β. The transition from state α to state β occurs over the brief interval of time when the constraint is applied. If $[t_{\alpha\beta}^-, t_{\alpha\beta}^+]$ denotes this transition interval, the effect of the transition can be mathematically described by the relations

$$X(t_{\alpha\beta}^+) = X(t_{\alpha\beta}^-) \tag{4.6}$$

$$M\dot{X}(t_{\alpha\beta}^+) = M\dot{X}(t_{\alpha\beta}^-) + I_{\alpha\to\beta} \tag{4.7}$$

and

$$Y(t_{\alpha\beta}^+) = T_{\alpha\beta}\, X(t_{\alpha\beta}^+) \tag{4.8}$$

$$\dot{Y}(t_{\alpha\beta}^+) = T_{\alpha\beta}\, \dot{X}(t_{\alpha\beta}^+) \tag{4.9}$$

where $I_{\alpha\to\beta}$ is the N-dimensional impulse of the generalized forces and $T_{\alpha\beta}$ is a constant $(N-1)\times N$ transformation matrix. Equations (4.6) and (4.7) enable us to determine the states of the unconstrained system, X and $\dot{X}$, immediately after application of the constraint and Eqs.(4.8) and (4.9) determine the initial conditions for the constrained system. The number of unknowns in the vector $I_{\alpha\to\beta}$ is equal to the number of constraints and equal to the number of dependent variables in the vector $\dot{X}(t_{\alpha\beta}^+)$, which is one in the present discussion, and therefore Eq.(4.7) can be solved without any problem. Since the set of independent variables in the vector $\dot{X}(t_{\alpha\beta}^+)$ is not unique, the transformation matrix $T_{\alpha\beta}$ is not unique. This will be illustrated with an example later.

The transition from state β to state α occurs over a brief interval of time when the constraint is removed. If $[t_{\beta\alpha}^-, t_{\beta\alpha}^+]$ denotes this transition interval, the effect of

the transition can be described by the relations

$$Y(t^+_{\beta\alpha}) = Y(t^-_{\beta\alpha}) \tag{4.10}$$

$$\dot{Y}(t^+_{\beta\alpha}) = \dot{Y}(t^-_{\beta\alpha}) \tag{4.11}$$

and

$$X(t^+_{\beta\alpha}) = T_{\beta\alpha}\, Y(t^+_{\beta\alpha}) \tag{4.12}$$

$$\dot{X}(t^+_{\beta\alpha}) = T_{\beta\alpha}\, \dot{Y}(t^+_{\beta\alpha}) \tag{4.13}$$

where $T_{\beta\alpha}$ is a constant and unique $N \times (N-1)$ transformation matrix. The transitions from state α to state β and from state β to state α are summarized in Fig.4.4. To obtain a relationship between the mass and stiffness matrices in Eqs.(4.4) and

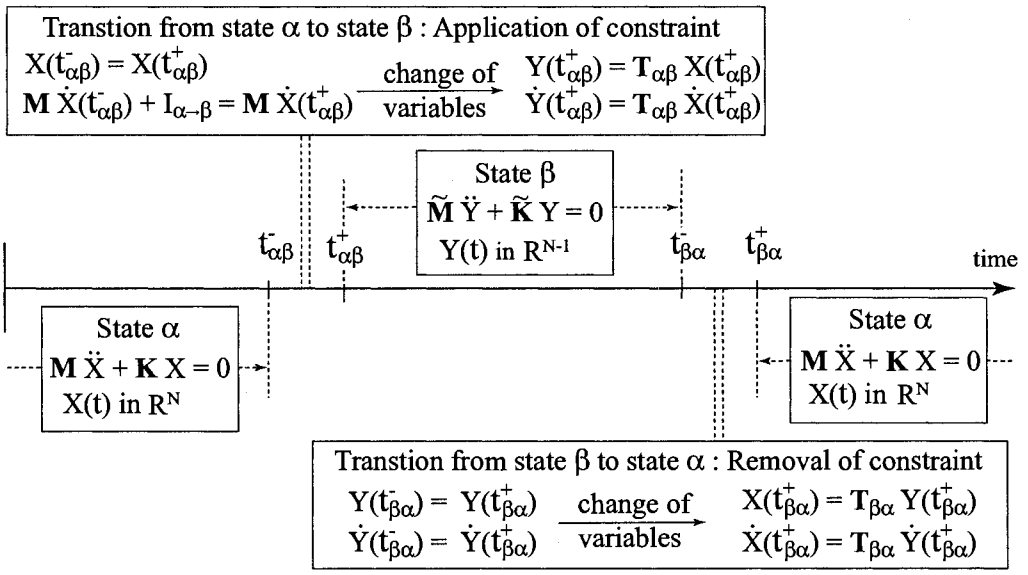

Figure 4.4. System description before and after application and removal of constraint

(4.5), we note that the kinetic energy before and after removal of the constraint is the same. Using Eqs.(4.11) and (4.13) we can show that

$$\begin{aligned} \frac{1}{2}\dot{Y}^T(t^-_{\beta\alpha})\tilde{M}\dot{Y}(t^-_{\beta\alpha}) &= \frac{1}{2}\dot{X}^T(t^+_{\beta\alpha})M\dot{X}(t^+_{\beta\alpha}) \\ \Rightarrow \quad \frac{1}{2}\dot{Y}^T(t^+_{\beta\alpha})\tilde{M}\dot{Y}(t^+_{\beta\alpha}) &= \frac{1}{2}\dot{Y}^T(t^+_{\beta\alpha})T^T_{\beta\alpha}MT_{\beta\alpha}\dot{Y}(t^+_{\beta\alpha}) \end{aligned} \tag{4.14}$$

Since the above equation holds for any $\dot{Y}(t^+_{\beta\alpha})$, it follows that

$$\tilde{M} = T^T_{\beta\alpha}MT_{\beta\alpha} \tag{4.15}$$

The strain energy immediately before and after removal of the constraint is also the same. Using Eqs.(4.10) and (4.12) we can therefore show that

$$\begin{aligned} \frac{1}{2}Y^T(t^-_{\beta\alpha})\tilde{K}Y(t^-_{\beta\alpha}) &= \frac{1}{2}X^T(t^+_{\beta\alpha})KX(t^+_{\beta\alpha}) \\ \Rightarrow \quad \frac{1}{2}Y^T(t^+_{\beta\alpha})\tilde{K}Y(t^+_{\beta\alpha}) &= \frac{1}{2}Y^T(t^+_{\beta\alpha})T^T_{\beta\alpha}KT_{\beta\alpha}Y(t^+_{\beta\alpha}) \end{aligned} \tag{4.16}$$

Once again, since the above equation holds for any $Y(t^+_{\beta\alpha})$, we can claim that

$$\tilde{K} = T^T_{\beta\alpha}KT_{\beta\alpha} \tag{4.17}$$

Equations (4.15) and (4.17) provide expressions for $\tilde{M}$ and $\tilde{K}$ in terms of M and K, respectively, but the reverse transformations are not possible. The kinetic energy before and after application of the constraint is not the same and it is not possible to start from an expression similar to Eq.(4.14). The strain energy before and after application of the constraint is the same and it is possible to start with an expression similar to Eq.(4.16) and use Eq.(4.8) to obtain

$$\begin{aligned} \frac{1}{2}X^T(t^-_{\alpha\beta})KX(t^-_{\alpha\beta}) &= \frac{1}{2}Y^T(t^+_{\alpha\beta})\tilde{K}Y(t^+_{\alpha\beta}) \\ \Rightarrow \quad \frac{1}{2}X^T(t^+_{\alpha\beta})KX(t^+_{\alpha\beta}) &= \frac{1}{2}X^T(t^+_{\alpha\beta})T^T_{\alpha\beta}\tilde{K}T_{\alpha\beta}X(t^+_{\alpha\beta}) \end{aligned}$$

The above equation is not valid for all values of $X(t^+_{\alpha\beta})$ since the constraint can be applied only when the configuration of the system satisfies the constraint instantaneously. Therefore, we cannot claim $K = T^T_{\alpha\beta}\tilde{K}T_{\alpha\beta}$.

4.4.2 Energetics of constraint application and removal

The change in kinetic energy over one cycle of constraint application and removal is given by the relation

$$\Delta E = \frac{1}{2}\dot{X}^T(t^+_{\alpha\beta})\, M\, \dot{X}(t^+_{\alpha\beta}) - \frac{1}{2}\dot{X}^T(t^-_{\alpha\beta})\, M\, \dot{X}(t^-_{\alpha\beta}) \tag{4.18}$$

To simplify Eq.(4.18), we premultiply Eq.(4.7) by $\dot{X}^T(t^+_{\alpha\beta})$ and $\dot{X}^T(t^-_{\alpha\beta})$ to obtain

$$\dot{X}^T(t^+_{\alpha\beta})M\dot{X}(t^+_{\alpha\beta}) = \dot{X}^T(t^+_{\alpha\beta})M\dot{X}(t^-_{\alpha\beta}) + \dot{X}^T(t^+_{\alpha\beta})I_{\alpha\to\beta} \tag{4.19}$$

$$\dot{X}^T(t^-_{\alpha\beta})M\dot{X}(t^+_{\alpha\beta}) = \dot{X}^T(t^-_{\alpha\beta})M\dot{X}(t^-_{\alpha\beta}) + \dot{X}^T(t^-_{\alpha\beta})I_{\alpha\to\beta} \tag{4.20}$$

Assuming a workless constraint, we can claim that

$$\dot{X}^T(t^+_{\alpha\beta})I_{\alpha\to\beta} = 0 \tag{4.21}$$

Using the symmetric property of the mass matrix, we can then show from Eqs.(4.19) and (4.20) that

$$\begin{aligned}\dot{X}^T(t^+_{\alpha\beta})M\dot{X}(t^+_{\alpha\beta}) &= \dot{X}^T(t^+_{\alpha\beta})M\dot{X}(t^-_{\alpha\beta}) \\ &= \dot{X}^T(t^-_{\alpha\beta})M\dot{X}(t^+_{\alpha\beta}) \\ &= \dot{X}^T(t^-_{\alpha\beta})M\dot{X}(t^-_{\alpha\beta}) + \dot{X}^T(t^-_{\alpha\beta})I_{\alpha\to\beta}\end{aligned} \tag{4.22}$$

Substitution of Eqs.(4.21) and (4.22) into Eq.(4.18) gives

$$\Delta E = \frac{1}{2}\dot{X}^T(t^-_{\alpha\beta})I_{\alpha\to\beta} \tag{4.23}$$

To simplify further, we rewrite Eq.(4.7) as

$$\dot{X}(t^-_{\alpha\beta}) = \dot{X}(t^+_{\alpha\beta}) - M^{-1}I_{\alpha\to\beta} \tag{4.24}$$

The expression for $\dot{X}(t^-_{\alpha\beta})$ in Eq.(4.24) is substituted in Eq.(4.23) to obtain

$$\begin{aligned} \Delta E &= \frac{1}{2}\left(\dot{X}^T(t^+_{\alpha\beta})I_{\alpha\to\beta} - I^T_{\alpha\to\beta}M^{-T}I_{\alpha\to\beta}\right) \\ &= -\frac{1}{2}I^T_{\alpha\to\beta}M^{-1}I_{\alpha\to\beta} \end{aligned} \tag{4.25}$$

In simplifying Eq.(4.25) we used the relation $\dot{X}^T(t^+_{\alpha\beta})I_{\alpha\to\beta} = 0$ and the symmetry of the mass matrix. The mass matrix is positive definite and thus $\Delta E \leq 0$.

4.4.3 Modal coordinate description

Let ϕ_i and $\mu_i(t)$, $i = 1, 2, \cdots N$, denote the linearly independent mode shapes and the corresponding modal amplitudes in state α. Similarly, let ψ_i and $\nu_i(t)$, $i = 1, 2, \cdots (N-1)$, denote the linearly independent mode shapes and the corresponding modal amplitudes in state β. The mode shapes in state α, ϕ_i, are N-dimensional whereas the mode shapes in state β, ψ_i, are $(N-1)$-dimensional. For convenience, we embed the $(N-1)$-dimensional mode shapes of state β, ψ_i, into N dimensions using the transformation matrix in Eq.(4.12), namely,

$$\tilde{\psi}_i = T_{\beta\alpha}\psi_i, \qquad i = 1, 2, \cdots, (N-1) \tag{4.26}$$

The generalized coordinates, before and after application of the constraint, can now be expressed as follows

$$X(t) = \begin{cases} \sum_{i=1}^{N} \mu_i(t)\,\phi_i = \Phi\,\mu(t) & t \le t_{\alpha\beta}^{-} \\ \\ \sum_{i=1}^{N-1} \nu_i(t)\,\tilde{\psi}_i = \tilde{\Psi}\,\nu(t) & t \ge t_{\alpha\beta}^{+} \end{cases} \tag{4.27}$$

where $\Phi = [\phi_1, \phi_2, \cdots, \phi_N] \in R^{N\times N}$ and $\tilde{\Psi} = \left[\tilde{\psi}_1, \tilde{\psi}_2, \cdots, \tilde{\psi}_{(N-1)}\right] \in R^{N\times(N-1)}$ are modal matrices in states α and β, respectively, and $\mu = [\mu_1, \mu_2, \cdots, \mu_N]^T$ and $\nu = \left[\nu_1, \nu_2, \cdots, \nu_{(N-1)}\right]^T$. The transition from state α to state β, described earlier by Eqs.(4.6) and (4.7), can now be written as

$$\sum_{i=1}^{N-1} \nu_i(t_{\alpha\beta}^{+})\,\tilde{\psi}_i = \sum_{i=1}^{N} \mu_i(t_{\alpha\beta}^{-})\,\phi_i \tag{4.28}$$

$$M\sum_{i=1}^{N-1} \dot{\nu}_i(t_{\alpha\beta}^{+})\,\tilde{\psi}_i = M\sum_{i=1}^{N} \dot{\mu}_i(t_{\alpha\beta}^{-})\,\phi_i + I_{\alpha\to\beta} \tag{4.29}$$

From the orthogonality property of the modes we have

$$\psi^T \tilde{M} \psi = I_{(N-1)}$$

where $I_{(N-1)}$ is the $(N-1)$-dimensional identity matrix. Substituting Eqs.(4.15) and (4.26) in the above equation we can show that

$$\tilde{\psi}^T M \tilde{\psi} = I_{(N-1)} \tag{4.30}$$

Using Eq.(4.30) and the identity $\tilde{\psi}_j^T\, I_{\alpha\beta} = 0$, which follows from Eq.(4.21), we can obtain the modal displacements and velocities of the constrained system in terms of those of the unconstrained system from Eqs.(4.28) and (4.29), as follows

$$\nu_j(t_{\alpha\beta}^{+}) = \sum_{i=1}^{N} \tilde{\psi}_j^T\, M\, \phi_i\, \mu_i(t_{\alpha\beta}^{-}) \tag{4.31}$$

$$\dot{\nu}_j(t_{\alpha\beta}^{+}) = \sum_{i=1}^{N} \tilde{\psi}_j^T\, M\, \phi_i\, \dot{\mu}_i(t_{\alpha\beta}^{-}) \tag{4.32}$$

In matrix form, Eqs.(4.31) and (4.32) can be written as

$$\begin{aligned} \nu(t^+_{\alpha\beta}) &= \Gamma\,\mu(t^-_{\alpha\beta}) \\ \dot{\nu}(t^+_{\alpha\beta}) &= \Gamma\,\dot{\mu}(t^-_{\alpha\beta}) \end{aligned} \tag{4.33}$$

where

$$\Gamma \doteq \tilde{\Psi}^T M \Phi \tag{4.34}$$

Repeating the above procedure for the transition from state β to state α, we can similarly show that

$$\begin{aligned} \mu(t^+_{\beta\alpha}) &= \Gamma^T\,\nu(t^-_{\beta\alpha}) \\ \dot{\mu}(t^+_{\beta\alpha}) &= \Gamma^T\,\dot{\nu}(t^-_{\beta\alpha}) \end{aligned} \tag{4.35}$$

The change in kinetic energy over one cycle of constraint application and removal can now be expressed in terms of the modal coordinates. Starting from Eq.(4.23) and using Eqs.(4.24), (4.27), and (4.33), we obtain

$$\begin{aligned} \Delta E &= \tfrac{1}{2}\dot{X}^T(t^-_{\alpha\beta})M\left[\dot{X}(t^+_{\alpha\beta}) - \dot{X}(t^-_{\alpha\beta})\right] \\ &= \tfrac{1}{2}\dot{\mu}^T(t^-_{\alpha\beta})\Phi^T M\left[\tilde{\Psi}\dot{\nu}(t^+_{\alpha\beta}) - \Phi\dot{\mu}(t^-_{\alpha\beta})\right] \\ &= \tfrac{1}{2}\dot{\mu}^T(t^-_{\alpha\beta})\Phi^T M\left[\tilde{\Psi}\Gamma - \Phi\right]\dot{\mu}(t^-_{\alpha\beta}) \\ &= -\tfrac{1}{2}\dot{\mu}^T(t^-_{\alpha\beta})\Lambda\dot{\mu}(t^-_{\alpha\beta}) \end{aligned} \tag{4.36}$$

where

$$\Lambda \doteq \left(I_N - \Gamma^T\Gamma\right) \tag{4.37}$$

and I_N is the N-dimensional identity matrix. In the next section we show that Λ is positive semi-definite and this will corroborate the observation made earlier from Eq.(4.25), namely, that $\Delta E \leq 0$.

We conclude this section by deriving expressions in modal coordinates that are equivalent to Eqs.(4.15) and (4.17). Since the kinetic energy before and after removal

of the constraint is the same, we can use Eq.(4.35) to show that

$$\frac{1}{2}\dot{\nu}^T(t^-_{\beta\alpha})\dot{\nu}(t^-_{\beta\alpha}) = \frac{1}{2}\dot{\mu}^T(t^+_{\beta\alpha})\dot{\mu}(t^+_{\beta\alpha}) = \frac{1}{2}\dot{\nu}^T(t^-_{\beta\alpha})\Gamma\Gamma^T\dot{\nu}(t^-_{\beta\alpha})$$

Since the above equation holds good for all $\dot{\nu}(t^-_{\beta\alpha})$, we claim that

$$\Gamma\Gamma^T = I_{(N-1)} \tag{4.38}$$

Let ω_i, $i = 1, 2, \cdots, N$, and $\tilde{\omega}_j$, $j = 1, 2, \cdots, (N-1)$, denote the natural frequencies of the unconstrained and constrained systems, respectively. The stiffness matrices in modal coordinates can then be defined as follows:

$$\begin{aligned} \Omega &\doteq diag\left[\omega_1^2, \omega_2^2, \cdots, \omega_N^2\right] \\ \tilde{\Omega} &\doteq diag\left[\tilde{\omega}_1^2, \tilde{\omega}_2^2, \cdots, \tilde{\omega}_{(N-1)}^2\right] \end{aligned} \tag{4.39}$$

Since the strain energy before and after removal of the constraint is the same, we can use Eq.(4.35) to show that

$$\frac{1}{2}\nu^T(t^-_{\beta\alpha})\tilde{\Omega}\nu(t^-_{\beta\alpha}) = \frac{1}{2}\mu^T(t^+_{\beta\alpha})\Omega\mu(t^+_{\beta\alpha}) = \nu^T(t^-_{\beta\alpha})\Gamma\Omega\Gamma^T\nu(t^-_{\beta\alpha})$$

Since the above equation holds for all $\nu(t^-_{\beta\alpha})$, we claim that

$$\tilde{\Omega} = \Gamma\Omega\Gamma^T \tag{4.40}$$

4.4.4 Numerical example

We consider a system with three dof in state α and two dof in state β, *i.e.* $N = 3$. The system, shown in Fig.4.5 consists of four bars connected by rotational springs except for the two middle bars, which are connected by a frictionless pin joint. In state α, the pin joint is free and the generalized coordinates are chosen to be the

displacements of the ends of the bars, namely, x_1, x_2, x_3. The pin joint is locked only when the middle two bars are aligned, and locking the joint applies the constraint

$$f(X) = 3x_1 - 4x_2 + x_3 = 0 \tag{4.41}$$

and transfers the system to state β. In state β, the generalized coordinates are the displacements y_1, y_2. The relationship between the generalized coordinates of states α and β can be derived from Fig.4.5 as follows:

$$\begin{aligned} y_1 &= x_1 + \lambda_1(3x_1 - 4x_2 + x_3) \\ y_2 &= x_3 + \lambda_2(3x_1 - 4x_2 + x_3) \end{aligned} \quad \Rightarrow \quad T_{\alpha\beta} = \begin{bmatrix} 1+3\lambda_1 & -4\lambda_1 & \lambda_1 \\ 3\lambda_2 & -4\lambda_2 & 1+\lambda_2 \end{bmatrix}$$

$$\begin{aligned} x_1 &= y_1 \\ x_2 &= 0.75y_1 + 0.25y_2 \\ x_3 &= y_2 \end{aligned} \quad \Rightarrow \quad T_{\beta\alpha} = \begin{bmatrix} 1 & 0 \\ 0.75 & 0.25 \\ 0 & 1 \end{bmatrix}$$

where λ_1 and λ_2 are arbitrary non-zero constants. Clearly, $T_{\beta\alpha}$ is unique whereas $T_{\alpha\beta}$ is not. For small displacements, the system behaves linearly and Eqs.(4.4) and

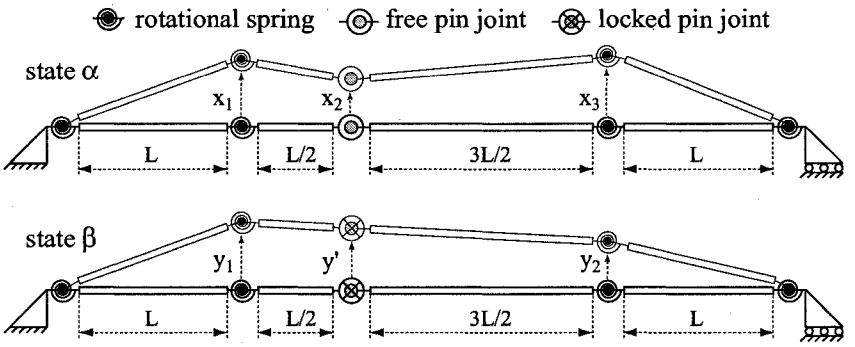

Figure 4.5. A linear system with three dof in state α and two dof in state β

(4.5) describe its dynamics in states α and β, respectively. The mass and stiffness matrices in Eqs.(4.4) and (4.5) can be derived from the system Lagrangian [39] as

$$M = \frac{\rho AL}{12}\begin{bmatrix} 6 & 1 & 0 \\ 1 & 8 & 3 \\ 0 & 3 & 10 \end{bmatrix} \qquad K = \frac{k}{9L^2}\begin{bmatrix} 90 & -54 & 0 \\ -54 & 40 & -10 \\ 0 & -10 & 34 \end{bmatrix}$$

$$\tilde{M} = \frac{\rho AL}{3}\begin{bmatrix} 3 & 1 \\ 1 & 3 \end{bmatrix} \qquad \tilde{K} = \frac{k}{2L^2}\begin{bmatrix} 7 & -3 \\ -3 & 7 \end{bmatrix}$$

where ρ is the material density and A is the cross-sectional area of the bars, k is the stiffness of the rotational springs, and L is a dimension that is shown in Fig.4.5.

The transformation from state α to state β requires the application of an action-reaction pair of impulsive moments[3], $\tau(t)$, on the middle bars, as shown in Fig.4.6. If the impulse of these moments is denoted by

$$C = \int_{t_{\alpha\beta}^-}^{t_{\alpha\beta}^+} \tau(t)\, dt,$$

the impulse vector corresponding to the generalized coordinates $X = [x_1, x_2, x_3]$ can be shown to be (see Appendix-A)

$$I_{\alpha\to\beta} = \frac{C}{L}\begin{bmatrix} 2 & -8/3 & 2/3 \end{bmatrix}^T \tag{4.42}$$

Starting from Eq.(4.25), the change in kinetic energy over one cycle of constraint

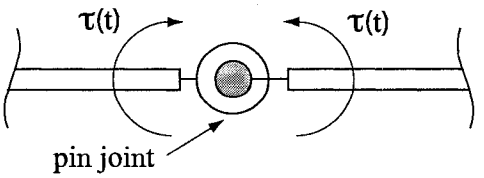

Figure 4.6. Action-reaction pair of impulsive moments

[3]Such impulsive moments can be generated in experiments by an electromagnetic brake, as in [40].

application and removal can now be shown to be (see Appendix-B)

$$\begin{aligned}
\Delta E &= -\frac{1}{2} I^T_{\alpha\to\beta} M^{-1} I_{\alpha\to\beta} \\
&= -\frac{13}{1536}\rho AL\left[3\dot{x}_1(t^-_{\alpha\beta}) - 4\dot{x}_2(t^-_{\alpha\beta}) + \dot{x}_3(t^-_{\alpha\beta})\right]^2 \\
&= -\frac{13}{1536}\rho AL\left\{f[\dot{X}(t^-_{\alpha\beta})]\right\}^2 \leq 0
\end{aligned}$$

where the function $f(.)$ is defined by Eq.(4.41).

For the purpose of simulation, we assumed the bars to be of circular cross section and made of aluminum. The material and geometric properties of the bars and the stiffness of the rotational springs were assumed to be

$$\rho = 2710 \text{ Kg/m}^3, \quad A = \pi(0.02)^2 \text{ m}^2, \quad L = 0.20 \text{ m}, \quad k = 20.0 \text{ Nm} \tag{4.43}$$

The system was assumed to be in state α at the initial time with the following initial conditions

$$(x_1, x_2, x_3, \dot{x}_1, \dot{x}_2, \dot{x}_3) = (0.006, 0.003, -0.003, 0.00, 0.00, 0.00)$$

in SI units. The system was switched from state α to state β at the earliest opportunity after 0.2 seconds when the two middle bars are aligned ($f(X) = 0$) and switched back to state α after 0.2 seconds in state β. The process was continued till the energy of the system became negligible. Figure 4.7 shows the displacements of the bars and the energy of the system as a function of time. The energy undergoes a step change when the system changes state from α to β due to application of the constraint. It remains constant at all other times.

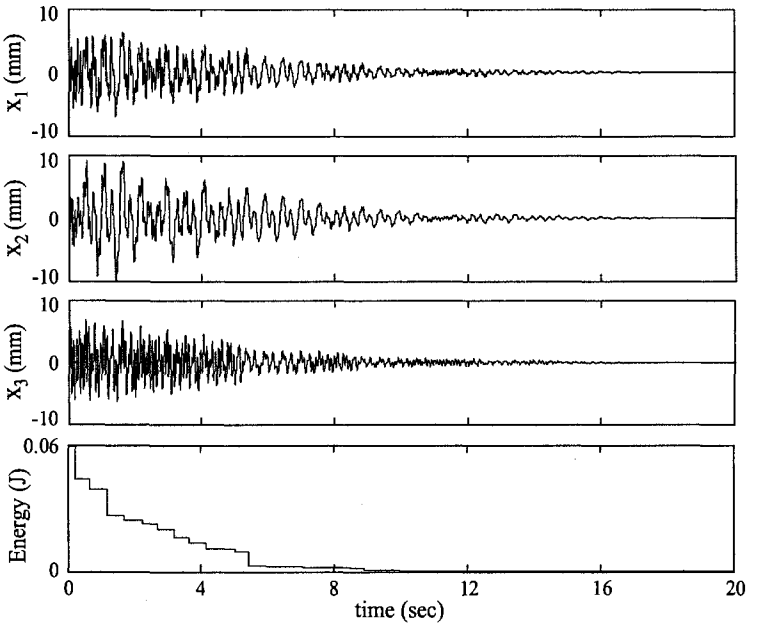

Figure 4.7. Plot of displacements of the bars and total energy of the system

4.5 Controllability Issues for Linear Systems

4.5.1 Limitation of energy dissipation

We investigate the properties of the matrix Λ, defined in Eq.(4.37), to understand the limitations of energy dissipation through application of constraints. Consider the matrix $\Gamma^T\Gamma$, where Γ is defined by Eq.(4.34). Using Eq.(4.38) it can be shown that

$$\left(\Gamma^T\Gamma\right)^2 = \Gamma^T\Gamma\Gamma^T\Gamma = \Gamma^T\Gamma \tag{4.44}$$

This implies $\Gamma^T\Gamma$ is idempotent and hence $\Lambda = \left(I_N - \Gamma^T\Gamma\right)$ is idempotent. The trace of Λ can be computed as

$$\begin{aligned} \text{trace}[\Lambda] &= \text{trace}[I_N] - \text{trace}[\Gamma^T\Gamma] \\ &= N - \text{trace}[\Gamma\Gamma^T] \\ &= N - \text{trace}[I_{(N-1)}] \\ &= 1 \end{aligned} \tag{4.45}$$

Since the eigenvalues of idempotent matrices are all zero or unity, the trace of an idempotent matrix is equal to its rank. From Eq.(4.45) we deduce that Λ has one unit eigenvalue and other eigenvalues are all zero. If v is the normalized eigenvector of Λ corresponding to its unit eigenvalue, then eigen decomposition of Λ gives

$$\Lambda = vv^T \tag{4.46}$$

Substitution of Eq.(4.46) into Eq.(4.36) gives

$$\Delta E = -\frac{1}{2}\dot{\mu}^T(t_{\alpha\beta}^-)vv^T\dot{\mu}(t_{\alpha\beta}^-) = -\frac{1}{2}\left[v^T\dot{\mu}(t_{\alpha\beta}^-)\right]^2 \leq 0 \tag{4.47}$$

Clearly, the energy of the system will not be dissipated upon application of the constraint if any of the following conditions hold:

1. $\dot{\mu}(t_{\alpha\beta}^-) = 0$: the constraint is applied when the system has zero kinetic energy.
2. $v^T\dot{\mu}(t_{\alpha\beta}^-) = 0$, $v_i \neq 0$, $i = 1, 2, \cdots, N$: the constraint is applied when the modal velocity vector is normal to the eigenvector of Λ corresponding to the unity eigenvalue.
3. $v_i = 0$, $i \in S_r \doteq \{k_1, k_2, \cdots, k_r\}$, $\dot{\mu}_j(t_{\alpha\beta}^-) = 0$, $\forall j \notin S_r$: the kinetic energy of the system lies in specific modes that correspond to zero entries of v.

The first and second conditions can be avoided through a proper choice of the time when the constraint is applied. It may not be possible to avoid the third condition, which depends on modal characteristics of the unconstrained and constrained systems and the energy distribution of the unconstrained system. This corresponds to a necessary condition for energy entrapment.

4.5.2 Energy entrapment

In this section we show that energy can get trapped in specific modes of the system. The third condition in Section 4.5.1 is a necessary condition for energy entrapment

but not a sufficient condition. Before we present the sufficient condition, we derive some properties of the matrix Γ, defined by Eq.(4.34). We assume that Γ has the form

$$\Gamma = \left[\begin{array}{cccc} p_1 & p_2 & \cdots & p_N \end{array} \right], \quad \Gamma^T = \left[\begin{array}{cccc} q_1 & q_2 & \cdots & q_{(N-1)} \end{array} \right] \tag{4.48}$$

where the p's and q's are column vectors of dimension $(N-1)$ and N, respectively. Using the identity $\Gamma\Gamma^T = I_{(N-1)}$ from Eq.(4.38), we can show that

$$q_i^T q_j = \left\{ \begin{array}{ll} 1 & j = i \\ 0 & j \neq i \end{array} \right. , \quad i, j = 1, 2, \cdots, (N-1) \tag{4.49}$$

Since v is the eigenvector of Λ corresponding to its unit eigenvalue, v is also the eigenvector of $\Gamma^T\Gamma$ corresponding to its zero eigenvalue. This implies that

$$\Gamma^T\Gamma v = 0 \quad \Rightarrow \quad v^T\Gamma^T\Gamma v = 0 \quad \Rightarrow \quad \Gamma v = 0 \quad \Rightarrow \quad v \perp q_j \quad j = 1, 2, \cdots, (N-1)$$

Since $\Gamma^T\Gamma$ has $(N-1)$ repeated eigenvalues, there will be no unique set of orthonormal eigenvectors. The q_j's, $j = 1, 2, \cdots, (N-1)$ are in the space spanned by the eigenvectors of $\Gamma^T\Gamma$ with eigenvalue of unity. This follows directly from the relation

$$\left(\Gamma^T\Gamma\right)\Gamma^T = \Gamma^T$$

which follows from the identity $\Gamma\Gamma^T = I_{(N-1)}$ in Eq.(4.38). Now consider the orthonormal matrix

$$Q = \left[\begin{array}{ccccc} q_1 & q_2 & \cdots & q_{(N-1)} & v \end{array} \right] = \left[\begin{array}{cc} p_1^T & v_1 \\ \vdots & \vdots \\ p_N^T & v_N \end{array} \right]$$

Since $\left[QQ^T\right]_{j,j} = p_j^T p_j + v_j^2$, we can readily establish

$$p_j^T p_j = 1.0 - v_j^2 \leq 1.0, \quad i,j = 1,2,\cdots,N \tag{4.50}$$

The sufficient condition for energy entrapment is stated next with the help of the following theorem.

Theorem 4.1 *The energy of a linear system will remain trapped in r specific modes if* Γ *contains an orthonormal sub-matrix of dimension r.* □

Proof: We renumber the modes of both the unconstrained and constrained systems such that Γ has the form

$$\Gamma = \begin{bmatrix} A_{11} & A_{12} \\ A_{21} & A_{22} \end{bmatrix}$$

where A_{22} is the orthonormal sub-matrix of dimension r. From Eqs.(4.49) and (4.50) we know that the p's and q's have norm less than or equal to unity. This implies that $A_{12} = A_{21} = 0$ and hence

$$\Gamma = \begin{bmatrix} A_{11} & 0 \\ 0 & A_{22} \end{bmatrix} \tag{4.51}$$

We partition the modal coordinates of state α and state β as follows:

$$\mu = \begin{bmatrix} \mu_1 & \mu_2 \end{bmatrix}, \quad \nu = \begin{bmatrix} \nu_1 & \nu_2 \end{bmatrix}, \quad \mu_2, \nu_2 \in R^r \tag{4.52}$$

Equations (4.33) and (4.35) can now be rewritten as

$$\begin{aligned} \nu_2(t_{\alpha\beta}^+) &= A_{22}\,\mu_2(t_{\alpha\beta}^-) \\ \dot{\nu}_2(t_{\alpha\beta}^+) &= A_{22}\,\dot{\mu}_2(t_{\alpha\beta}^-) \end{aligned} \tag{4.53}$$

$$\begin{aligned} \mu_2(t_{\beta\alpha}^+) &= A_{22}^T\,\nu_2(t_{\beta\alpha}^-) \\ \dot{\mu}_2(t_{\beta\alpha}^+) &= A_{22}^T\,\dot{\nu}_2(t_{\beta\alpha}^-) \end{aligned} \tag{4.54}$$

If $\tilde{\Omega}_{22}$ and Ω_{22} denote the lower right $r \times r$ sub-matrices of $\tilde{\Omega}$ and Ω, respectively, then substitution of Eq.(4.51) into Eq.(4.40) gives

$$\tilde{\Omega}_{22} = A_{22}\Omega_{22}A_{22}^T \tag{4.55}$$

Using the orthonormal property of A_{22} it can be easily shown that

$$\Omega_{22} = A_{22}^T\tilde{\Omega}_{22}A_{22} \tag{4.56}$$

In state α, the total energy associated with modes μ_2 prior to application of the constraint is

$$E_2(t_{\alpha\beta}^-) = \frac{1}{2}\dot{\mu}_2^T(t_{\alpha\beta}^-)\dot{\mu}_2(t_{\alpha\beta}^-) + \frac{1}{2}\mu_2^T(t_{\alpha\beta}^-)\Omega_{22}\mu_2(t_{\alpha\beta}^-)$$

Using Eqs.(4.53) and (4.55), this can be shown to be equal to

$$\begin{aligned} E_2(t_{\alpha\beta}^-) &= \frac{1}{2}\dot{\nu}_2^T(t_{\alpha\beta}^+)A_{22}A_{22}^T\dot{\nu}_2(t_{\alpha\beta}^+) + \frac{1}{2}\nu_2^T(t_{\alpha\beta}^+)A_{22}\Omega_{22}A_{22}^T\nu_2(t_{\alpha\beta}^+) \\ &= \frac{1}{2}\dot{\nu}_2^T(t_{\alpha\beta}^+)\dot{\nu}_2(t_{\alpha\beta}^+) + \frac{1}{2}\nu_2^T(t_{\alpha\beta}^+)\tilde{\Omega}_{22}\nu_2(t_{\alpha\beta}^+) \\ &= E_2(t_{\alpha\beta}^+) \end{aligned} \tag{4.57}$$

In state β, the energy associated with modes ν_2 prior to removal of the constraint is

$$E_2(t_{\beta\alpha}^-) = \frac{1}{2}\dot{\nu}_2^T(t_{\beta\alpha}^-)\dot{\nu}_2(t_{\beta\alpha}^-) + \frac{1}{2}\nu_2^T(t_{\beta\alpha}^-)\tilde{\Omega}_{22}\nu_2(t_{\beta\alpha}^-)$$

Using Eqs.(4.54) and (4.56), this can be shown to be equal to

$$\begin{aligned} E_2(t_{\beta\alpha}^-) &= \frac{1}{2}\dot{\mu}_2^T(t_{\beta\alpha}^+)A_{22}^TA_{22}\dot{\mu}_2(t_{\beta\alpha}^+) + \frac{1}{2}\mu_2^T(t_{\beta\alpha}^+)A_{22}^T\tilde{\Omega}_{22}A_{22}\mu_2(t_{\beta\alpha}^+) \\ &= \frac{1}{2}\dot{\mu}_2^T(t_{\beta\alpha}^+)\dot{\mu}_2(t_{\beta\alpha}^+) + \frac{1}{2}\mu_2^T(t_{\beta\alpha}^+)\Omega_{22}\mu_2(t_{\beta\alpha}^+) \\ &= E_2(t_{\beta\alpha}^+) \end{aligned} \tag{4.58}$$

Equations (4.57) and (4.58) imply that energy is trapped between modes μ_2 in state α and modes ν_2 in state β, and this completes the proof.

The results in Theorem 1 can be further extended as follows:

1. From Eq.(4.55) it can be shown that the eigenvalues of $\tilde{\Omega}_{22}$ are the same as those of Ω_{22}. Since $\tilde{\Omega}_{22}$ and Ω_{22} are both diagonal matrices, they must be identical. Equation (4.55) now implies $\Omega_{22} = A_{22}\Omega_{22}A_{22}^T \quad \Rightarrow \quad \Omega_{22}A_{22} = A_{22}\Omega_{22}$. Since Ω_{22} and A_{22} commute and Ω_{22} is diagonal with distinct entries, A_{22} must be diagonal [41]. Since A_{22} is orthonormal, it simply follows that $A_{22} = I_r$, where I_r is the identity matrix of dimension r. In summary, we have

$$\tilde{\Omega}_{22} = \Omega_{22}, \qquad A_{22} = I_r \tag{4.59}$$

   This implies that r modes in state α will be identical to r modes in state β. These modes form an invariant sub-space that is not affected by the constraint and energy in these modes remain trapped.

2. From Eq.(4.51) we can show that $\Gamma^T\Gamma$ and Λ will have the form

$$\Gamma^T\Gamma = \begin{bmatrix} A_{11}^T A_{11} & 0 \\ 0 & I_r \end{bmatrix}, \qquad \Lambda = \begin{bmatrix} I_{N-r} - A_{11}^T A_{11} & 0 \\ 0 & 0 \end{bmatrix}$$

   From the expression of Λ in Eq.(4.46) it follows that r elements of v will be zero. Clearly, the third condition in Section 4.5.1 is satisfied when the condition in Theorem 1 is satisfied.

4.5.3 Numerical example

Consider the system in Fig.4.5 with all bars having the same length L, as shown in Fig.4.8. Assuming the system parameters to be those given by Eq.(43), the matrices

Γ and Λ and the eigenvector v are computed as follows:

$$\Gamma^T = \begin{pmatrix} 0.9599 & 0.0 \\ 0.0 & 1.0 \\ -0.2804 & 0.0 \end{pmatrix}, \quad v = \begin{pmatrix} 0.2804 \\ 0.0 \\ 0.9599 \end{pmatrix},$$
$$\Lambda = \begin{pmatrix} 0.0786 & 0.0 & 0.2691 \\ 0.0 & 0.0 & 0.0 \\ 0.2691 & 0.0 & 0.9214 \end{pmatrix} \tag{4.60}$$

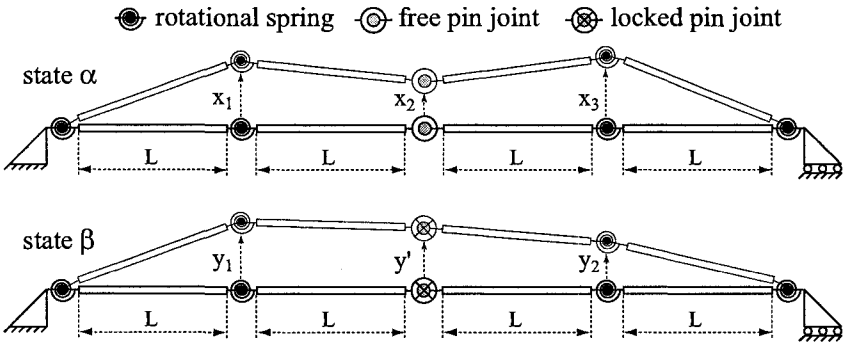

Figure 4.8. A modified version of the system in Fig.4.5 in states α and β

From the entries of Γ in Eq.(4.60) it is clear that the condition in Theorem 1 is satisfied with $r = 1$. Since $\Gamma^T_{2,2} = 1.0$, the energy of the system is trapped in the second mode of state α, which is also the second mode of state β. We can also verify that one element of v, namely v_2, is equal to zero. Energy entrapment can be verified from the simulation results presented in Fig.4.9, the initial conditions for which were chosen as

$$(x_1, x_2, x_3, \dot{x}_1, \dot{x}_2, \dot{x}_3) = (0.006, 0.016, 0.002, 0.00, 0.00, 0.00)$$

in SI units. As in the previous simulation, the system was switched from state α to state β at the earliest opportunity after 0.2 seconds when the two middle bars are

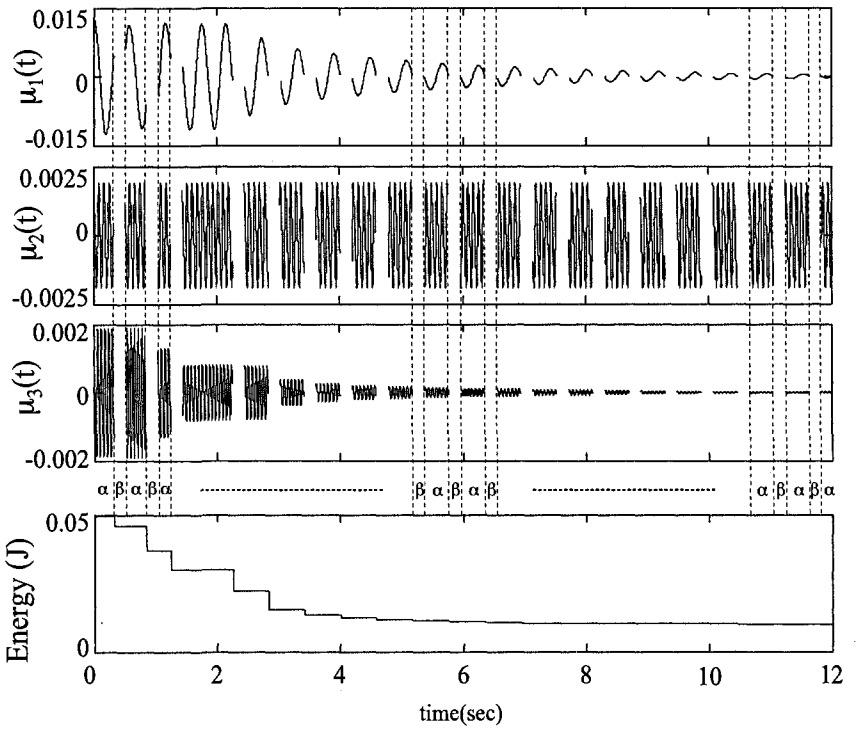

Figure 4.9. Plot of modal amplitudes in state α and total energy of the system

aligned, *i.e.*, when

$$g(X) = x_1 - 2x_2 + x_3 = 0$$

and switched back to state α after 0.2 seconds in state β. The modal amplitudes in state α, namely, μ_1, μ_2, μ_3, are shown in Fig.4.9 for the intervals of time when the system is in state α. It is clear from these plots that the amplitudes of the first and third modes decay to zero whereas the amplitude of the second mode remains constant. The plot of the energy confirms that some energy of the system gets trapped in the second mode.

4.6 Application to Nonlinear Systems

For the simulations in Sections 4.4 and 4.5, the constraints were applied when the two middle bars were aligned, *i.e.*, the constraints were applied based on state variable

information. The purpose of using state variable information was to make the analysis tractable by switching the unconstrained system to the same constrained system every time. Furthermore, the assumption of small displacements and linear system behavior permitted the analysis in modal coordinates. For nonlinear systems, where a modal coordinate description is not possible, the analysis does not benefit from switching based on state variable information. However, the information of the states can be used to maximize the amount of energy dissipated. We do not address this optimization problem in our work. Using a numerical example we simply show that a random switching schedule can be quite effective in dissipating the energy of a nonlinear system. This will demonstrate an important advantage of our approach that has not been explicitly stated thus far: that vibration control can be achieved without state variable estimation and therefore without the use of sensors.

The analysis for nonlinear systems can be carried out in a manner similar to that of linear systems presented in Section 4.4.1 and is therefore not repeated. It will be different in two respects: (a) the mass matrix will be a function of the generalized coordinates and not a constant matrix, and (b) the transformation matrices $T_{\alpha\beta}$ and $T_{\beta\alpha}$ will vary from one cycle of constraint application and removal to the next. This simply reflects the fact that the constraint applied and removed will be different for each cycle since a random switching schedule will be used.

We consider a serial chain of three links connected by revolute joints, as shown in Fig.4.10. Each joint has a rotational spring and the second joint can be locked or released for constraint application and removal. The unconstrained system has three dof and its configuration is described by the generalized coordinates α_1, α_2, α_3. The system is constrained by locking the second joint. In this locked configuration, which is described by the generalized coordinates β_1, β_2, the relative angle between the second joint and first joint is denoted by γ. The value of γ will be different for each cycle of constraint application and removal since a random switching schedule

will be used. The simulation results are presented in Fig.4.11. For this simulation,

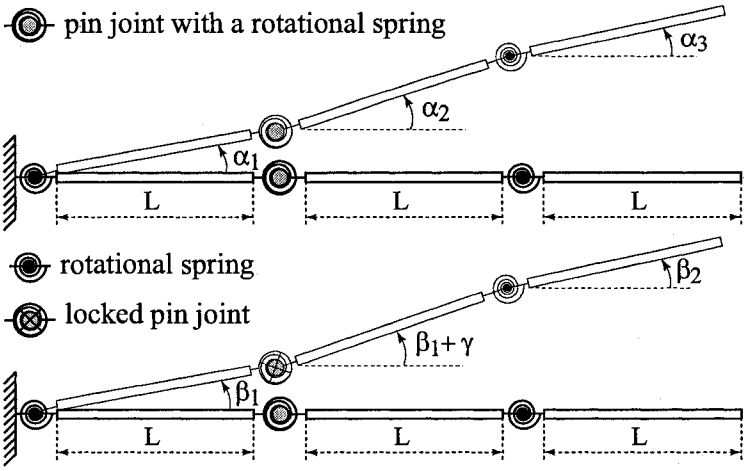

Figure 4.10. An example nonlinear system

the mass and length of each link were assumed to be 1.0 kg and 0.5 m, respectively. The stiffness of the rotational springs were assumed to be the same and equal to 200 Nm/rad. The initial conditions were assumed to be

$$(\theta_1, \theta_2, \theta_3, \dot{\theta}_1, \dot{\theta}_2, \dot{\theta}_3) = (15.0, -10.0, 5.0, 0.0, 0.0, 0.0)$$

where the units are in deg and deg/sec. The second joint was locked and released with the time interval between switchings randomly varying between 0.2 and 0.3 sec till the total energy of the system was dissipated. The simulation results indicate that a random switching schedule is quite effective in dissipating the total energy of the system.

4.7 Remarks

It has been shown that a sequence of application and removal of constraints can be used as a mechanism to extract energy of vibration from finite dimensional elastic systems. The strategy is straight forward, as it does not rely on state-dependent

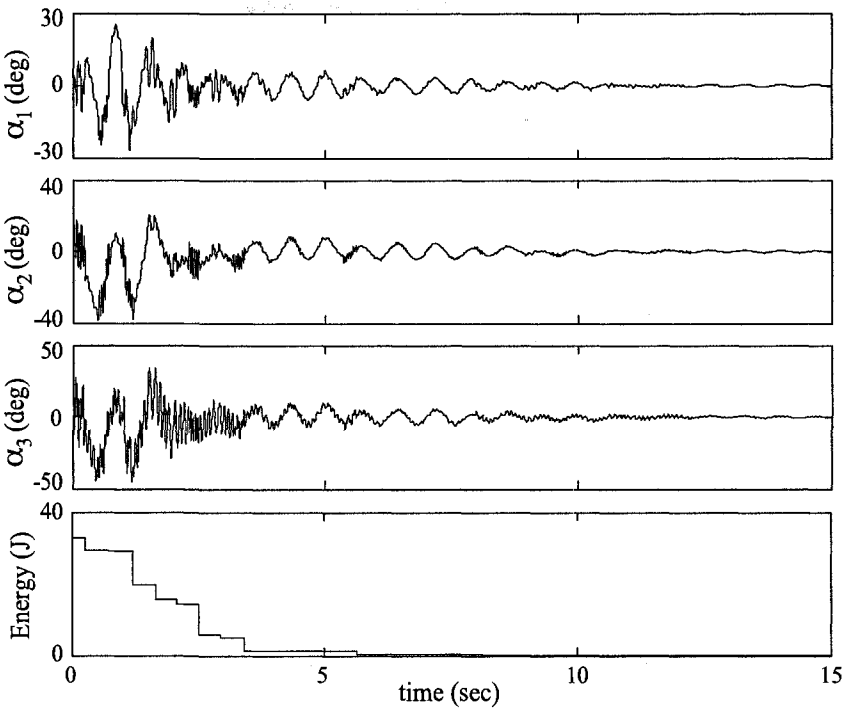

Figure 4.11. Plot of generalized coordinates and total energy of the nonlinear system

timing of the constraint application and thus it is easy to implement. This is particularly relevant in the case of non-linear systems, where examples show that here too application and removal of constraints leads to removal of kinetic energy. As such, the strategy emerges as a potential mechanism for vibration control without the use of sensors.

The results in this chapter highlight a number of interesting features of the behavior of linear systems under the repeated application and removal of constraints. In general, applying and removing constraints results in energy transfer from mode to mode and, in the case of finite-dof systems, removal from the system altogether in a manner akin to transferring energy to unmodeled, higher-order modes. In the process, energy is extracted from all modes except in cases where the modes and the constraints interact in such a way that energy is entrapped and a part of the system is indifferent to constraint application. One can view this as a sort of orthogonality of the system, as represented by a subset of its modes, and the constraints. This sug-

gests that if energy removal is the principal consideration, it may always be effected by applying and removing a different set of constraints after every switch, carefully crafted to affect all the modes of the system. A number of interesting further investigations are possible. For example, since the rate at which energy transfer takes place depends on and can be controlled by the manner in which the constraints are applied, it may be possible to optimize both the rate and the direction of this transfer to fit a particular purpose, simply by designing the constraint application scheme. Since the efficiency of a number of engineering systems relies on the manipulation of vibration energy, the work presented can have interesting applications in the design of such systems such as devices for vibration isolation, vibration control [1], [2], and energy harvesting. The goal of the next chapter is to use the method of energy dissipation proposed here but apply the constraints at specific times and locations to maximize energy removal.

CHAPTER 5

Energy Dissipation Through Optimal Application And Removal of Constraints

5.1 Introduction

The energy dissipation approach presented in the last chapter is revisited in this chapter with the objective of investigating efficient energy removal through an optimal sequence of constraint application. A special case of the constraint application procedure proposed in the last chapter is used here: the constraint is applied and instantaneously removed instead of remaining active for a finite duration of time. In terms of the nomenclature used in the last chapter, this implies $t^+_{\alpha\beta} = t^-_{\beta\alpha}$ and the system always remains in state α. The time spent in state β is zero. The basic idea is illustrated with the help of Fig.5.1, which is a modified version of the three dof[1] mass-spring system of Fig.4.1. Unlike in Fig.4.1, where a pin is inserted in the second mass to enforce the constraint $x_2 = 0$, here we assume that the second mass has an electromagnetic brake that enables it to stop instantaneously. Immediately after it stops, the brake is disabled and the mass is set free to move. In this case, the constraint $\dot{x}_2 = 0$ is enforced and instantaneously removed. The system configuration does not change and therefore its dof remain three, namely, x_1, x_2 and x_3. The application and instantaneous removal of the constraint however results

[1]degrees-of-freedom

in an instantaneous reduction in energy of the overall system by an amount equal to the kinetic energy of mass m_2. A repetition of the process of application and removal of the constraint will ultimately reduce the energy of the system to zero. In this chapter, we pose and solve several optimization problems to efficiently remove energy from the system by applying and instantaneously removing constraints at strategic location and specific instants of time.

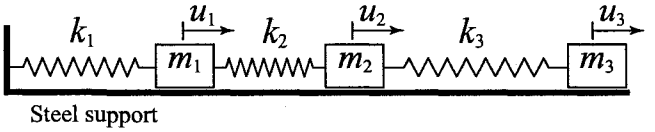

Figure 5.1. A three dof mass-spring system

The above idea of energy dissipation relies on application of an impulsive force on the system. It is however different from impact dampers, commonly used for vibration suppression, that also apply impulsive forces. For impact dampers, the motion of the impact mass is constrained to a specific region of the physical system, the impact mass moves in an uncontrolled fashion and the frequency of collisions depends on the dynamics of the overall system. In this work, we do not introduce impact masses but apply constraints that have the equivalent effect of an impact damper. This gives us the flexibility to control the timing as well as location of the impacts.

This chapter is organized as follows. In the next section we describe the effect of constraint application and removal and the loss of energy associated with this process. In section 5.3 we consider the examples of a discrete N-dof mass spring system and a continuous rectangular membrane fixed at all sides. For both examples, three optimization problems are solved using a genetic algorithm approach. A gradient-based optimization method is proposed in section 5.4 for solving optimization problems of the continuous rectangular membrane introduced in section 5.3. Concluding remarks are provided in section 5.5.

5.2 Energy Loss due to Constraint Application and Removal

In this section we investigate energy dissipation in linear systems with finite dof through application and instantaneous removal of constraints. From our earlier discussion we know that application of a constraint will result in an impact and transfer energy into the high-frequency modes of the system, where it will be dissipated naturally (without the use of active control). Our finite-dof assumption simply implies that the flexible modes are unmodeled; this is justified by the fact that the energy transferred to these modes decay rapidly and their high-frequency dynamics have negligible effect on the dynamics of the rigid body dof.

We consider N-dof linear systems of the form

$$M\ddot{X} + KX = 0 \tag{5.1}$$

where M and K are the N-dimensional mass and stiffness matrices and $X = [x_1, x_2, \cdots, x_N]^T$ is the vector of independent generalized coordinates. The application and instantaneous removal of a constraint will change the momentum of the system but will not affect the displacements. If $[t^-, t^+]$ denotes the period of time over which the constraint is applied and removed, the evolution of the system over this interval can be mathematically described by the relations

$$X(t^+) = X(t^-) \tag{5.2}$$

$$M\dot{X}(t^+) = M\dot{X}(t^-) + I \tag{5.3}$$

where I is the N-dimensional impulse of the generalized forces. The change in kinetic energy over one cycle of constraint application and removal is given by the relation

$$\Delta E = \frac{1}{2}\dot{X}^T(t^+)\, M\, \dot{X}(t^+) - \frac{1}{2}\dot{X}^T(t^-)\, M\, \dot{X}(t^-) \tag{5.4}$$

To simplify Eq.(5.4), we premultiply Eq.(5.3) by $\dot{X}^T(t^+)$ and $\dot{X}^T(t^-)$ to obtain

$$\dot{X}^T(t^+)M\dot{X}(t^+) = \dot{X}^T(t^+)M\dot{X}(t^-) + \dot{X}^T(t^+)I \tag{5.5}$$

$$\dot{X}^T(t^-)M\dot{X}(t^+) = \dot{X}^T(t^-)M\dot{X}(t^-) + \dot{X}^T(t^-)I \tag{5.6}$$

Assuming a workless constraint, we claim

$$\dot{X}^T(t^+)I = 0 \tag{5.7}$$

Using the symmetric property of the mass matrix, we can then show from Eqs.(5.5) and (5.6) that

$$\begin{aligned} \dot{X}^T(t^+)M\dot{X}(t^+) &= \dot{X}^T(t^+)M\dot{X}(t^-) \\ &= \dot{X}^T(t^-)M\dot{X}(t^+) \\ &= \dot{X}^T(t^-)M\dot{X}(t^-) + \dot{X}^T(t^-)I \end{aligned} \tag{5.8}$$

Substitution of Eqs.(5.7) and (5.8) into Eq.(5.4) gives

$$\Delta E = \frac{1}{2}\dot{X}^T(t^-)I \tag{5.9}$$

To simplify further, we rewrite Eq.(5.3) as

$$\dot{X}(t^-) = \dot{X}(t^+) - M^{-1}I \tag{5.10}$$

The expression for $\dot{X}(t^-)$ in Eq.(5.10) is substituted in Eq.(5.9) to obtain

$$\begin{aligned} \Delta E &= \frac{1}{2}\left(\dot{X}^T(t^+)I - I^T M^{-T} I\right) \\ &= -\frac{1}{2} I^T M^{-1} I \end{aligned} \tag{5.11}$$

In simplifying Eq.(5.11) we used the relation $\dot{X}^T(t^+)I = 0$ and the symmetry of the mass matrix. The mass matrix is positive definite and thus $\Delta E \leq 0$.

5.3 Optimization Using Genetic Algorithms

In this section we consider two examples: an N-dof mass spring system and a continuous rectangular membrane system. For each example, several optimization problems are posed and solved using a genetic algorithm approach.

5.3.1 Discrete System Example: N-dof Mass Spring System

We consider the N-dof mass-spring system shown in Fig.5.2. We assume that we can apply and instantaneously remove the constraint $\dot{x}_i(t) = 0$, for any $i \in \{1, 2, \cdots, N\}$ at any time t. This physically means that mass m_i is stopped and instantaneously released. The impulse required to enforce these constraints can be easily calculated from Eq.(5.3) since the mass matrix M is diagonal. Assuming the initial and final times to be $t = 0$ and $t = T$, respectively, and that the constraint can be applied n times, we pose the following optimization problems with the objective of minimizing the total energy of the system at the final time:

P1 Given the time sequence $\{0 \leq t_1 \leq t_2 \leq \cdots \leq t_n \leq T\}$, find the number sequence $\{j_1, j_2, \cdots, j_n\}$, $j_k \in \{1, 2, \cdots, N\}$, $k = 1, 2, \cdots, n$, such that sequential application and instantaneous removal of the constraints $\dot{x}_i(t_k) = 0$

for $i = j_k$ will minimize the total energy of the system at $t = T$.

P2 Given $i \in \{1, 2, \cdots, N\}$, find the time sequence $\{0 \leq t_1 \leq t_2 \leq \cdots \leq t_n \leq T\}$ such that sequential application and instantaneous removal of the constraints $\dot{x}_i(t_k) = 0,\ k = 1, 2, \cdots, n$, will minimize the total energy of the system at $t = T$.

P3 Find the time sequence $\{0 \leq t_1 \leq t_2 \leq \cdots \leq t_n \leq T\}$ and the number sequence $\{j_1, j_2, \cdots, j_n\},\ j_k \in \{1, 2, \cdots, N\},\ k = 1, 2, \cdots, n$, such that sequential application and instantaneous removal of the constraints $\dot{x}_i(t_k) = 0$ for $i = j_k$ will minimize the total energy of the system at $t = T$.

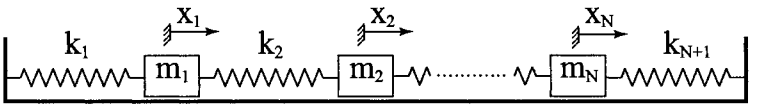

Figure 5.2. An N-dof mass spring system

The above optimization problems were solved using genetic algorithms. For each of the problems, we assumed $N = 5$, $n = 6$, and $T = 10s$. In SI units, the five masses and six spring constants were chosen randomly as follows:

$$m_1 = 0.095,\ m_2 = 0.051,\ m_3 = 0.132,\ m_4 = 0.094,\ m_5 = 0.112$$

$$k_1 = 14.5,\ k_2 = 7.31,\ k_3 = 11.06,\ k_4 = 9.85,\ k_5 = 13.91,\ k_6 = 12.62$$

The initial conditions used for simulations were chosen as:

	t_1 , j_1	t_2 , j_2	t_3 , j_3	t_4 , j_4	t_5 , j_5	t_6 , j_6
P1	1.00 , 3	2.00 , 2	3.00 , 1	4.00 , 3	5.00 , 1	6.00 , 3
P2	1.65 , 3	1.82 , 3	2.21 , 3	4.72 , 3	4.86 , 3	5.11 , 3
P3	0.26 , 3	1.00 , 1	2.00 , 3	2.71 , 1	4.71 , 4	4.85 , 4

Table 5.1. Time and number sequence for problems P1, P2 and P3

$$x_1 = 3.95,\ x_2 = 3.69,\ x_3 = 2.03,\ x_4 = 4.58,\ x_5 = 4.47$$

$$\dot{x}_1 = 0.92,\ \dot{x}_2 = 0.17,\ \dot{x}_3 = 0.93,\ \dot{x}_4 = 0.41,\ \dot{x}_5 = 0.06$$

where the units are mm and mm/s. The results of problems P1, P2 and P3 are tabulated in Tab.5.1. The plots of energy decays are shown in Fig.5.3. This figure indicate that energy of the system is reduced by 92.5% for problem P1, by 99.2% for problem P2 and by 99.3% for P3. For problem P1, a time sequence was given and the number sequence was obtained through optimization. For problem P2, a number sequence was given and the time sequence was obtained through optimization. For problem P3, both sequences were obtained through optimization and therefore it is not surprising that its solution has the maximum reduction in energy of the system.

5.3.2 Continuous System Example: Membrane

We consider a uniform rectangular membrane fixed on all sides, as shown in Fig.5.4. The natural frequencies and mode shapes for this continuous system can be written in closed form and they take the form [42]

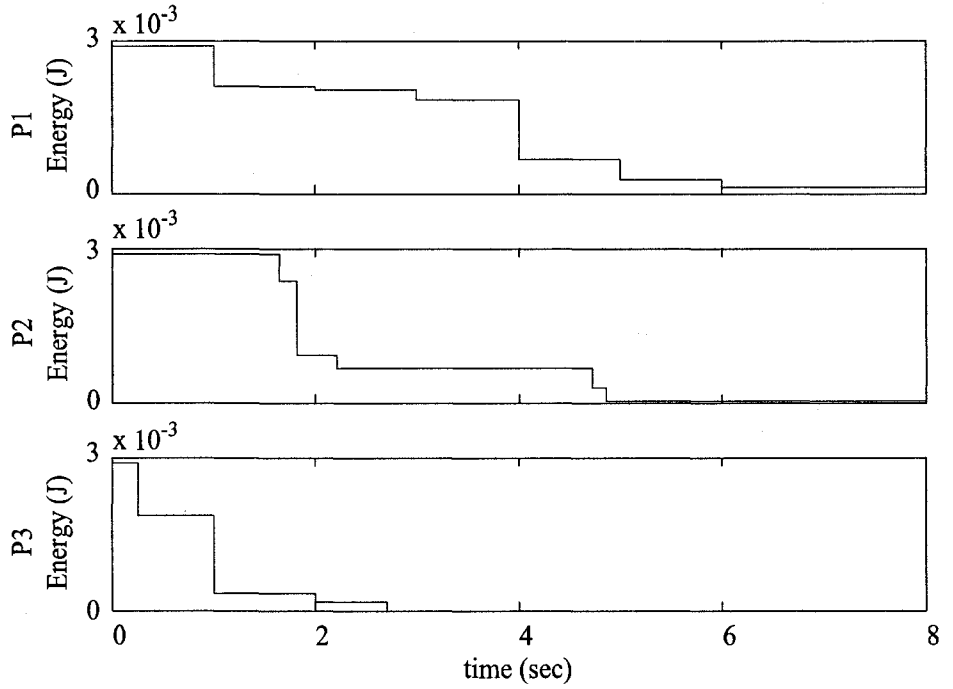

Figure 5.3. Energy decay for problems P1, P2 and P3

$$\begin{aligned} \omega_i &= \pi\sqrt{\left[\left(\frac{m}{a}\right)^2+\left(\frac{n}{b}\right)^2\right]\frac{\sigma}{\rho}} \\ W_i(x,y) &= \frac{2}{\sqrt{\rho ab}}\sin\frac{m\pi x}{a}\sin\frac{n\pi y}{b} \end{aligned} \tag{5.12}$$

where i, m and n are integers, a and b are dimensions of the membrane as shown in Fig.5.4, ρ is the mass density, and σ is the tension per unit area. In the above equations each value of i represent a mode number and is associated with a specific combination of m and n values.

We assume that a constraint of the form $\dot{z}(x_p, y_p, t) = 0$ can be applied at any time t, to any point (x_p, y_p) on the membrane, $0 < x_p < a$, $0 < y_p < b$. The application and instantaneous removal of the constraint is achieved by the application of an impulsive force $F_I\,\delta(x_p, y_p)$ at point (x_p, y_p). Assuming an N-mode model of the

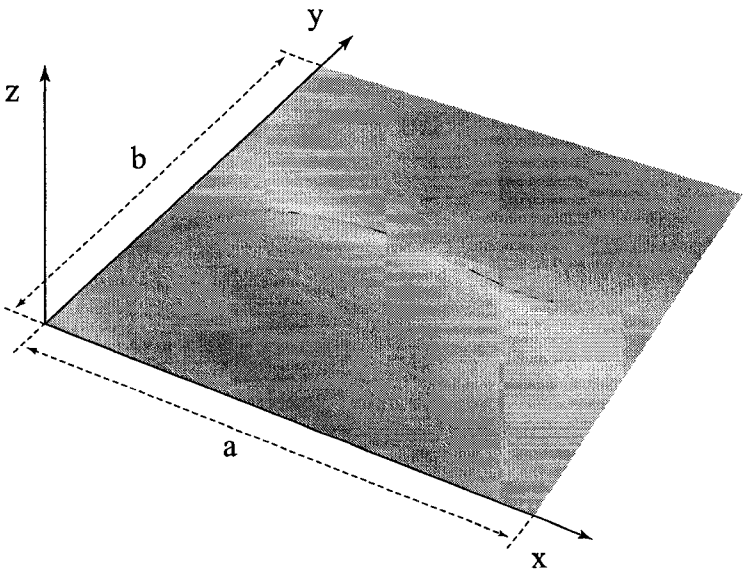

Figure 5.4. Uniform rectangular membrane fixed on all sides

membrane, the magnitude of this force can be computed using Eq.(5.3) as follows: The impulse vector I is calculated by projecting the impulsive force $F_I\,\delta(x_p, y_p)$ on the mode shapes of the system. The i^{th} entry of the impulse vector can therefore be computed as

$$\begin{aligned} I(i) &= \int_0^b \int_0^a W_i(x,y)\; F_I\,\delta(x_p, y_p)\,dx\,dy \\ &= F_I\,W_i(x_p, y_p) \end{aligned}$$

Hence, the impulse vector takes the form

$$I = F_I\left[W_1(x_p, y_p), \cdots, W_N(x_p, y_p)\right]^T \tag{5.13}$$

Let $\eta_i(t)$ and $\dot{\eta}_i(t)$ be the modal displacement and velocity of mode i. Since the mass matrix is the identity matrix in modal coordinates, the change in modal velocities due to this impulsive force can be calculated using Eq.(5.3) as follows

$$\dot{\eta}_i(t^+) = \dot{\eta}_i(t^-) + F_I W_i(x_p, y_p) \tag{5.14}$$

The magnitude of F_I required to enforce this constraint $\dot{z}(x_p, y_p, t) = 0$ can now be computed as

$$F_I = -\frac{\sum_{i=1}^{N} W_i(x_p, y_p)\dot{\eta}_i(t^-)}{\sum_{i=1}^{N} W_i(x_p, y_p)^2} \tag{5.15}$$

which follows directly from

$$\dot{z}(x_p, y_p, t) = \sum_{i=1}^{N} W_i(x_p, y_p)\dot{\eta}_i(t^+) = 0 \tag{5.16}$$

Assuming the initial and final times to be $t = 0$ and $t = T$, respectively, and that the constraint can be applied n times, we pose the following optimization problems with the objective of minimizing the total energy of the system at the final time:

P4 Given the time sequence $\{0 \leq t_1 \leq t_2 \leq \cdots \leq t_n \leq T\}$, find the location sequence $\{(x_1, y_1), \cdots, (x_n, y_n)\}$, $x_{min} < x_k < x_{max}$, $y_{min} < y_k < y_{max}$, $k = 1, 2, \cdots, n$, such that sequential application and instantaneous removal of the constraints $\dot{z}(x_i, y_i, t_i) = 0$ for $i = 1, 2, \cdots, n$ will minimize the total energy of the system at $t = T$.

P5 Given the location $(x_p, y_p) \in \{1, 2, \cdots, N\}$, find the time sequence $\{0 \leq t_1 \leq t_2 \leq \cdots \leq t_n \leq T\}$ such that sequential application and instantaneous removal of the constraints $\dot{z}(x_p, y_p, t_i) = 0$, $i = 1, 2, \cdots, n$, will minimize the total energy of the system at $t = T$.

P6 Find the time sequence $\{0 \leq t_1 \leq t_2 \leq \cdots \leq t_n \leq T\}$ and the location sequence $\{(x_1, y_1), \cdots, (x_n, y_n)\}$, $x_{min} < x_k < x_{max}$, $y_{min} < y_k < y_{max}$,

	t_1	t_2	t_3	t_4	t_5	t_6	t_7	t_8	t_9
P4	1.00	2.00	3.00	4.00	5.00	6.00	7.00	8.00	9.00
P5	0.73	1.06	2.30	2.86	3.84	5.18	5.83	6.58	9.56
P6	0.77	1.84	2.91	4.85	4.87	5.40	6.80	8.85	9.06

Table 5.2. Time sequence for problems P4, P5 and P6

$k = 1, 2, \cdots, n$, such that sequential application and instantaneous removal of the constraints $\dot{z}(x_i, y_i, t_i) = 0$ for $i = 1, 2, \cdots, n$ will minimize the total energy of the system at $t = T$.

For our numerical simulations, we assumed $n = 9$, $T = 10\ s$ and

$$x_{min} = 0.15\ m \qquad x_{max} = 0.85\ m$$
$$y_{min} = 0.15\ m \qquad y_{max} = 1.05\ m$$

For the membrane, we chose the following geometric and material properties: $a = 1.0$ m, $b = 1.2\ m$, $\rho = 800\ kg/m^3$ and $\sigma = 600\ N/m^2$. A 10-mode model of the membranes was considered, *i.e.* $N = 10$. The initial conditions were chosen to be the same for all modes and equal to $\eta_i(t_0) = 0.001$ and $\dot{\eta}_i(t_0) = 0.001$.

The results of simulations for problems P4, P5 and P6 are shown in Tab.5.2, and Tab.5.3. The corresponding plots of energy decay are shown in Fig.5.5. They demonstrate an energy reduction of 86.3% for problem P4, 69.3% for problem P5 and 94.0% for problem P6. For P5, we choose $x_p = 0.3\ m$ and $y_p = 0.7\ m$. For problems P4 and P6 we imposed the additional restriction that the points of application of constraints satisfy $x_{min} < x_k < x_{max}$, $y_{min} < y_k < y_{max}$, $k = 1, 2, \cdots, n$. This was done to avoid a large impulsive force needed to enforce the constraint at points that

		t_1	t_2	t_3	t_4	t_5	t_6	t_7	t_8	t_9
P4	x	0.85	0.62	0.73	0.48	0.23	0.21	0.68	0.40	0.85
	y	0.81	0.97	0.62	0.35	1.05	0.52	0.85	0.15	0.43
P6	x	0.22	0.43	0.27	0.25	0.22	0.41	0.23	0.17	0.17
	y	0.96	0.79	0.69	1.03	1.00	0.44	0.90	0.88	0.29

Table 5.3. Location sequence for problems P4 and P6

are close to the boundary. The location sequence for P4 and P6 are shown in Fig.5.6.

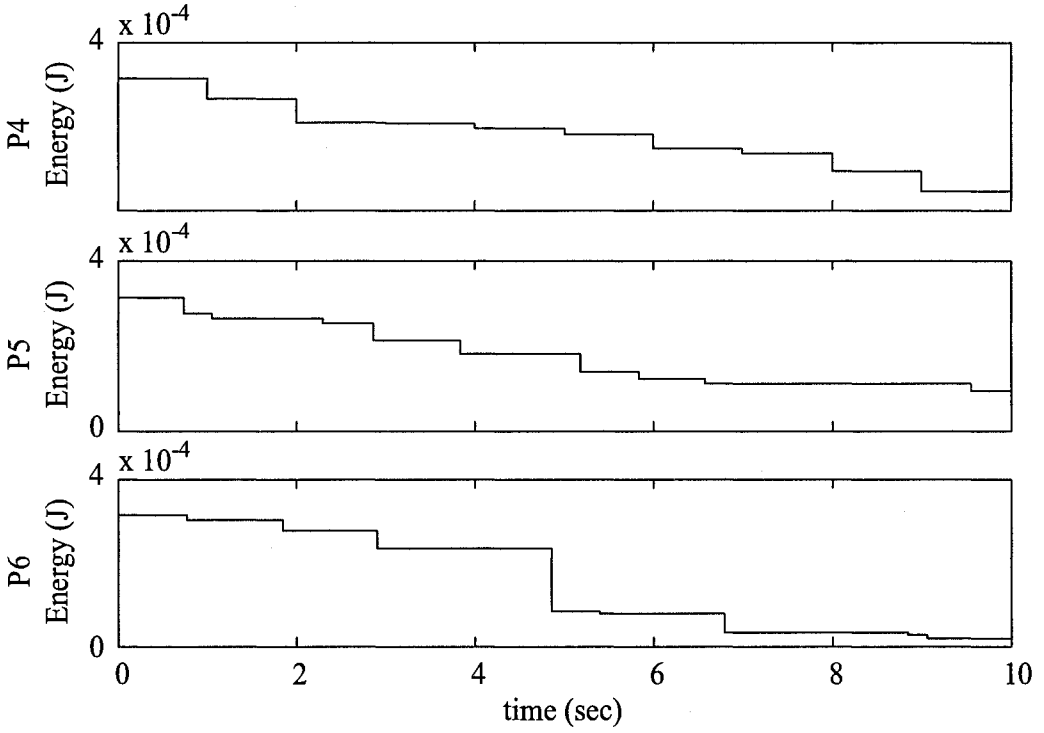

Figure 5.5. Energy decay for problems P4, P5 and P6

5.4 Gradient Based Optimization Method

The membrane example in section 5.3.2 is revisited in this section and solved using a gradient-based optimization method. Specifically, the method of moving asymptotes

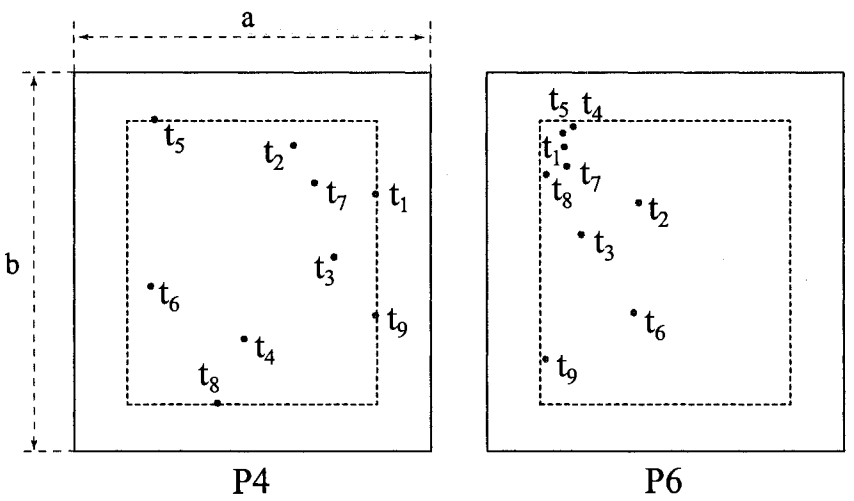

Figure 5.6. Location sequence for problems P4 and P6

(MMA) [43] is used. This method can be used to solve optimization problems for continuous systems and thus the mass-spring system of section 5.3.1 is not revisited. We present the derivation necessary and solve optimization problem P4 in the next section. The derivations needed for problems P5 and P6 can be carried out in a similar manner and are not presented.

5.4.1 Objective function

We restate problem P4 as follows: Given the time sequence $\{0 \leq t_1 \leq t_2 \leq \cdots \leq t_n \leq T\}$, find $p = \{(x_1, y_1), \cdots, (x_n, y_n)\} \in R^{2\times n}$ that will

$$\text{maximize} \qquad f = \frac{1}{2}\sum_{i=1}^{n} I_i^T I_i \tag{5.17}$$

$$\text{subject to} \qquad \begin{array}{ccccc} x_{min} & < & x_k & < & x_{max} \\ y_{min} & < & y_k & < & y_{max} \end{array} \tag{5.18}$$

In Eq.(5.17), I_i is the impulse vector resulting from application and instantaneous removal of the constraint $\dot{z}(x_i, y_i, t_i) = 0$ at time t_i. It is calculated from Eqs.(5.13)

and (5.15) and takes the form

$$I_i = \left[C_i^T U(t_i^-)\right] B_i \tag{5.19}$$

where

$$\begin{aligned} B_i &= [0, \cdots, 0, W_1(x_i, y_i), \cdots, W_N(x_i, y_i)]^T \\ U(t) &= [\eta_1(t), \cdots, \eta_N(t), \dot{\eta}_1(t), \cdots, \dot{\eta}_N(t)]^T \\ C_i &= \frac{1}{\sum_{j=1}^{N} W_j(x_i, y_i)^2} [0, \cdots, 0, W_1(x_i, y_i), \cdots, W_N(x_i, y_i)]^T \end{aligned}$$

In the above expressions, $U(t)$ denotes the vector of state variables at time t. Starting from the initial state $U(t_0)$, $U(t_i^-)$ and I_i are calculated recursively as follows.

$$\begin{aligned} U(t_1^-) &= \Phi_1 \, U(t_0) \\ U(t_1^+) &= \Phi_1 \, U(t_0) + I_1 \\ U(t_2^-) &= \Phi_2 \Phi_1 \, U(t_0) + \Phi_2 I_1 \\ U(t_2^+) &= \Phi_2 \Phi_1 \, U(t_0) + \Phi_2 I_1 + I_2 \\ \vdots \quad & \quad \vdots \quad \quad \vdots \quad \quad \vdots \\ U(t_i^-) &= \prod_{j=1}^{i} \Phi_j \, U(t_0) + \sum_{j=1}^{i-1} \prod_{k=j+1}^{i} \Phi_k I_j \\ U(t_i^+) &= \prod_{j=1}^{i} \Phi_j \, U(t_0) + \sum_{j=1}^{i-1} \prod_{k=j+1}^{i} \Phi_k I_j + I_i \\ \vdots \quad & \quad \vdots \quad \quad \vdots \quad \quad \vdots \\ U(t_n^-) &= \prod_{j=1}^{n} \Phi_j \, U(t_0) + \sum_{j=1}^{n-1} \prod_{k=j+1}^{n} \Phi_k I_j \\ U(t_n^+) &= \prod_{j=1}^{n} \Phi_j \, U(t_0) + \sum_{j=1}^{n-1} \prod_{k=j+1}^{n} \Phi_k I_j + I_n \end{aligned} \tag{5.20}$$

where

$$\Phi_i = e^{A\Delta t} \qquad \text{and} \qquad A = \begin{bmatrix} 0_N & 1_N \\ -\Omega & 0_N \end{bmatrix} \tag{5.21}$$

In Eq.(5.21), $\Delta t = (t_i - t_{i-1})$, $i = 1, 2, \cdots, n$, denotes the time interval between successive impacts and $\Omega = diag(\omega_j^2)$ is the $N \times N$ stiffness matrix of the system. 1_N

and 0_N are the $N \times N$ identity and zero matrices respectively. The expression for Φ_i can be obtained in closed form as follows

$$\Phi_i = \begin{bmatrix} diag\left[\cos(\omega_j \Delta t)\right] & diag\left[\sin(\omega_j \Delta t)/\omega_j\right] \\ -diag\left[\omega_j \sin(\omega_j \Delta t)\right] & diag\left[\cos(\omega_j \Delta t)\right] \end{bmatrix} \tag{5.22}$$

where $diag\left[\cos(\omega_j \Delta t)\right]$, $diag\left[\sin(\omega_j \Delta t)/\omega_j\right]$, $diag\left[\omega_j \sin(\omega_j \Delta t)\right]$ and $diag\left[\cos(\omega_j \Delta t)\right]$ are $N \times N$ diagonal matrices with $\left[\cos(\omega_j \Delta t)\right]$, $\left[\sin(\omega_j \Delta t)/\omega_j\right]$, $\left[\omega_j \sin(\omega_j \Delta t)\right]$ and $\left[\cos(\omega_j \Delta t)\right]$ as their j-th entries, respectively, $j = 1, \cdots, N$.

5.4.2 Sensitivity Analysis

The gradient of the objective function in Eq.(5.17) needed for the optimization algorithm is computed as follows

$$\frac{\partial f}{\partial p} = \sum_{i=1}^{n} I_i^T \frac{\partial I_i}{\partial p} \tag{5.23}$$

Using Eq.(5.19), $\dfrac{\partial I_i}{\partial p}$ can be computed as follows

$$\frac{\partial I_i}{\partial p} = B_i \otimes \left[U(t_i^-)^T \frac{\partial C_i}{\partial p} + C_i^T \frac{\partial U(t_i^-)}{\partial p} \right] + \left[C_i^T U(t_i^-) \right] \frac{\partial B_i}{\partial p} \tag{5.24}$$

In the above equation, $\dfrac{\partial C_i}{\partial p}$ and $\dfrac{\partial B_i}{\partial p}$ can be computed directly because they are expressed in terms of x_i and y_i. The evaluation of $\dfrac{\partial U(t_i^-)}{\partial p}$ is more involved and requires recursive computations, as shown below:

$$\frac{\partial U(t_i^-)}{\partial p} = \sum_{j=1}^{i-1} \prod_{k=j+1}^{i} \Phi_k \frac{\partial I_j}{\partial p}$$

		t_1	t_2	t_3	t_4	t_5	t_6	t_7	t_8	t_9
S1	x	0.73	0.70	0.29	0.71	0.60	0.69	0.62	0.17	0.19
	y	0.41	0.72	0.57	0.39	0.42	0.36	0.58	0.39	0.26
S2	x	0.43	0.48	0.35	0.33	0.67	0.70	0.20	0.31	0.57
	y	0.60	0.68	0.25	0.46	0.48	0.54	0.24	0.82	0.21

Table 5.4. Location sequence for problems S1 and S2

The gradient of the objective function in Eq.(5.23) is used in the MMA algorithm to iteratively converge to an optimal solution starting from an initial guess.

5.4.3 Numerical Simulations

The material and geometric properties of the membrane were assumed to be the same as those used in section 5.3.2. A 10-mode model of the membrane was considered ($N = 10$) and the total time of simulation was set to $T = 10$ *sec.* The constraint was applied and instantaneously removed nine times ($n = 9$) and the time sequence was chosen to be the same as that used for simulation of P4 given in table 5.2. The constraints imposed on the solution, given by Eq.(5.18), were chosen as: $x_{min} = 0.15$ m, $x_{max} = 0.85$ m, $y_{min} = 0.15$ m and $y_{max} = 1.05$ m. The initial condition was assumed to be $U(t_0) = 0.001\,[1, \cdots, 1]^T$; this corresponds to initial energy of the system equal to 31.2×10^{-5} J. We present results of two simulations, S1 and S2, obtained from two different initial guesses for the optimal solution. Figure 5.7 shows the energy decay and Fig.5.8 indicates the locations of constraint application on the membrane. The exact locations are tabulated in Tab.5.4. For simulations S1 and S2 the final energies were 6.59×10^{-5} J and 9.4×10^{-5} J, a reduction of 78.9% and 69.9%, respectively. Clearly, the results of optimization depend on the initial guess since the solutions obtained are not global optima.

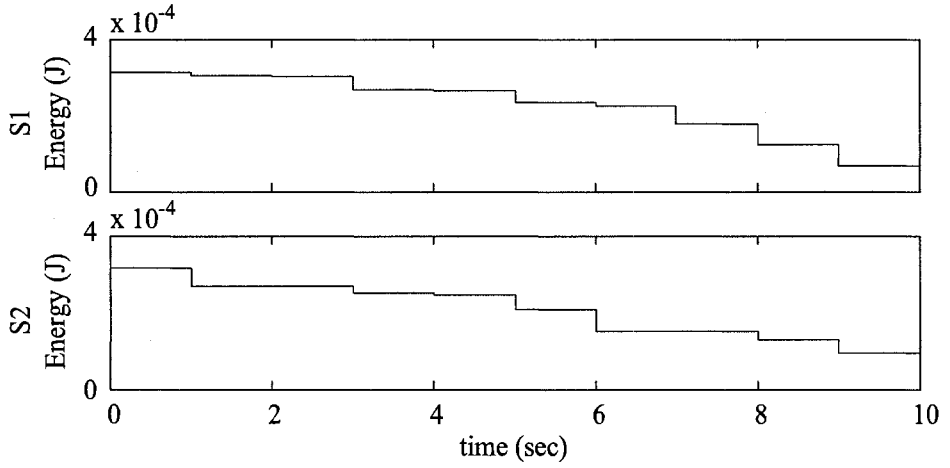

Figure 5.7. Energy decay for simulations S1 and S2

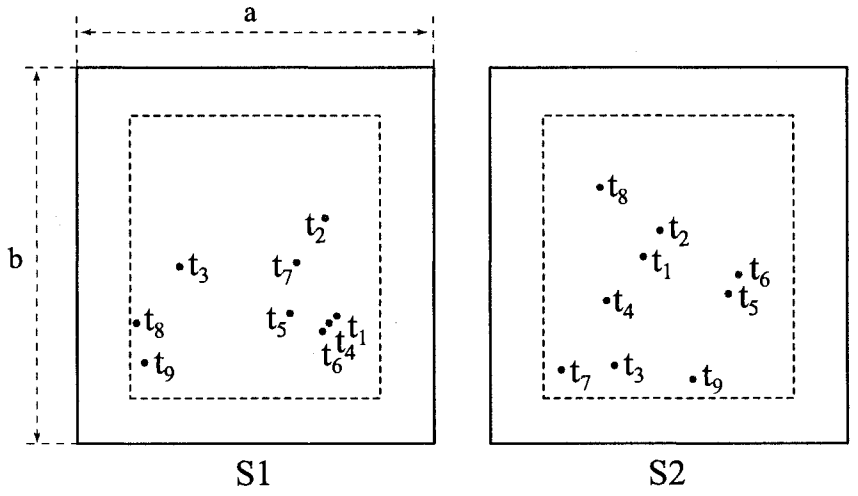

Figure 5.8. Location sequence for simulations S1 and S2

5.5 Remarks

In the last chapter it was shown that a strategy based on sequential application of constraints can be used to significantly eliminate vibration energy from a finite dof system. While it may seem obvious that imposition of a constraint that freezes the motion of a dof will remove kinetic energy, as a general strategy energy removal by constraint application reaches its full potential only in the context of an associated optimization problem. A number of formulations of the optimization problem are possible and can be adjusted depending on the design goal and the amount of freedom available to design the system. The formulations explored in this chapter are simple, yet they demonstrate performance when different goals are considered. Other formulations could, for instance, account for the cost of applying the constraint using more complex cost models. Such modifications could be incorporated easily within the present framework and the problems presented hint to how to use these ideas to solve more complex problems. The genetic and the gradient-based algorithms used are simple to implement and result in reasonable energy extraction, although no effort was invested in ascertaining whether the solutions obtained are actually global optima.

CHAPTER 6

Vibration Suppression Using Cable Actuators

6.1 Introduction

The results presented in this chapter are part of the active control strategy discussed in the introduction. It is an extension of the work of Nudehi et al. [26] where cable actuators were used for vibration suppression in a cantilever beam. In this chapter we extend the results to the general case of frame structures. The vibration modes of the beam studied in Nudehi et al. [26] lie in a single plane but this is not the case for general frame structures. As a result, the cable actuators have two distinguishing effects: the first is a parametric effect where the stiffness of the structure is affected by the cable tension, and the second is a direct effect by which external forces are applied to the structure. In general cabled structures both effects are present but in most cases one of them is the dominant or sole effect. In section 6.2 we summarize the work of Nudehi et al., and extend it to motivate the present study. In section 6.3 a dynamic model, which describes the dynamics of a structure formed by frame elements and cables, is presented. The model is based on finite elements for the frame and a linear cable element in which sag, coupling, and other such effects, are neglected. In section 6.4 a general control scheme is presented and described. In section 6.5, we explore the

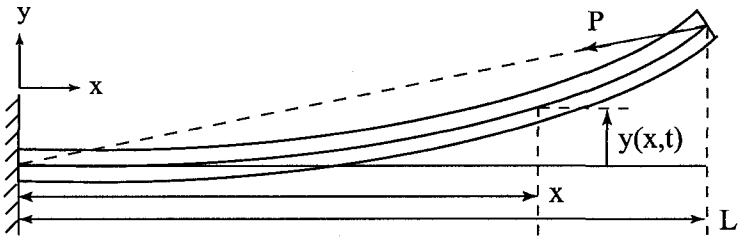

Figure 6.1. Cantilever beam with cable-supplied end force.

idea of active stiffness variation on a frame structure, placing particular emphasis on the importance of the cable placement on the structure, and a performance function is proposed for quantitatively assessing its effectiveness in terms of control. Numerical simulations for several choices of cable placements are shown for a particular frame model. In section 6.6 the direct effect of transverse cable force is examined; we consider the special case in which the structural stiffness change due to cable effects is small. Numerical simulations and experimental results are presented for a sample frame. Some conclusions and directions for future work are addressed in Section 6.7.

6.2 Background

The idea of stiffness variation for vibration control of a beam using a cable-supplied end load was investigated by Nudehi et al. [26]. In this section we briefly review that work and use it to demonstrate the effects of cable placement. While these results are quite straightforward in this beam application, they provide the basis for evaluating more complex structures, as described subsequently. The results of Nudehi et al. [26] were based on a uniform cantilever beam of length L subjected to an end load P whose line of action is directed from the free end of the beam to its base; see Fig.6.1. Assuming Euler-Bernoulli beam theory, the beam equation of motion and boundary conditions can be written as follows,

$$EI\, y'''' + P\, y'' + \rho A\, \ddot{y} = 0. \tag{6.1}$$

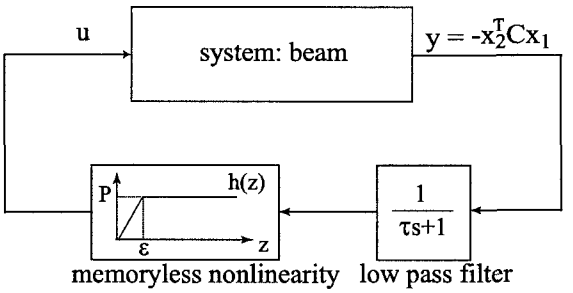

Figure 6.2. Control Scheme

The geometric boundary conditions are

$$y(0,t) = 0, \qquad y'(0,t) = 0$$

and the natural boundary conditions are

$$y''(L,t) = 0, \qquad EIy'''(L,t) + P\{y'(L,t) - \tfrac{1}{L}y(L,t)\} = 0.$$

In Eq.(6.1), E and ρ are Young's modulus of elasticity and density of the beam, respectively, I is the second moment of cross-sectional area, and y' and $\dot{y}$ denote the partial derivatives of $y(x,t)$ with respect to x and t, respectively. Note that the end load P appears in a unique manner in the boundary conditions, but it enters the field equation the same as if it were a compressive buckling or flutter type load. Using the first N normalized mode shapes of a cantilever beam, the beam model is approximated by projecting the partial differential equation onto these modes and expressing the resulting ordinary differential equations in state space form, resulting in:

$$\begin{aligned} \dot{x}_1 &= x_2 \\ \dot{x}_2 &= -Kx_1 - Dx_2 + Cx_1u \end{aligned} \tag{6.2}$$

In Eq.(6.2), x_1 is the modal amplitude vector, x_2 is the modal velocity vector, K is the stiffness matrix, D is the damping matrix, u is the cable tension ($u = P$),

Table 6.1. Material and geometric properties of the experimental beam.

Material	Aluminum
Young's Modulus	70 GPa
Density	2730 Kg/m^3
Dimensions	$1.25 \times 0.05 \times 0.003$ m

and C is the stiffness change corresponding to a unit tension. Initially, it was found using passivity analysis, that if energy was to be removed from the system, tension should be applied in the cable only when the output function $y = -x_2^T C x_1$ is positive. Then, a low pass filter was added to remove the high frequency content of the output y, thereby providing a signal that is consistent with the actuator bandwidth. A memoryless nonlinearity was included to account for the unilateral nature of the control action and to proportionally reduce the control action as the system vibration dies out. This control scheme is depicted in Fig.6.2.

An experimental setup was built to demonstrate the approach, in which a dc motor provided the cable tension. The material and geometric properties of the beam are provided in Tab.6.1. The cable tension was switched between 20-22N in one case and 20-24N in another case. The 20N bias tension was applied to the cable to prevent slack. The first mode vibration of the beam was successfully suppressed using this approach, as shown in Fig.6.3.

In order to demonstrate the effects of cable placement, the model is adapted here to allow for cable placement anywhere along the beam. Of course, in this case moving the cable closer to the base will reduce the control authority of the cable, and thus reduce its effectiveness. Our aim is to capture this effect in the equations of motion, so that it can be investigated for more complex structural systems. In the first configuration, designated Case I, the cable is connected from the base to the tip, as shown in Fig.6.1. In Case II the cable is assumed to be connected

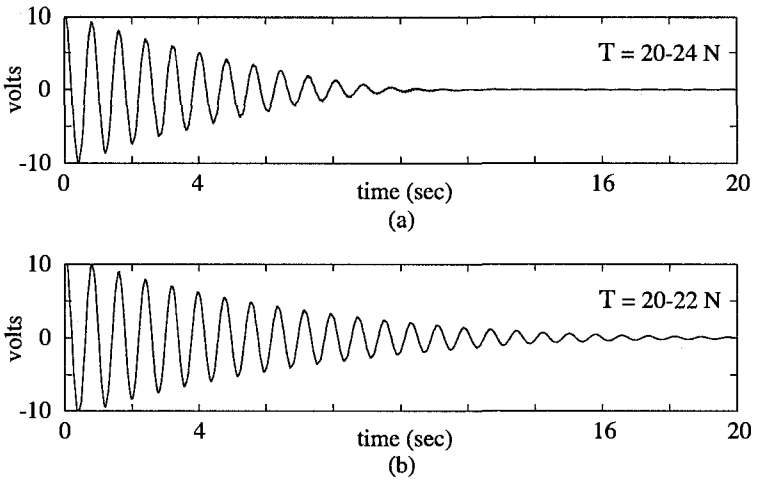

Figure 6.3. Experimental results of the first mode, showing vibration suppression from the cable forces.

from the base to a point at $x = 3L/4$, and in Case III the cable is attached at $x = L/2$. A two-mode approximation of the beam dynamics is considered. In Eq.(6.2), the K and the D matrices will remain unchanged for the three cases but the C matrix will change. These matrices, including C for all three cases, are given by:

$$K = \begin{bmatrix} 97.38 & 0.0 \\ 0.0 & 3824.39 \end{bmatrix} \qquad D = \begin{bmatrix} 0.098 & 0.0 \\ 0.0 & 0.618 \end{bmatrix}$$

C in Case I	C in Case II	C in Case III
$\begin{bmatrix} 1.0 & -5.28 \\ -5.28 & 44.41 \end{bmatrix}$	$\begin{bmatrix} 0.16 & -2.10 \\ -2.10 & 28.81 \end{bmatrix}$	$\begin{bmatrix} 0.01 & -0.25 \\ -0.25 & 5.58 \end{bmatrix}$

The results of numerical simulations for the three cases are shown in Fig.6.4. The control scheme in Fig.6.2 was used with $T = 35N$, $\varepsilon = 1.0 \times e^{-4}$, and the cut-off frequency of the low pass filter was set at 15 rad/s. The following initial conditions (in SI units) were used,

$$
\begin{aligned}
x_1(0) &= \begin{bmatrix} a_1(0) \\ a_2(0) \end{bmatrix} = \begin{bmatrix} 0.1 \\ 0.02 \end{bmatrix}, \\
x_2(0) &= \begin{bmatrix} \dot{a}_1(0) \\ \dot{a}_2(0) \end{bmatrix} = \begin{bmatrix} 0.0 \\ 0.0 \end{bmatrix}
\end{aligned}
\tag{6.3}
$$

It is clear that a shorter cable results in lesser control authority. It is also clear that the C matrix is key to quantifying the level of control authority and thus some norm of C should be useful for assessing the control effectiveness of cable placement. This observation motivates the question of finding a method for determining an optimal location of the cable. In the case of the beam the cable placement is limited to be along the beam, making the optimization problem simple, but in a three-dimensional structure the cable can be placed between any two points on the structure, and the assessment and optimization become more complicated.

6.3 Modeling Of Cabled Frame Structures

In this section we present a mathematical model that describes the dynamic behavior of a structure made of frame elements and cables. Finite element analysis is used to derive the equation of motion of the system. Two elements are needed to completely describe the structural dynamics, a frame element, which is well known, and a cable element, which is proposed below. The frame element is shown in Fig.6.5; it has two nodes, N_1 and N_2, and six dof[1] per node, 3 displacements and 3 rotations. It carries an axial load P, which is taken to be positive in compression. Its geometric and material properties are defined as follows: A is the cross sectional area, I is the second moment of cross-sectional area, J is the polar moment of cross-sectional area, ρ is the density, E is the Young's modulus, and G is the shear modulus of elasticity. We denote $u(x,t)$ and $\theta_x(x,t)$ as its longitudinal displacement and twist

[1]degrees-of-freedom

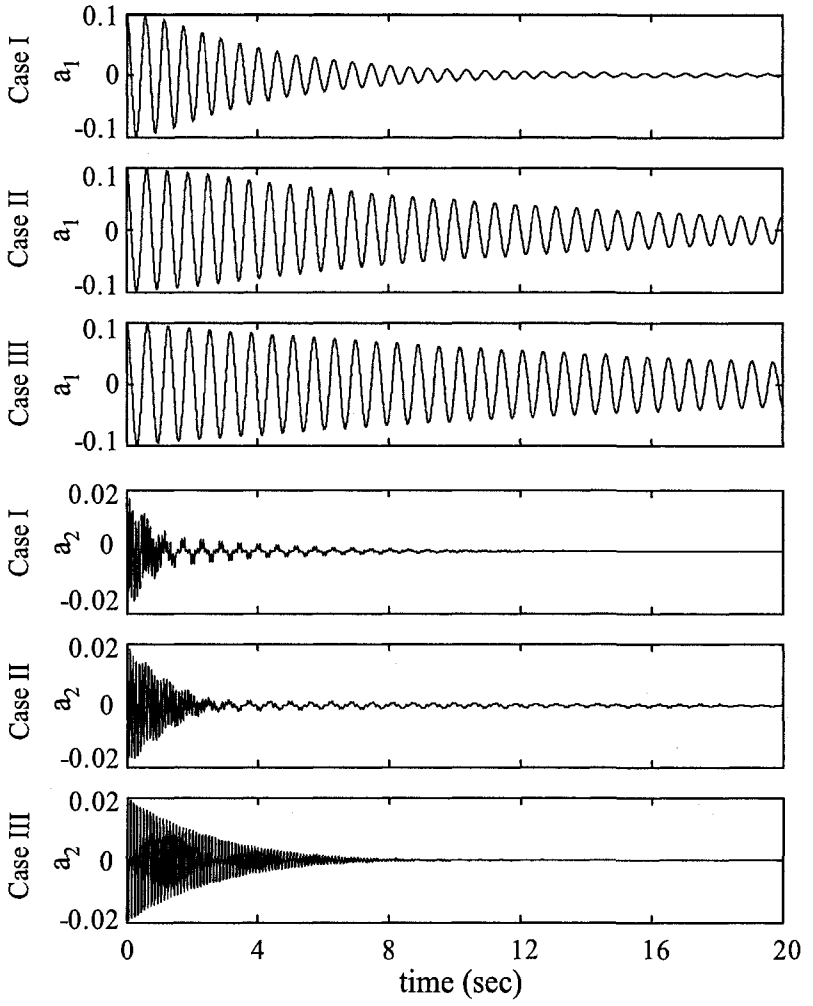

Figure 6.4. Simulation of decay in modal amplitudes a_1 and a_2 due to the control shown in Fig.6.2, for cable configuration in Case I (connection at $x = L$), Case II ($x = 3L/4$), and Case III ($x = L/2$).

angle, respectively, and $v(x,t)$ and $w(x,t)$ as the transverse element displacements along the y-axis and z-axis, respectively. In terms of these parameters and variables, the frame element linear equations of motion are given by:

$$\begin{aligned} \rho A\, \ddot{u} &= AE\, u'' & \rho A\, \ddot{v} + EI\, v'''' + P\, v'' &= 0 \\ \rho J\, \ddot{\theta}_x &= GJ\, \theta_x'' & \rho A\, \ddot{w} + EI\, w'''' + P\, w'' &= 0 \end{aligned} \tag{6.4}$$

where the first two equations describe the longitudinal and the torsional vibration of

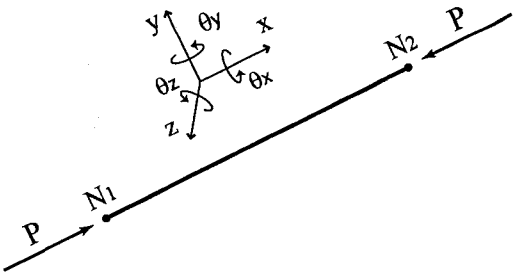

Figure 6.5. Frame element

the element, respectively, and the latter two equations describe the transverse vibration of the element in the x-y and x-z planes, respectively. As per standard notation, f' and $\dot{f}$ denote the partial derivatives of f with respect to x and t, respectively. The elementary mass matrix, stiffness matrix and geometric stiffness matrix for such an element are standard; see Reddy [28], for example.

The effects of the element axial forces P, which are induced by cable and other loads, are only one factor contributing to the change in stiffness of the structure. Another factor is the spring-back forces created at the cable-structure interface points. We define a cable element to be any part of the cable that connects any two different nodes, say N_1 and N_2, on the structure. Let T be the cable element tension. When the structure deforms, each cable element acts like a spring and applies a restoring force at each of the nodes where it is attached to the structure. Assuming small deformations, these restoring forces are linearly dependent on the displacements of the interface nodes. A cable element stiffness matrix can be added to the usual stiffness matrix to account for these effects, as follows. The 3D deflections of the cable element are projected onto the x-y and x-z planes, where (u_i, v_i, w_i) are the displacements of the node N_i along the x-axis, the y-axis and the z-axis, respectively, as shown in Fig.6.6. The tension in this element is T. The cable restoring forces $F_{v_1}, F_{v_2}, F_{w_1}$, and F_{w_2} are determined from the geometry of the figure, and are given as follows:

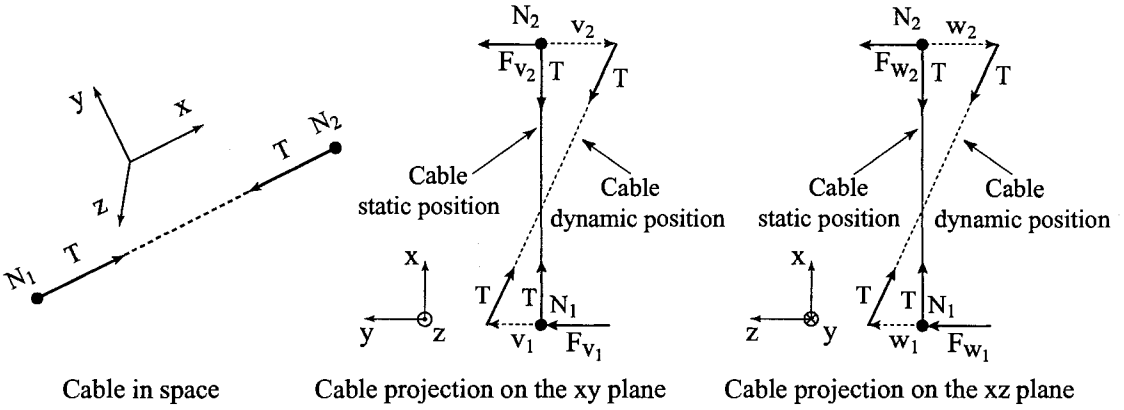

Figure 6.6. Cable element and its projections on the x-y and x-z planes

$$
\begin{aligned}
F_{v_1} &\simeq -T(v_1 - v_2)/l_c \qquad & F_{w_1} &\simeq -T(w_1 - w_2)/l_c \\
F_{v_2} &\simeq -T(v_2 - v_1)/l_c \qquad & F_{w_2} &\simeq -T(w_2 - w_1)/l_c.
\end{aligned}
\tag{6.5}
$$

In Eq.(6.5) all nonlinear effects, such as sag in the cable, are ignored. It is also assumed that the cable tension T and cable length are constant, that is, independent of the deformation. Using these assumptions the restoring forces in Eq.(6.5) can be rewritten in matrix form, from which one can obtain the cable elementary stiffness matrix K_c, as follows,

$$
\begin{bmatrix} -F_{v_1} \\ -F_{w_1} \\ -F_{v_2} \\ -F_{w_2} \end{bmatrix} = \frac{T}{l_c} \begin{bmatrix} 1 & 0 & -1 & 0 \\ 0 & 1 & 0 & -1 \\ -1 & 0 & 1 & 0 \\ 0 & -1 & 0 & 1 \end{bmatrix} \begin{bmatrix} v_1 \\ w_1 \\ v_2 \\ w_2 \end{bmatrix} \tag{6.6}
$$

$$
\Rightarrow \qquad K_c = \frac{T}{l_c} \begin{bmatrix} 1 & 0 & -1 & 0 \\ 0 & 1 & 0 & -1 \\ -1 & 0 & 1 & 0 \\ 0 & -1 & 0 & 1 \end{bmatrix}. \tag{6.7}
$$

This stiffness is mapped into the global stiffness matrix of the system. After adding the cable structure interface to the system, and ignoring the inertial effects of the

cable, the numerical model is developed using finite elements and will take the form of as

$$M\ddot{X} + (K - T\,K_g)X = T\,F. \tag{6.8}$$

In this equation M and K are the mass and stiffness matrices of the system without the cable, F is the forcing vector corresponding to a unit tension in the cable and X is the vector of nodal displacements and rotations. K_g is the geometric stiffness matrix which includes both axial loading and cable effects, calculated assuming a unit tension. The total geometric effect from the cable on the system is $T\ K_g$, which results from the attendant axial loading in the frame elements (the part of P that arises from T, calculated in the static state) and the stiffness effect due to cable elements. Both of these effects are proportional to T. The resulting system is analyzed to determine the system vibration modes. A coordinate transformation is carried out to express the equations of motion in terms of modal amplitudes. This model is truncated to n modes, resulting in the following form for the equations of motion for the retained modal amplitudes η,

$$\ddot{\eta} + D\dot{\eta} + (\Omega - T\,k_g)\eta = T\,f \tag{6.9}$$

In Eq.(6.9), k_g is the $n \times n$ modal geometric stiffness matrix, $\Omega = diag(\omega_i^2)$ is the diagonal matrix of zero-tension natural frequencies, $D = diag(2\xi_i\omega_i)$ is the diagonal modal equivalent viscous damping matrix in which ξ_i are the modal damping ratios, and f is the modal forcing vector corresponding to a unit tension in the cable. It is clear from Eqs.(6.8) and (6.9) that the cable has two distinct effects on the system. The first is a parametric effect in which it alters the system stiffness, and the second is a direct effect where it provides directly applied forces. Both effects will be considered in the control design described in the next sections.

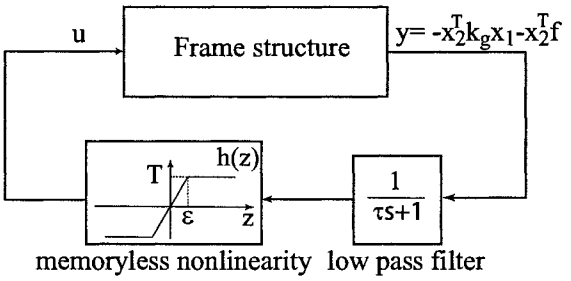

Figure 6.7. Feedback

6.4 Control Scheme Design

In this section we propose a control design for the system described in Eq.(6.9) by generalizing the results of Nudehi et al. [26]. We first write the state space form of the closed loop in Fig.6.7 as follows:

$$\begin{aligned} \dot{x}_1 &= x_2 \\ \dot{x}_2 &= -\Omega x_1 - D x_2 + \left(k_g x_1 + f\right) h(z) \\ \dot{z} &= \frac{1}{\tau}\left(x_2^T k_g x_1 + x_2^T f\right) - \frac{1}{\tau} z \end{aligned} \tag{6.10}$$

where, $x_1 \in R^N$ is the vector of modal displacements, $x_2 \in R^N$ is the vector of modal velocities and $z \in R$ is the state of the low-pass filter. The cable tension is the control input, that is, $u = h(z) = T$. Similar to the control design in Sec.6.2, passivity analysis is used to prove that tension in the cable should be applied to maintain the inequality $u^T y = u^T\left(-x_2^T k_g x_1 - x_2^T f\right) \geq 0$, which removes energy from the system. The high frequency components of y are attenuated by the use of a low-pass filter in order to avoid spillover. To reduce chattering, the output of the filter is passed through a memoryless nonlinearity with a saturation function.

The origin of the closed-loop system in Fig.6.7 is shown to be globally asymptotically stable using the following Lyapunov function candidate:

$$V(x_1, x_2, z) = \frac{1}{2}\left(x_1^T \Omega x_1 + x_2^T x_2\right) + \tau \int_0^z h(\sigma) d\sigma. \tag{6.11}$$

The derivative of the lyapunov function is found to be

$$\begin{aligned} \dot{V} &= \dot{x}_1^T \Omega x_1 + \dot{x}_2^T x_2 + \tau h(z)\dot{z} \\ &= -x_2^T D x_2 - z h(z) \end{aligned} \tag{6.12}$$

In the above equation, $\dot{V} \leq 0$ since D is positive definite and $h(z)$ is passive. Also $\dot{V} = 0$ implies $x_2 = 0$ and $z = 0$. Furthermore, from Eq.(6.10) $x_2 = 0$ and $z = 0$ implies $x_1 = 0$. Since $V(x_1, x_2, z)$ is radially unbounded, we can use LaSalle's theorem [44] to claim global asymptotic stability of the origin $(x_1, x_2, z) = (0, 0, 0)$.

In implementation of the above approach, one needs to measure or estimate vibration modal amplitudes. It is important to note that when $z < 0$ the cable tension will be negative. To avoid this situation, a bias tension T_0 is applied where T_0 is chosen to be more than the maximum control effort T and less than the critical load. Although a bias tension will alter the equilibrium configuration of the system in the general case, proper cable placement can ensure that the change in the equilibrium configuration is insignificant. In the next two sections we conduct two separate studies. In the first study, the parametric effect is considered, *i.e.*, $f = 0$ in Eq.(6.9), and the effect of cable placement is explored. In the second study we address the case of direct cable control assuming the geometric stiffness k_g is negligible.

6.5 Control By Stiffness Variation

6.5.1 Problem Definition

The parametric cable control of the closed loop system in Fig.6.7 is studied. It is assumed that the cable is wrapped around the structure in a way that renders the

modal forcing vector to be zero, *i.e.*, $f = 0$. This corresponds to a physical situation in which the cable tension does not affect the static configuration of the system, at least for the truncated modal description of the system. Such arrangements are possible, and are not difficult to achieve in structures that are essentially one or two dimensional. An important consideration that will be investigated is how the placement of the cable will influence the control. In this section, we will identify the parameters that determine the control authority and present numerical simulations for a specific example.

6.5.2 Cable Placement

An important consideration in this class of problems is to develop a systematic method for assessing and comparing various cable placements, which will be useful for determining an optimal location that maximizes the control authority of the cable on the structure. Actuator and sensor locations have been widely studied, especially for linear systems; see Hamdan and Nayfeh [45] and Sadri et al. [46], for example. Unfortunately, these criteria can not be applied in the present case, due to the nonlinear nature of the system. Also, unlike other actuators, the cable tendon is unique in the fact that the overall effect of the force transmitted to the structure can be significantly increased by rerouting the cable through pulleys at different points on the structure. A single actuator is needed to apply the tension in the cable which can then be connected to multiple locations on the structure. Here we investigate cable placement for an undamped system, since we are interested in energy dissipation solely due to parametric cable control. The equation of motion for this class of systems is a special case of Eq.(6.9):

$$\ddot{\eta} + (\Omega - Tk_g)\eta = 0. \tag{6.13}$$

The cable placement will affect only the geometric stiffness matrix k_g. This stiffness

matrix is directly related to the negative work done by the cable tension that is described by the term, $Tk_g\eta$. It is clear that some norm of the geometric stiffness matrix k_g can be a measure of the control authority of the cable. The cable placement problem will be approached by first applying a change of variables that decouples the stiffness matrix of the system, and the desired criteria will be based on the new form of the geometric stiffness. Let ϕ be the $n \times n$ transformation matrix that diagonalize the two symmetric matrices Ω and k_g. The statement of this generalized eigenvalue problem and its consequences for the two matrices are given by:

$$\Omega\phi = \lambda k_g \phi \tag{6.14}$$

with

$$\phi^T k_g \phi = diag(1/T_i), \quad \phi^T \Omega \phi = I_{n\times n}$$

where $\lambda = diag(T_i)$ are the eigenvalues, ϕ is normalized with respect to the Ω matrix, *i.e.*, $\phi^T\Omega\phi = I_{n\times n}$, and T_i's are the buckling loads for the modes, as confirmed below. For convenience, the eignvectors that compose ϕ are ordered so that $|T_i| < |T_{i+1}|$. Performing the change of variables $\eta = \phi\sigma$, where σ is an $(n \times 1)$ vector of the new set of displacement variables, and multiplying Eq.(6.13) by ϕ^T, we get the equation of motion in terms of the new modal coordinates:

$$\Delta\, \ddot{\sigma} \;+\; [I_{n\times n} - T diag(1/T_i)]\; \sigma \;=\; 0 \tag{6.15}$$

where $\Delta = \phi^T\phi$ is the new mass matrix. Since we have taken $|T_1| < |T_2| < \cdots |T_n|$, the system stiffness matrix is given by:

$$I_{n\times n} - T\,\mathrm{diag}(1/\mathrm{T_i}) = \begin{bmatrix} 1-\frac{T}{T_1} & 0 & \cdots & 0 \\ 0 & 1-\frac{T}{T_2} & \cdots & 0 \\ \vdots & \vdots & \ddots & \vdots \\ 0 & 0 & \cdots & 1-\frac{T}{T_n} \end{bmatrix} \tag{6.16}$$

This form of the stiffness matrix makes it easy to quantify the stiffness change induced by the cable tension T. To prevent structural instability, the condition $1 - \frac{T}{T_i} > 0$ must hold good for all i, $i = 1, \ldots, n$. Note that the T_i's can be positive or negative, and stability requires that the tension in the cable to be less then the first buckling load. The absolute values of T_i indicate the extent to which the diagonal entries of the stiffness matrix are changed from their original values of unity (when $T = 0$).

The parametric effect of the cable is described by the diagonal geometric stiffness matrix in Eq.(6.16) and optimal cable placement can be defined as the problem of maximizing the deviation of this matrix from the identity stiffness matrix, independent of the cable tension T since it is a common factor in Eq.(6.16). This is in conformity with the observation in section 6.2 where optimal cable placement resulted in the geometric stiffness matrix with the "largest" norm. To maximize the norm of k_g independent of T, we propose the following performance function:

$$F_p = \sum_{i=1}^{n} 1/T_i^2. \tag{6.17}$$

In the next section we consider a numerical example and determine the optimal cable placement based on this performance function.

6.5.3 Numerical Simulations

In this section we present simulation results of vibration suppression based on the control scheme in Fig.6.7. Consider the frame structure in Fig.6.8 and assume that the cable can run in the plane of the structure between any three nodes. It is assumed that the cable is rerouted through a pulley at the middle node and that the actuator

is fixed at one of the two end nodes, which are restricted to be different nodes of the structure. The frame is taken to be made of aluminum pipes, the geometric and material properties of which are shown in Tab.6.2. The structure is assumed to be 1.2 m in length and 1.0 m in height. The natural frequencies and mode shapes are calculated from the mass and stiffness matrices of the system, obtained using the FEM method described in Section 6.3. A two-mode model is then obtained through model reduction. The natural frequencies of the tension-free system are as follows: $f_1 = 2.94\ Hz$ and $f_2 = 8.13\ Hz$. In this example, damping is ignored. Since the cable lies entirely in the plane of the structure, the forcing vector is zero, *i.e.*, $f = 0$. The initial conditions, in SI units, used in this simulation are as follows:

$$\begin{aligned} x_1(0) &= \begin{bmatrix} a_1(0) \\ a_2(0) \end{bmatrix} = \begin{bmatrix} 0.1 \\ 0.01 \end{bmatrix}, \\ x_2(0) &= \begin{bmatrix} \dot{a}_1(0) \\ \dot{a}_2(0) \end{bmatrix} = \begin{bmatrix} 0.0 \\ 0.0 \end{bmatrix} \end{aligned} \tag{6.18}$$

The performance function is chosen based on the first two buckling loads and is selected to be: $F_p = 1/T_1^2 + 1/T_2^2$. The tension in the cable is switched between 0 and $50N$. The low pass filter cut-off frequency is 15.9 Hz and the boundary-layer parameter is taken to be $\varepsilon = 10^{-7}$. The value of F_p was calculated for all possible cable configurations: three sample cable locations are shown in Fig.6.8. The cable configuration for Case I corresponds to the maximum value of F_p and this makes it the best configuration with respect to the proposed criterion. The remaining cases, Case II and III are shown for comparison. Numerical simulations of the response, demonstrating and comparing vibration suppression for all three cases are shown in Fig.6.9. The results indicate that the value of F_p is a useful measure of effective cable configuration.

Table 6.2. Material and geometric properties of the frame structure

Material	*Aluminum*
Modulus of rigidity	26.2 GPa
Pipe diameter	9.53 mm
Young's modulus	71.0 GPa
Pipe Thickness	1.00 mm
Density	2710 kg/m^3

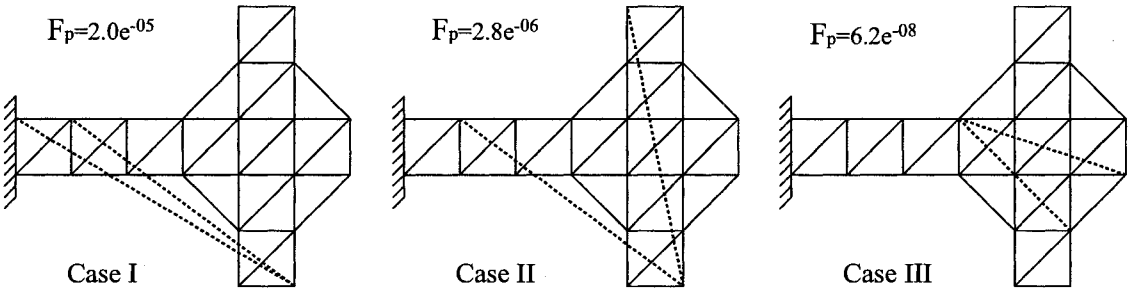

Figure 6.8. Different cable placements

6.6 Control by Transverse Cable Force

6.6.1 Problem Statement

In this section we consider direct cable control of the closed loop system in Fig.6.7 by setting $k_g = 0$ in Eq.(6.9). The tension in the cable is considered to be sufficiently small, or placed in such a manner that it will not cause a significant change in the stiffness of the system. Therefore, the effects of Tk_g can be ignored. The control scheme in Fig.6.7 is used by ignoring the k_g term and the low pass filter, and by switching the tension in the cable between 0 and T instead of $-T$ and $+T$. For this case, the issue of cable placement is not investigated since this problem is similar to the actuator placement problem in linear systems, which is well know in the literature; see, Hamdan and Nayfeh [45] and Sadri et al. [46], for example. Numerical simulations

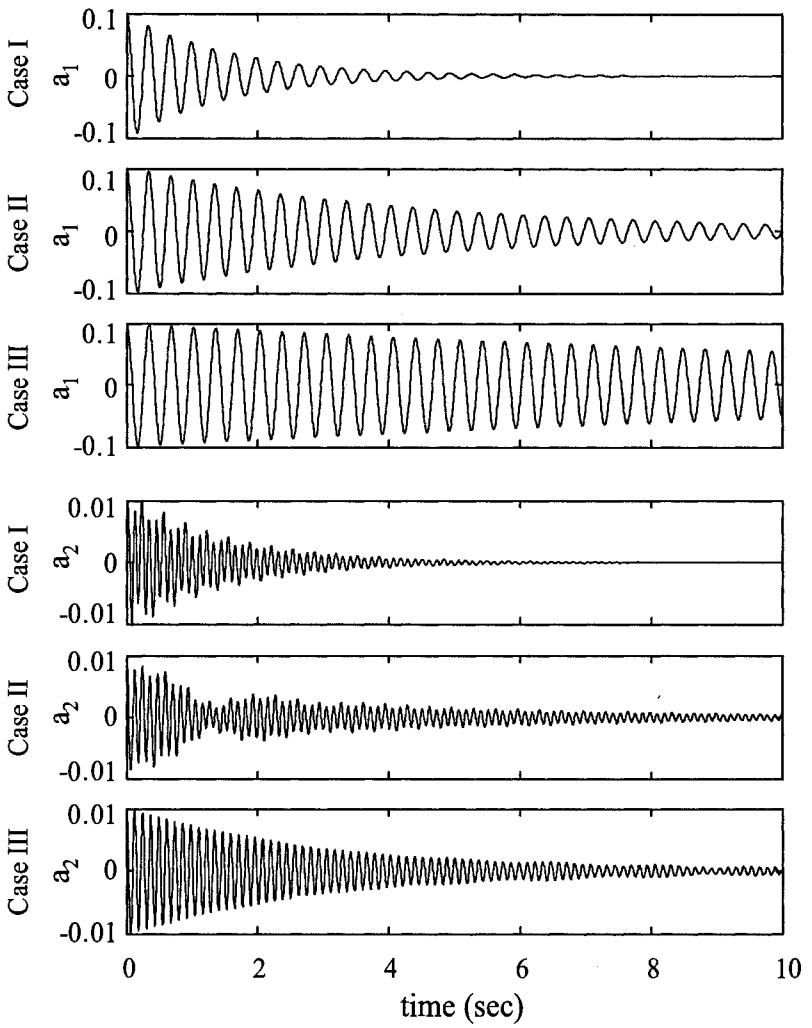

Figure 6.9. Simulation of decay in modal amplitude a_1 and a_2 due to the control in Fig.6.2, for cable configuration in Case I, Case II and Case III

are presented in the next section, followed by experimental results.

6.6.2 Numerical Simulations

Numerical simulations of vibration control of the frame structure depicted in Fig.6.10 are shown in this section to prove the feasibility of the control scheme. The structure in Fig.6.10 is a 2D frame made of elements with circular cross-sectional areas. The geometric and material properties of the elements are the same as those in Tab.6.2, with the difference that the frame elements are solid rods and not hollow pipes. The

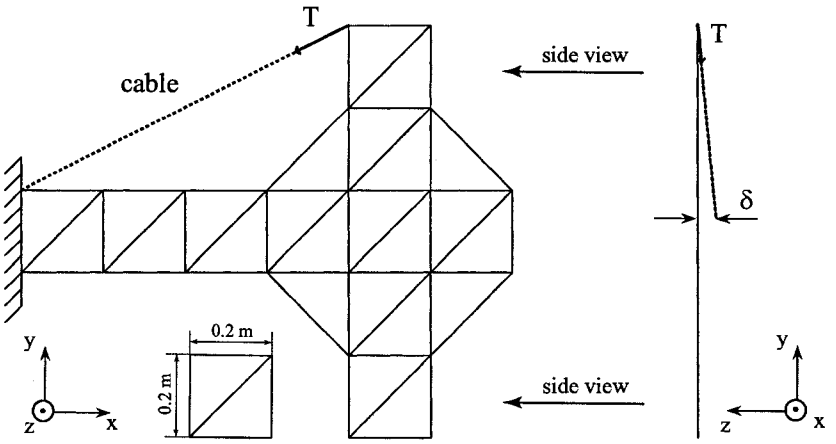

Figure 6.10. Front and side view of the frame structure

frame is assumed to be fixed at one end and have a length of 1.2 m and a height of 1.0 m. The cable is assumed to be attached as shown with $\delta = 12.7\ mm$. After calculating the elementary mass and stiffness matrices, the global mass and stiffness matrices are evaluated. The mesh is refined until the natural frequencies of the first two significant modes converge. A two mode model of the structure is used with modal damping ratios of $\xi_1 = \xi_2 = 0.001$. The first two natural frequencies of the system are found to be $f_1 = 2.19\ Hz$ and $f_2 = 6.06\ Hz$. The first mode is a pure beam bending-like mode and the second is a torsional mode. Both mode shapes are generated using ABAQUS/VIEWER and shown in Fig.6.11. For the control parameters, we choose $\varepsilon = 2.0 \times 10^{-3}$ and $T = 10N$. The initial conditions were chosen in SI units as follows:

$$\begin{aligned} x_1(0) &= \begin{bmatrix} a_1(0) \\ a_2(0) \end{bmatrix} = \begin{bmatrix} 0.01 \\ 0.005 \end{bmatrix}, \\ x_2(0) &= \begin{bmatrix} \dot{a}_1(0) \\ \dot{a}_2(0) \end{bmatrix} = \begin{bmatrix} 0.0 \\ 0.0 \end{bmatrix}. \end{aligned} \tag{6.19}$$

The results of numerical simulations are shown in Fig.6.12. The cable placement is based on high degree of controllability of the first two modes [45] and [46].

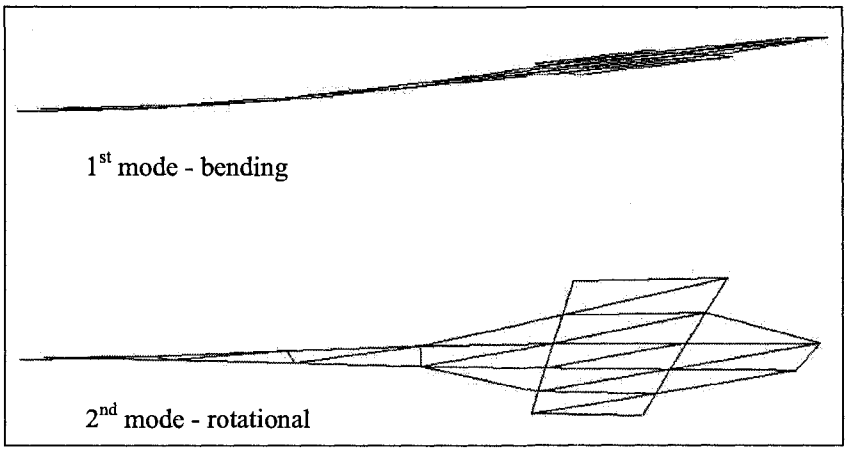

Figure 6.11. Shapes of the first two modes

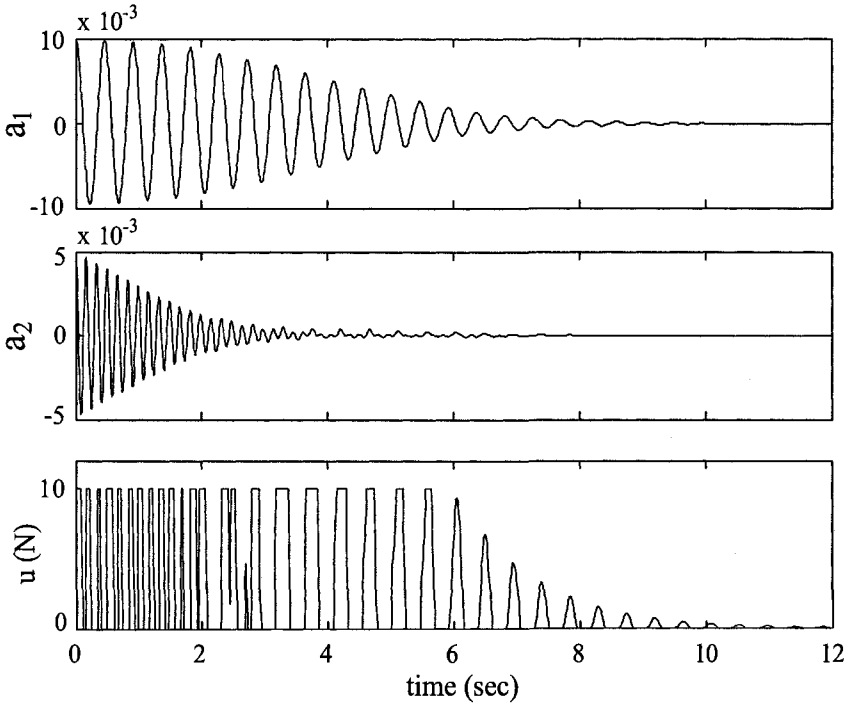

Figure 6.12. Plot of the modal amplitudes of the 1^{st} and 2^{nd} mode, and the control action (cable tension)

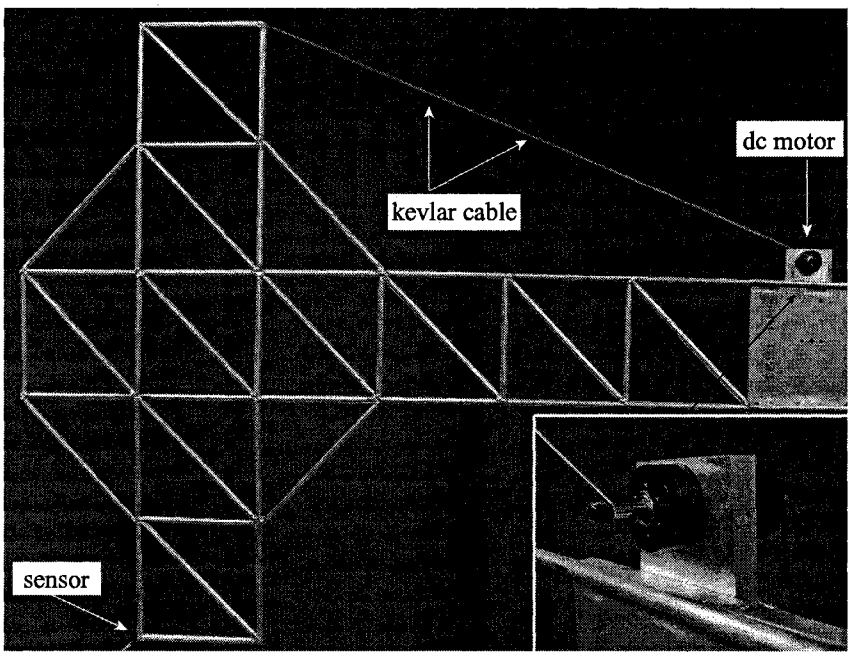

Figure 6.13. Experimental setup

6.6.3 Experiments

Experiments were carried out with the 2-D frame shown in Fig.6.13 which is identical to that of the frame used in the numerical model in the last section. The aluminum frame was built and controlled using a Kevlar cable, where the tension was provided by a dc motor working in current-control mode. The frame is formed by aluminum rods welded together to imitate the shape of a space structure. It is designed to have two frequencies below 10 Hz. The cable position is the same as that used for simulations in the previous section. An accelerometer (manufactured by PCB, with $0.5 - 3000\ Hz$ bandwidth) was placed on the structure (using a small plate welded to the frame) at a location where the significant (i.e., modeled) modes are strongly observable. An observer was programmed in MATLAB/SIMULINK to estimate the amplitudes of the first two modes from the accelerometer readings. Normalized mode shapes with respect to the mass matrix were found numerically using finite element methods. An impulse test was used to estimate the natural frequencies of the system;

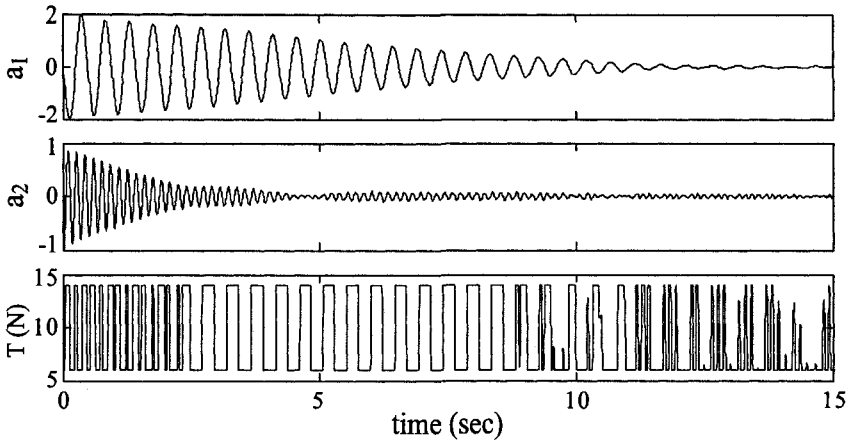

Figure 6.14. Plot of the modal amplitudes of the 1^{st} and 2^{nd} mode, and the control action (cable tension)

an impulse hammer was used for this purpose. The first two natural frequencies of the system were found to be $f_1 = 2.14\ Hz$ and $f_2 = 5.95\ Hz$. The damping ratios were computed as $\xi_1 = 0.003$ and $\xi_2 = 0.002$ using the method of log decrement on decaying oscillations produced after exciting each of the first two modes. The sensed signal from the accelerometer and the feedback signal from the computer were interfaced using a dSPACE DSP board with a 20 kHz sampling frequency. The tension in the cable was switched between 6 N and 14 N; the 6 N bias tension was used to overcome the problem of potential slack in the cable. We chose $\varepsilon = 5 \times 10^{-4}$. It is important to note that the natural frequency of the isolated cable under bias tension is much higher than the first two natural frequencies of the structure. This precludes the possibility of inadvertently exciting the cable modes. The experimental results are shown in Fig.6.14. In this figure, the first two modal amplitudes are plotted they are estimated from the voltage output of the accelerometer.

6.7 Remarks

In this chapter we illustrate the use of cable actuators for vibration suppression in frame structures. We model the cabled structure using finite element methods and

develop a general control scheme for vibration suppression. The control force is transmitted to the structure through a cable actuator and cable tension is applied only when it removes energy from the system. The cable tension has two distinct effects on the structure. The first is a parametric effect that alters the stiffness of the structure and the second is direct effect that stems from externally applied forces. Each effect is considered separately. For the parametric effect, optimal cable placement on the structure is studied and numerical simulations are presented. For the direct effect, numerical and experimental results are presented to demonstrate the effectiveness of the control strategy.

CHAPTER 7

Conclusions

The aim of this work was to explore new methods for vibration suppression in structures. Two strategies were proposed, the first one is a semi-active control strategy and the second is an active control strategy. In the first method, the semi-active strategy, modal energy is transferred to high-frequency modes of structures where it is dissipated naturally and quickly due to high levels of damping. For modal energy dissipation through redistribution, we proposed sequential application and removal of constraints. It was found that the amount of energy pumped into or out of a mode is dependent on the timing of the constraint application and removal and on "modal disparity", which is a property of a structure and the constraint. The phenomenon of modal energy redistribution was validated in a clamped-clamped beam with a hinge in its mid span. The beam has the capability of changing configuration on the fly by activation and deactivation of an electromagnetic brake built in the hinge. After experimental verification of modal disparity and modal energy redistribution, we proposed a semi-active control strategy for finite-dof[1] linear systems. It was shown that energy in these systems can be pumped into the high-frequency flexible modes through sequential application and removal of constraints. This energy is dissipated naturally due to high levels of damping in these modes. In special cases some energy can get trapped in particular modes that are not affected by the constraints. For

[1]finite-degrees of freedom

linear systems, feedback was used and constraints where applied only when the system passed through a specific configuration. This was done only to facilitate investigation of the system behavior in modal coordinates. The use of feedback is not a requirement of the semi-active control strategy and this is illustrated with the example of a nonlinear system where a random sequence of application and removal of constraints is used for energy dissipation. The potential for vibration control without feedback is an advantage of this approach. The full potential of the approach can be achieved through optimal application and removal of constraints. To this end, several optimization problems were investigated with the goal of maximizing energy removal for a specified number of cycles of constraint application and removal. In the second method, the active control strategy, cable actuators where used and cable tension was varied to remove energy from the system. It was found that the cable has two effects on the structure. It applies external forces and alters the stiffness of structures. The cable placement on the structure was investigated with the goal of increasing its control authority. Numerical simulations and experimental results were presented to show the efficacy of vibration control with cable actuators.

Our future work in semiactive control will include applications of the control strategy to real world problems. An important application to be explored is space structures, radar array panels, for example. For easy deployment in space, radar array panels are typically formed by small elements connected by joints that enable them to fold into compact shapes that can fit into the space shuttle bay. Upon arrival in space, these radars will be unfurled and deployed. These structures are prone to vibration problems and one approach to mitigation of such problems is to embed electromagnetic brakes in some of the joints; the activation and deactivation of the brakes will result in application and removal of constraints and lead to the dissipation of vibration energy. Another target application is control of vibration in

membrane-like structures, typically used in space based optical systems. The challenge here is to design non-contact actuators that can apply and release constraints.

Another important consideration for future work is to extend the optimization problem addressed in this research as part of the semi-active control strategy. Even though it was assumed that a single actuator is used to apply and remove constraints, physical constraints associated with the design variables were not taken into consideration. The actuators cannot apply and release constraints at two different locations on a structure arbitrarily quickly and have limits on the maximum impulsive forces that they can generate. In our future work we will address the optimization problem by taking into consideration such constraints.

An important observation made in the course of our research on cable control of structures has been the change in damping characteristics of the structure with the cable in tension. In particular, it has been observed that damping of the structure with the cable in tension is significantly higher than that without the cable. Although this is beneficial in terms of vibration control, the phenomenon of increase in damping remains unexplained and needs to be investigated.

APPENDIX A

An alternate set of generalized coordinates for state α in Fig.4.5 are the angular displacements of the bars, θ_i, $i = 1, 2, 3, 4$, described by the relations

$$\begin{aligned} \theta_1 &= x_1/L \\ \theta_2 &= 2(x_2 - x_1)/L \\ \theta_3 &= 2(x_3 - x_2)/3L \\ \theta_4 &= -x_3/L \end{aligned}$$

If the generalized forces corresponding to x_i be F_i, $i = 1, 2, 3$, and those corresponding to θ_j be M_j, $j = 1, 2, 3, 4$, then, the principle of virtual work

$$\begin{aligned} \sum_{i=1}^{3} F_i \, \delta x_i &= \sum_{j=1}^{4} M_j \, \delta\theta_j \\ &= \sum_{j=1}^{4} M_j \sum_{i=1}^{3} \frac{\partial \theta_j}{\partial x_i} \delta x_i \end{aligned}$$

can be used to establish the relationship between F_i and M_j, namely

$$F_i = \sum_{j=1}^{4} M_j \frac{\partial \theta_j}{\partial x_i}$$

For the numerical example in section 4.4, we have

$$\begin{bmatrix} M_1 \\ M_2 \\ M_3 \\ M_4 \end{bmatrix} = \begin{bmatrix} 0 \\ -\tau(t) \\ \tau(t) \\ 0 \end{bmatrix} \qquad \left(\frac{\partial\theta}{\partial x}\right) = \frac{1}{L}\begin{bmatrix} 1 & 0 & 0 \\ -2 & 2 & 0 \\ 0 & -2/3 & 2/3 \\ 0 & 0 & -1 \end{bmatrix}$$

It follows that

$$\begin{bmatrix} F_1 \\ F_2 \\ F_3 \end{bmatrix} = \frac{1}{L}\begin{bmatrix} 2 \\ -8/3 \\ 2/3 \end{bmatrix}\tau(t) \tag{A.1}$$

And from the definition of the impulsive moment C

$$C = \int_{t_{\alpha\beta}^-}^{t_{\alpha\beta}^+} \tau(t)dt \tag{A.2}$$

it simply follows

$$I_{\alpha\to\beta} = \frac{C}{L}\begin{bmatrix} 2 \\ -8/3 \\ 2/3 \end{bmatrix} \tag{A.3}$$

APPENDIX B

From Eq.(4.24), the impulse vector $I_{\alpha\to\beta}$ can be expressed as

$$M\dot{X}(t^+_{\alpha\beta}) = M\dot{X}(t^-_{\alpha\beta}) + I_{\alpha\to\beta}$$

Substituting the expression for $I_{\alpha\to\beta}$ from Eq.(4.42) and the mass matrix from Section 4.4.4, we get

$$\frac{\rho AL}{12}\begin{bmatrix} 6 & 1 & 0 \\ 1 & 8 & 3 \\ 0 & 3 & 10 \end{bmatrix}\begin{bmatrix} \dot{x}_1(t^+_{\alpha\beta}) \\ \dot{x}_2(t^+_{\alpha\beta}) \\ \dot{x}_3(t^+_{\alpha\beta}) \end{bmatrix} = \frac{\rho AL}{12}\begin{bmatrix} 6 & 1 & 0 \\ 1 & 8 & 3 \\ 0 & 3 & 10 \end{bmatrix}\begin{bmatrix} \dot{x}_1(t^-_{\alpha\beta}) \\ \dot{x}_2(t^-_{\alpha\beta}) \\ \dot{x}_3(t^-_{\alpha\beta}) \end{bmatrix} + \frac{C}{L}\begin{bmatrix} 2 \\ -8/3 \\ 2/3 \end{bmatrix}$$

Using the constraint $\dot{x}_2(t^+_{\alpha\beta}) = [3\dot{x}_1(t^+_{\alpha\beta}) + \dot{x}_3(t^+_{\alpha\beta})]/4$, the above equation can be rewritten as a set of three linear equations in terms of the unknowns, $\dot{x}_1(t^+_{\alpha\beta})$, $\dot{x}_3(t^+_{\alpha\beta})$, and C, as $\mathbf{B}\,U = \mathbf{f}$, where

$$\mathbf{B} = \begin{bmatrix} 9\rho A/16 & \rho A/48 & -2/L \\ 7\rho A/12 & 5\rho A/12 & 8/(3L) \\ 3\rho A/16 & 43\rho A/48 & -2/(3L) \end{bmatrix}, \qquad U = \begin{bmatrix} \dot{x}_1(t^+_{\alpha\beta}) \\ \dot{x}_3(t^+_{\alpha\beta}) \\ C \end{bmatrix}$$

$$\mathbf{f} = \rho A\begin{bmatrix} \dot{x}_1(t^-_{\alpha\beta})/2 + \dot{x}_2(t^-_{\alpha\beta})/12 \\ \dot{x}_1(t^-_{\alpha\beta})/12 + 2\dot{x}_2(t^-_{\alpha\beta})/3 + \dot{x}_3(t^-_{\alpha\beta})/4 \\ \dot{x}_1(t^-_{\alpha\beta})/2 + \dot{x}_2(t^-_{\alpha\beta})/12 \end{bmatrix}$$

Solving the above equation yields

$$C = -\frac{13}{512}\rho AL\left[3\dot{x}_1(t^-_{\alpha\beta}) - 4\dot{x}_2(t^-_{\alpha\beta}) + \dot{x}_3(t^-_{\alpha\beta})\right] \tag{B.1}$$

Substitution of Eq.(B.1) in the expression for ΔE in Eq.(4.25) leads us to the final form

$$\Delta E = -\frac{13}{1536}\rho AL\left[3\dot{x}_1(t^-_{\alpha\beta}) - 4\dot{x}_2(t^-_{\alpha\beta}) + \dot{x}_3(t^-_{\alpha\beta})\right]^2$$

BIBLIOGRAPHY

[1] A. R. Diaz and R. Mukherjee, "Modal disparity enhancement through optimal insertion of non-structural masses," *Structural and Multidisciplinary Optimization*, vol. 31, no. 1, pp. 1–7, 2006.

[2] A. R. Diaz and R. Mukherjee, "A topology optimization problem in control of structures using modal disparity," *ASME Journal of Mechanical Design*, vol. 128, pp. 536–541, 2006.

[3] W. W. Clark, "Vibration control with state-switching piezoelectric materials," *Journal of Intelligent Material Systems and Structures*, vol. 11, no. 4, pp. 263–271, 2000.

[4] L. R. Corr and W. W. Clark, "Energy dissipation analysis of piezoceramic semiactive vibration control," *Journal of Intelligent Material Systems and Structures*, vol. 12, pp. 729–736, 2001.

[5] A. J. Kurdila, W. W. Clark, W. Wang, and D. E. MacDaniel, "Stability of a class of state-switching piezoelectric methods," *ASME International Mechanical Engineering Congress and Exposition: Adaptive Structures and Material Systems*, vol. AD-60, pp. 477–484, 2000.

[6] A. Ramaratnam and N. Jalili, "A switched stiffness approach for structural vibration control: Theory and real-time implementation," *Journal of Sound and Vibration*, vol. 291, pp. 258–274, 2006.

[7] C. H. Hodges, "Confinement of vibration by structural irregularity," *Journal of Sound and Vibration*, vol. 82, pp. 411–424, 1982.

[8] C. Pierre and E. H. Dowell, "Localization of vibration by structural irregularity," *Journal of Sound and Vibration*, vol. 114, pp. 549–564, 1987.

[9] A. F. Vakakis and T. K. Centikaya, "Mode localization in a class of multi-degree of freedom systems with cyclic symmetry," *SIAM Journal on Applied Mathematics*, vol. 53, pp. 265–282, 1993.

[10] G. Kerschen, Y. S. Lee, A. F. Vakakis, D. M. MacFarland, and L. A. Bergman, "Irreversible passive energy transfer in coupled oscillators with essential nonlinearity," *SIAM Journal on Applied Mathematics*, vol. 66, no. 2, pp. 648–679, 2006.

[11] A. F. Vakakis, "Designing a linear structure with a local nonlinear attachment for enhanced energy pumping," *Mechanica*, vol. 38, pp. 677–686, 2003.

[12] J. Yang and F. Giannopoulus, "Active tendon control of structures," *Journal of the Engineering Mechanics Division-ASCE*, vol. 104, no. 3, pp. 551–568, 1978.

[13] J. Yang and F. Giannopoulus, "Active control and stability of cable-stayed bridge," *Journal of the Engineering Mechanics Division-ASCE*, vol. 105, no. 4, pp. 677–694, 1979.

[14] L. Chung, A. Reinhorn, and T. Soong, "Experiments on active control of seismic structures," *Journal of the Engineering Mechanics Division-ASCE*, vol. 114, no. 2, pp. 241–256, 1988.

[15] F. L. Almansa and J. Rodellar, "Control-systems of building structures by active cables," *Journal of Structural Engineering-ASCE*, vol. 115, no. 11, pp. 2897–2913, 1989.

[16] P. Warnitchai, Y. Fujino, B. Pacheco, and R. Agret, "An experimental-study on active tendon control of cable-stayed bridges," *Earthquake Engineering and Structural Dynamics*, vol. 22, no. 2, pp. 93–111, 1993.

[17] M. Magana, P. Volz, and T. Miller, "Nonlinear decentralized control of a flexible cable-stayed beam structure," *Journal of Vibration and Acoustics-Transactions of the ASME*, vol. 119, no. 4, pp. 523–526, 1997.

[18] M. Magana and J. Rodellar, "Nonlinear decentralized active tendon control of cable-stayed bridges," *Journal of Structural Control*, vol. 5, no. 1, pp. 45–62, 1998.

[19] Y. Fujino, T. Susumpow, and P. Warnitchai, "Active control of cable and cable-structure system," *Jsme International Journal Series C-Dynamics Control Robotics and Manufacturing*, vol. 38, no. 2, pp. 260–266, 1995.

[20] Y. Achkire and A. Preumont, "Active tendon control of cable-stayed bridges," *Earthquake Engineering and Structural Dynamics*, vol. 25, no. 6, pp. 585–597, 1996.

[21] F. Bossens and A. Preumont, "Active tendon control of cable-stayed bridges: a large-scale demonstration," *Earthquake Engineering and Structural Dynamics*, vol. 30, no. 7, pp. 961–979, 2001.

[22] Y. Murotsu, H. Okubo, and F. Terui, "Low-authority control of large space structures by using a tendon control-system," *Journal of Guidance Control and Dynamics*, vol. 12, no. 2, pp. 264–272, 1989.

[23] H. Okubo, N. Komatsu, and T. Tsumura, "Tendon control system for active shape control of flexible space structures," *Journal of Intelligent Material Systems and Structures*, vol. 7, no. 4, pp. 470–475, 1996.

[24] A. Preumont, Y. Achkire, and F. Bossens, "Active tendon control of large trusses," *AIAA Journal*, vol. 38, no. 3, pp. 493–498, 2000.

[25] A. Preumont and F. Bossens, "Active tendon control of vibration of truss structures: Theory and experiments," *Journal of Intelligent Material Systems and Strucutres*, vol. 11, no. 2, pp. 91–99, 2000.

[26] S. Nudehi, R. Mukherjee, and S. Shaw, "Active vibration control of a flexible beam using a buckling-type end force," *Journal of Dynamic Systems Measurement and Control-Transactions of the ASME*, vol. 128, no. 2, pp. 278–286, 2006.

[27] A. R. Diaz and R. Mukherjee, "Optimal joint placement and modal disparity in control of flexible structures," *Computers and Structures*, vol. 86, no. 13-14, pp. 1456–1462, 2008.

[28] J. N. Reddy, *An Introduction to the Finite Element Method, third edition.* McGraw-Hill Science/Engineering/Math, 2005.

[29] A. L. Paget, "Vibration in steam turbine buckets and damping by impact," *Engineering*, vol. 143, pp. 305–307, 1937.

[30] P. Lieber and D. P. Jensen, "An acceration damper: Development, design, and some applications," *Transactions of the American Society of Mechanical Engineers*, vol. 67, pp. 523–530, 1945.

[31] C. Grubin, "On the theory of acceleration damper," *ASME Journal of Applied Mechanics*, vol. 23, pp. 373–378, 1956.

[32] G. B. Warburton, "On the theory of acceleration damper," *Journal of Applied Mechanics*, vol. 24, pp. 322–324, 1957.

[33] S. F. Masri, "Analytical and experimental studies of multiple-unit impact dampers," *The Journal of the Acoustical Society of America*, vol. 45, no. 5, pp. 1111–1117, 1969.

[34] S. F. Masri, "Steady state response of a multi-degree system with an impact damper," *ASME Journal of Applied Mechanics*, vol. 40, no. 1, pp. 127–132, 1973.

[35] M. M. Nigm and A. A. Shabana, "Effect of an impact damper on a multi-degree of freedom system," *Journal of Sound and Vibration*, vol. 89, no. 4, pp. 541–557, 1983.

[36] K. Li and A. P. Darby, "Experiments on the effect of an impact damper on a multiple-degree-of-freedom system," *Journal of Vibration and Control*, vol. 12, no. 5, pp. 445–464, 2006.

[37] S. F. Masri and K. Kahyai, "Steady-state motion of a plate with a discontinuous mass," *International Journal of Nonlinear Mechanics*, vol. 9, pp. 451–462, 1974.

[38] R. K. Roy, R. D. Rocke, and J. E. Foster, "The application of impact dampers to continuous systems," *Journal of Engineering for Industry*, vol. 97, no. 4, pp. 1317–1324, 1975.

[39] D. T. Greenwood, "Principles of dynamics, second edition," *Prentice Hall*, vol. Englewood Cliffs, New Jersey, 1988.

[40] J. Issa, R. Mukherjee, A. R. Diaz, and S. W. Shaw, "Modal disparity and its experimental verification," *Journal of Sound and Vibration*, vol. 311, pp. 1465–1475, 2008.

[41] R. A. Horn and C. R. Johnson, "Matrix analysis," *Cambridge University Press*, p. 24.

[42] L. Meirovitch, *Principles And Techniques of Vibrations.* Prentice Hall, 1996.

[43] K. Svanberg, "The method of moving asymptotes - a new method for structural optimization," *International Journal for Numerical Methods In Engineering*, vol. 24, no. 2, pp. 359–373, 1987.

[44] H. K. Khalil, *Nonlinear Systems, third edition.* Prentice Hall, 2001.

[45] A. Hamdan and A. Nayfeh, "Measures of modal controllability and observability for 1st-order and 2nd-order linear-systems," *Journal of Guidance Control and Dynamics*, vol. 12, no. 3, pp. 421–428, 1989.

[46] A. Sadri, J. Wright, and R. Wynne, "Modelling and optimal placement of piezoelectric actuators in isotropic plates using genetic algorithms," *Smart Materials and Structures*, vol. 8, no. 4, pp. 490–498, 1999.